Progress in Materials Science 158 (2026) 101648

Contents lists available at ScienceDirect

Progress in Materials Science

journal homepage: www.elsevier.com/locate/pmatsci

A holistic review of MOF-based solar-driven atmospheric water harvesting

M. Arjmandi [a], M. Khayet [a,b,*], P. Horcajada [c]

[a] Department of Structure of Matter, Thermal Physics and Electronics, Faculty of Physics, University Complutense of Madrid, Avda. Complutense S/n, 28040 Madrid, Spain
[b] Madrid Institute for Advanced Studies of Water (IMDEA Water Institute), Avda. Punto Com no. 2, Alcalá de Henares, 28805 Madrid, Spain
[c] Advanced Porous Materials Unit (APMU), IMDEA Energy Institute, Avda. Ramón de la Sagra 3, Móstoles Madrid E-28935, Spain

ARTICLE INFO

Keywords:
Atmospheric Water Harvesting
Metal Organic Frameworks
Solar, Photothermal
Arid Climates

ABSTRACT

The growing global demand for clean water, particularly in arid and off-grid regions, has spurred intensive research into sustainable water generation technologies. Among them, solar-driven atmospheric water harvesting (SAWH) using metal–organic frameworks (MOFs) has emerged as a highly promising solution, owing to MOFs' exceptional topological/compositional tunability, and high porosity/surface area. This review systematically explores the key material-level and system-level factors influencing SAWH performance. First, we discuss the fundamental requirements for effective water adsorption, including high water uptake at low relative humidity, steep adsorption isotherms, and rapid adsorption–desorption kinetics. We then analyze the photothermal properties critical to solar-triggered desorption and classify strategies to enhance light-to-heat conversion in MOF-based systems, such as bandgap tuning, framework functionalization, and MOF–composite formation. The stability of MOFs under humid conditions, a major limitation for long-term operation, is also critically examined, with a focus on hydrolytic degradation mechanisms and design strategies for robust frameworks. In addition, auxiliary considerations such as management of contaminants, and shaping methodologies for MOFs are addressed, alongside novel device architectures that enhance passive solar utilization. We highlight the evolution of passive SAWH devices, showcasing advances in structural design, material integration, and thermodynamic modeling that enable efficient, continuous, and scalable operation. By consolidating recent advances in MOF chemistry, photothermal engineering, and device optimization, this review provides a comprehensive roadmap for the future development of efficient, sustainable, and deployable SAWH systems.

1. Introduction

Clean water scarcity and energy shortage are two key challenges for real sustainable global development [1]. By 2025, about two-thirds of the world's population will face a shortage of drinking water [2]. In addition, with the development of various industries and the growing need for energy, humanity now finds itself confronting an enormous energy challenge [3]. For access to clean water to solve this global crisis, various types of technologies have been explored, such as thermal distillation, reverse osmosis (RO), etc. [4]. RO processes with limited water transport capacity highly rely on expensive equipment and infrastructure yet are only viable for

* Corresponding author.
E-mail address: khayetm@fis.ucm.es (M. Khayet).

https://doi.org/10.1016/j.pmatsci.2025.101648
Received 14 October 2025; Received in revised form 24 November 2025; Accepted 22 December 2025
Available online 26 December 2025

coastal regions [5]. Also, conventional thermal distillation techniques relies heavily on the combustion of coal or other fossil fuels for heating water into vapor, resulting in high energy consumption, significant energy losses and additional pollution [6]. Therefore, developing cost-effective approaches to supply drinking water with minimal energy consumption is essential. It is estimated that approximately 13 billion tons of freshwater, in the form of both droplets and vapor, exist in the atmosphere at any given time, which is roughly 10 % of all the freshwater stored in lakes. Atmospheric Water Harvesting (AWH) has emerged as a promising technology for providing water resources even in arid and semi-arid regions [7 8]. As illustrated in Fig. 1a, AWH primarily includes (i) water vapor dewing or refrigeration [9], (ii) fog harvesting [10], and (iv) sorption-based AWH [11]. Dewing and refrigeration techniques primarily focus on passive radiative cooling, which operates without the need for external energy input [12]. While passive methods are energy-efficient, active refrigeration, which lowers the air temperature below its dew point, can be highly energy-consuming and impractical for regions with low humidity [13]. On the other hand, considerable efforts have been made to enhance the efficiency of fog harvesting by optimizing surface wettability and employing biomimetic micro/nanostructures [14 15]. For example, researchers have drawn inspiration from the unique structures and functions of desert beetles and pitcher plants to design slippery surfaces with wettable bump arrays, which facilitate droplet movement and rapid water collection [16]. Furthermore, natural materials such as cactus spines, spider silk, and lotus leaves have also contributed significantly to the development of more efficient harvesting systems [17]. However, fog harvesting is limited by the need for high relative humidity (RH), which restricts its applicability in certain geographical areas [18].

In contrast, sorption-based AWH presents a promising alternative for providing potable water, particularly in arid, landlocked areas [19 20 21 22]. This technique offers notable advantages, including the simplicity of the equipment, portability, ease of use in home-based settings, and its environmentally friendly nature [20 23].

As depicted in Fig. 1b, adsorbents typically capture atmospheric water at night, when ambient temperatures are lower and relative RH is higher, concentrating it on their surface or within their pores [23 24]. During the day, the stored water is released from the adsorbents through heating, then condensed and collected as liquid water. This thermal energy required for desorption can be supplied by various sources, such as electricity [25], magnetic fields [26], or solar energy [27]. Among these, solar energy stands out as a clean,

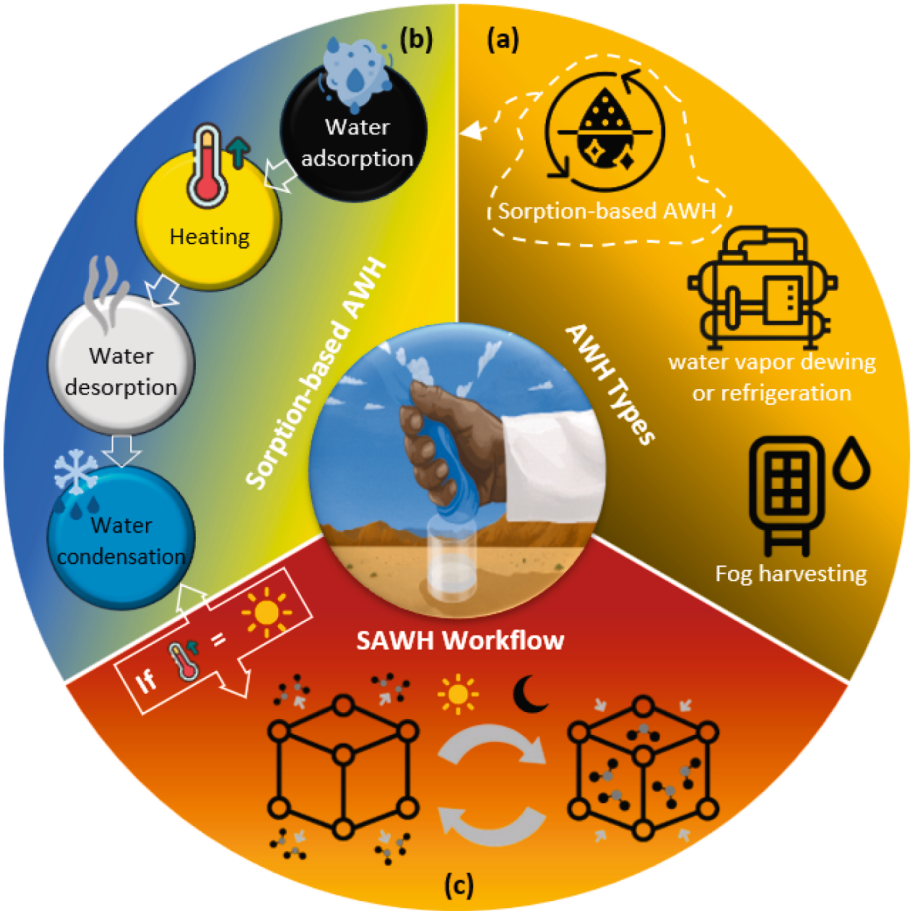

Fig. 1. (a) Main methods of AWH, including fog harvesting, water vapor dewing, and sorption-based AWH, (b) steps of sorption-based AWH method, (c) SAWH workflow.

renewable, and abundant energy source. When harnessed, solar energy is primarily converted into three components: heat loss due to convective heat transfer, radiant energy lost through photothermal conversion, and the energy utilized to drive the water desorption [28]. By relying on solar radiation to provide the necessary heat, the process not only reduces energy costs but also offers an environmentally sustainable solution. The workflow of solar-driven atmospheric water harvesting (SAWH) is illustrated in Fig. 1c. SAWH offers several advantages, including portability, home-based applicability, simple operation, environment compatibility, and exceptionally low energy consumption and cost [29].

The adsorbent material is a critical component of the SAWH system, significantly influencing its overall performance [30]. An ideal adsorbent for SAWH must efficiently capture water vapor even at low RH and rapidly release it upon exposure to solar radiation [31]. Considerable progress is being made in the development of advanced adsorbents to enhance this process [32]. Traditionally, adsorbents used in AWH systems are classified into several types, including zeolites, silica gels, polymer gels, and hygroscopic salt-based composites [28]. Despite their widespread use, these materials exhibit significant limitations under practical operating conditions: zeolites often have low operational capacity [8 28 33 34 35], silica gels show inadequate adsorption performance [8 28 36 37 34 35], polymer gels perform low adsorption kinetic [8 28 23], and salt-based composite face challenges in regeneration [8 28 38 35]. Taken together, these drawbacks prevent conventional adsorbents from simultaneously meeting the critical requirements of efficient water capture at low RH, rapid release, and long-term stability. To maximize the solar energy utilization, ideal adsorbents should combine high light absorption, effective water adsorption even at low RH, rapid water uptake, superior photothermal conversion efficiency, excellent thermal management, and robust stability [23 18 29 35]. Among emerging candidates, Metal-Organic Frameworks (MOFs) stand out as highly promising due to their exceptional performance in meeting these criteria and their demonstrated potential for enhancing SAWH efficiency [29 28 33 27 25 34]. To provide a quantitative perspective, Table 1 summarizes the comparison between MOFs and conventional adsorbents, in terms of cost, water stability, energy consumption, and performance at low RH. As shown in the table, MOFs outperform traditional materials especially in low RH, highlighting their potential to substantially improve SAWH efficiency in arid climates. However, while this table highlights the general trends and advantages of MOFs, we also acknowledge that it is not possible to make definitive statements about all individual adsorbents for every feature, as their performance can vary and even show contradictory behavior depending on specific material properties and operating conditions.

Following the IUPAC definition, MOFs are coordination networks with organic ligands containing potential voids [40 41 42,43]. Some of the more relevant MOF structures includes: (1) Iso-reticular MOFs (IRMOFs), (2) Zeolitic Imidazolate Frameworks (ZIFs), (3) Porous Coordination Networks (PCNs), (4) MOFs developed by the Materials Institute Lavoisier (MIL series), (5) Porous Coordination Polymers (PCPs), and (6) University of Oslo (UIO) family of MOFs [44 45 46]. They are built from composed of metal ions or clusters and connected to polycomplexant organic ligands, they combine exceptional high porosity, structural tunability, and chemical versatility-features that justify their broad potential heir in diverse fields (e.g. including energy, catalysis, environmental remediation, healthcare [47 48 49]). In the context of SAWH, their unique properties translate into clear advantages: i) their structural tunability ensures accessible active sites that facilitate fast adsorption/desorption kinetics and efficient water transport [50 51] ii) their ordered porous structures allows efficient photon penetration and interaction with organic ligands, thereby enhancing solar energy harvesting [52 53 54 55 56]. iii) their redox-active metal nodes act as electron acceptors, promoting photoinduced electron transfer (PET) from excited molecules to metal ions, and generating localized heating, which improves solar-driven water desorption [57 58 59 60 61]; iv) their large surface area, high porosity, and compositional flexibility enable the design of MOF-derived carbons, oxides, and composites with superior photothermal efficiency while remaining non-toxic and environmentally friendly [62 63 64 65 66 67 68]; and v); their compositional versatility through modifications (e.g. metal doping [69 70], introduction of functional groups like dopamine [71 72 73] or amines [74 75]) significantly boost photothermal conversion [76 77] and stability under SAWH operating conditions.

The main objective of this review is to highlight the latent and actual potential of MOFs as key adsorbents in SAWH systems. IT further explores the critical factors influencing MOF performances – water sorption capacity, photothermal properties, and stability under real conditions – together with strategies to enhance these key properties. The review also addresses system-level strategies to improve overall performance, such as the removal of volatile organic compounds (VOCs) and effective thermal management. Additionally, the review highlights recent advances in MOF-based AWH and SAWH systems and devices, identify current challenges, and offer a comprehensive outlook on future directions in material synthesis and system design to overcome existing limitations and optimize SAWH performance.

Table 1
Comparison of MOFs with traditional adsorbents used in AWH systems in terms of cost, stability, energy consumption, and performance at low RH.

Adsorbent Type	Cost	Hydrolytic Stability	Performance at Low RH	Regeneration Energy	Ref.
Zeolites	Moderate	Moderate–High	Moderate	High	[8 28 33 34 35 39]
Silica Gels	Low	Low-Moderate	Low	Moderate	[8 28 36 37 34 35 39]
Polymer Gels	Moderate–High	Moderate	Low- Moderate	Low-Moderate	[8 28 23 39]
Salt-based composite	Moderate–High	Variable	Moderate	High	[8 28 38 35 39]
MOFs	High	Variable	High	Low-Moderate	[8 28 35 39]

2. Fundamental Requirement: Water adsorption in MOFs

2.1. Efficient water adsorption

Efficient water adsorption by MOFs is essential, particularly for SAWH systems [7 28]. Because water uptake behavior in MOFs is strongly governed by their adsorption isotherm profiles, a clear understanding of the isotherm types is necessary before discussing the underlying adsorption mechanisms. According to the IUPAC 2015 classification, adsorption isotherms can be categorized into seven types, which reflect the hydrophilicity, pore structure, and adsorption mechanism of sorbents [78 79 80]. Because water uptake behavior in MOFs is strongly governed by their adsorption isotherm profiles, a clear understanding of the isotherm types is necessary before discussing the underlying adsorption mechanisms. According to the International Union of Pure and Applied Chemistry (IUPAC) classification, adsorption isotherms can be categorized into seven types, which reflect the hydrophilicity, pore structure, and

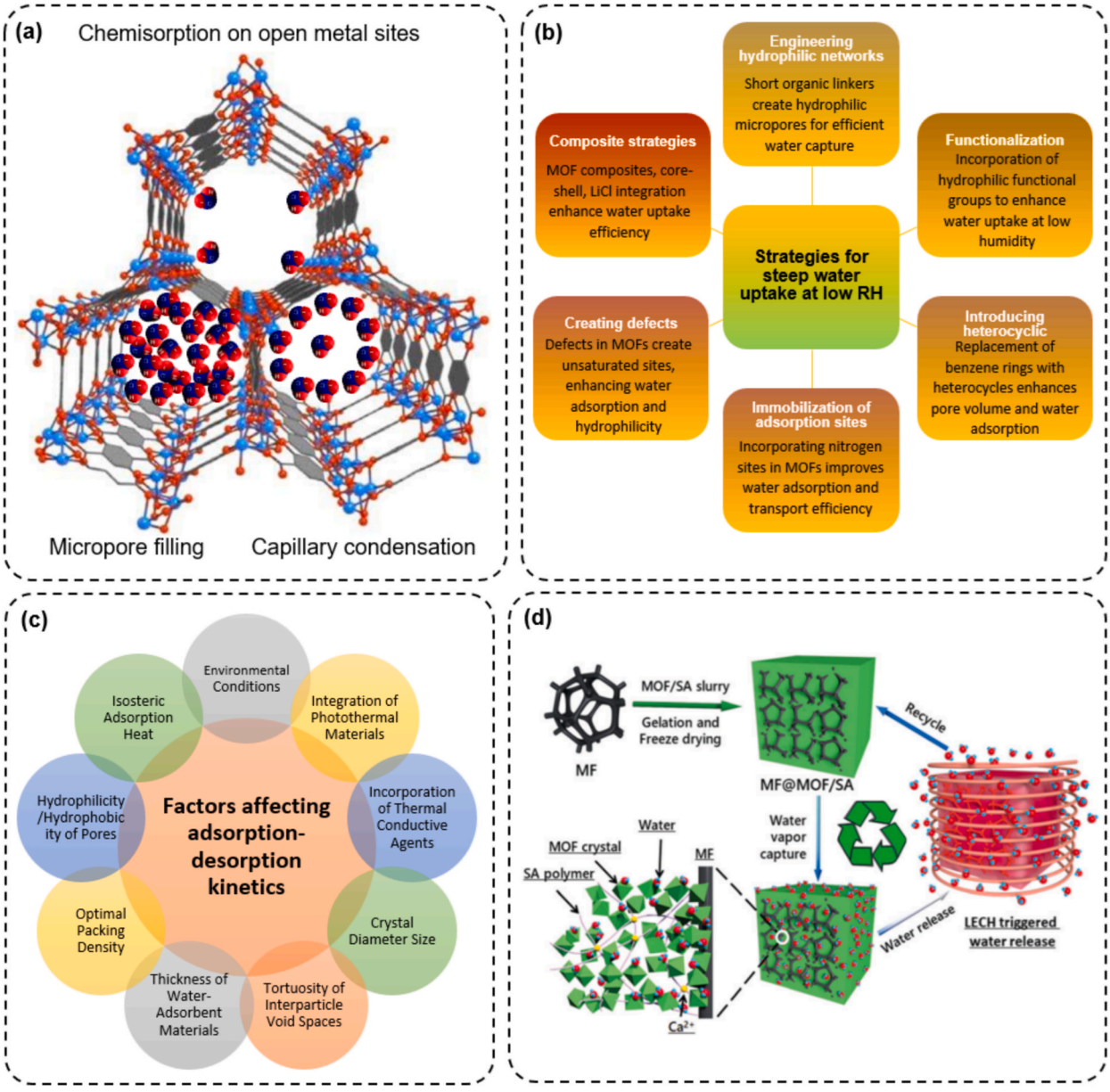

Fig. 2. (a) Schematic representation of water adsorption mechanisms in MOFs, including chemisorption on metal sites, micropore filling, and capillary condensation, (b) Approaches to enhance the water affinity of MOF adsorbents for achieving high water uptake at low humidity, (c) Factors affecting adsorption–desorption kinetics, (d) Schematic view of the fabrication of MF@MOFs, water adsorption and LECH-triggered water release from MF@MOFs [24]. Copyright 2021 Royal Society of Chemistry.

adsorption mechanism of sorbents [74]. Accordingly, different IUPAC isotherm types reflect not only pore-size regimes but also the hydrophilicity of the internal surface [81]. In type I, II, IV, and VI, isotherms, water uptake rises sharply at very low relative pressures, which is characteristic of strongly hydrophilic adsorbents in which primary adsorption sites are readily saturated [33 81]. In contrast, III, V, and VII isotherms exhibit negligible uptakes at low relative pressures, indicating the presence of moderately hydrophobic pore environments where water adsorption begins only after cooperative cluster formation [33 81]. The inflection point (α) of an isotherm that defined as the pressure corresponding to half of the maximum uptake, provides further insight into the humidity range in which a MOF becomes active, thereby helping to identify materials suitable for applications from atmospheric water harvesting to indoor humidity regulation [81]. Generally, the S-shaped (Type V or cooperative Type IV) isotherm is particularly advantageous for SAWH applications [33 82 83 84 85] because adsorption is suppressed at very low RH, preventing strong chemisorption, and undergoes a sharp, cooperative transition once water clustering is initiated. This behavior arises from the interplay between moderate water-framework interactions and strong water-water hydrogen bonding, which produces high working capacity under mild solar regeneration. The isotherm shape is governed not only by pore size and topology but also by functional groups, defects, and polar linkers, which shift the onset of adsorption and modulate hydrophilicity [86]. Tailoring these physicochemical features to achieve S-shaped uptake profiles at low-to-moderate RH represents a key design principle for high-performance water-harvesting MOFs. To better exploit these design principles, it is essential to understand the underlying mechanisms by which water molecules interact with and are adsorbed within MOF structures. As illustrated in Fig. 2a, the water adsorption mechanisms of MOFs can be categorized into three main types [87 81]: (i) *Chemisorption on coordinatively unsaturated metal sites (CUS)*: In MOF structures with unoccupied orbitals on open metal sites, water molecules can undergo chemisorption. These open metal sites arise either from the removal of neutral ligands, solvents, or modulators during synthesis or activation, or from intrinsic structural features such as coordinated solvents or charge-balancing anions belonging to the structure. For instance, heating under vacuum can remove these species, generating CUS. While the chemisorption of water on these sites is reversible, desorption can alter the coordination number of the Secondary Building Units (SBUs) or induce structural deformation [88 89 90]. Moreover, the strong interaction between water molecules and CUS results in a high regeneration temperatures, which can be disadvantageous for SAWH applications [7 91 88]. (ii) *Micropore filling*: In microporous MOFs, the interaction between the pore walls creates a higher van der Waals adsorption potential than surface adsorption, allowing water molecules to be adsorbed into the internal structure [92]. In hydrophobic microporous MOFs, pore filling typically occurs at the pore center [87]. By contrast, in hydrophilic microporous MOFs, water adsorption begins with nucleation at primary sites, such as defects, open metal sites, polar centers, μ-OH groups on SBUs, or hydrophilic groups on linkers [93 91]. This leads to the formation of water clusters via hydrogen bonding, eventually filling the micropores [94 95]. This mechanism is particularly beneficial for SAWH in arid regions [96 93 91]. (iii) *Capillary condensation*: In mesoporous and macroporous MOFs, when the vapor pressure is below saturation vapor pressure, multilayer adsorption and capillary condensation can occur [97 98]. According to the Kelvin equation, the critical pore diameter for capillary condensation of water at atmospheric temperature is 2.076 nm [7]. Therefore, mesoporous MOFs typically exhibit sharp water uptake with IV- or V-type adsorption isotherms [7]. Although their larger pore volume provides higher adsorption capacity, water uptake generally occurs at higher relative pressures than in microporous adsorbent. In some MOFs, such as MIL-101 (which cavities of 2.9 nm and 3.4 nm, accessible through microporous 1.2 and 1.6 nm), high energy is required to release capillary-condensed water, increasing energy consumption, which is detrimental to solar-driven AWH systems [99]. Additionally, hysteresis loops are observed during desorption in certain microporous MOFs, like MIL-53, which are related to structural deformations or the formation of water superclusters [100].

The contribution of these mechanisms varies substantially with humidity. Under low RH, chemisorption at CUS sites is typically the predominant pathway due to the strong water–metal interactions. At intermediate RH, the process transitions to micropore filling, where nucleation at primary sites leads to progressive cluster formation within the pore network. When the RH becomes high, particularly in mesoporous frameworks, capillary condensation governs the uptake behavior. Consequently, water adsorption generally proceeds in order chemisorption, micropore filling, and capillary condensation, although the exact RH thresholds are highly dependent on the physicochemical properties of MOFs, such as porosity, surface area, pore volume and hydrophilicity [101]. These factors can provide more accessible adsorption sites for water molecules and enhance the water uptake capacity. Zheng et al. introduced a mild thermal treatment method to increase the hydrophilicity of CAU-1 while maintaining its structural framework [102]. The modified material, CAU-1–250, exhibits a significantly higher water uptake capacity of 0.48 g g^{-1} at 25 °C and 40 % RH compared to the untreated sample. This enhancement was attributed to the shift in the inflection point of the adsorption isotherm, improved hydrogen bonding interactions, and excellent regeneration performance under mild conditions. Several MOFs, including Cr-soc-MOF-1 [101], MIL-101(Cr) [103], and NU-1500-Cr [104], demonstrate significant water adsorption capacities, attributed to their high porosity and well-defined porous structures. For instance, Cr-soc-MOF-1 exhibits a water uptake capacity of 1.95 g g^{-1} with a BET surface area of 4550 $m^2.g^{-1}$ and a pore volume of 2.1 $cm^3.g^{-1}$ [101]. Similarly, MIL-101(Cr) demonstrates a high-water uptake capacity from 1 to 1.5 g g^{-1}, with a surface area of 3070 $m^2.g^{-1}$ and a pore volume of 1.64 cm^3 g^{-1} [103]. Moreover, NU-1500-Cr, shows a water uptake capacity of 1.09 g g^{-1} at $P/P_0 = 0.90$ (25 °C), with a BET surface area of 3580 m^2 g^{-1} and a pore volume of 1.24 cm^3 g^{-1} [104]. However, there is often a trade-off between high porosity and structural stability [105]. Capillary forces acting on porous walls can cause deformation or even collapse during regeneration, while increasing pore volume generally raises the hydrophobicity of the framework. To enhance stability, strategies such as the introduction of hydrophobic ligands or post-synthetic modifications have been employed. For instance, Yang et al. synthesized a water-stable csq-MOF by capping it with hydrophobic trifluoroacetate moieties, which exhibited reversible water adsorption of 1.32 g g^{-1} [106]. Similarly, Gong et al. developed a series of hydrophobic Zr-MOFs based on a unique [2.2] paracyclophane (PCP) scaffold for improved water sorption [107].

Additionally, defects in MOFs can strongly affect water adsorption behavior by generating new CUS, increasing pore volume and enhancing hydrophilicity [108]. These effects shift the inflection point of the adsorption isotherms toward lower relative pressures,

thus enhancing the water adsorption capacity. For example, post-etching of MIL-101 to create hollow MIL-101 increased its pore volume and improved its water uptake capacity significantly [109]. Moreover, flexible MOFs that exhibit "breathing" or gate-opening effects, transitioning between closed and open pore phases, show great potential for AWH applications, offering high capacity and selective adsorption behaviors [7 110].

Lastly, compounding MOFs with other species can further boost water adsorption. Efforts to improve MOF adsorption capacity focus on increasing porosity or incorporating hygroscopic salts like LiCl, $CaCl_2$, and LiBr. These salts enhance hygroscopicity and have low regeneration temperatures [111 112 113 114]. Compared with other porous substrates such as aerogels, MOFs offer several structural and functional advantages that make them particularly suitable hosts for hygroscopic salts. Their crystalline and uniformly distributed pore networks enable controlled infiltration of salt species while preventing pore collapse or uncontrolled aggregation. The tunable pore size and surface chemistry of MOFs allow optimized salt-framework interactions, which improves salt retention and minimizes leakage during cycling that is one of the major limitations in salt-aerogel systems. Furthermore, many MOFs exhibit intrinsic hydrophilicity and high water uptake at low RH, providing synergistic enhancement when combined with hygroscopic salts. In some cases, MOFs also possess photothermal or heat-localization capabilities, which further facilitate low-energy regeneration. These combined attributes explain why MOF-salt composites typically show superior cycling stability, faster vapor transport, and higher effective water productivity compared to other materials like salt-loaded aerogels. Xu et al. developed LiCl@MIL-101(Cr), which shows better water uptake and cycling stability compared to bulk LiCl [115]. Recently, Tian et al. developed a high-performance composite adsorbent by incorporating LiCl into the pores of MOF-303 (MOF-303@LiCl). This material exhibited a water uptake of 0.61 g g^{-1} at 30 % RH (25 °C), along with rapid adsorption kinetics (saturation within 80 min) [116]. The high cost of lithium chloride however limits its use in practical water harvesting, making calcium chloride ($CaCl_2$) a more affordable alternative. In this sense, An et al. developed a $CaCl_2$@MOF-808 composite, where $CaCl_2$ enhances the hydrophilicity and stability of the MOF, achieving 0.56 g g^{-1} water adsorption at 30 % RH [117]. Additionally, combining photothermal MOFs with traditional adsorbents enhances both water adsorption and regeneration efficiency. Hu et al. encapsulated $CaCl_2$ in Fe-Fc-HCPs, boosting the water adsorption rate from 1.204 to 2.685 g g^{-1} at 80 % RH [118]. Furthermore, $CaCl_2$-decorated MOF-derived porous carbon (PCC-42) exhibits good photothermal properties and water adsorption at low humidity, achieving 1.13 L kg^{-1} daily water production [119]. While incorporating hygroscopic salts into MOFs can partially reduce the accessible surface area or block a portion of the pores, studies have shown that this process does not compromise the integrity of water-stable MOF frameworks. For instance, in $CaCl_2$/MOF-303 composites, increasing $CaCl_2$ content (3.28–8.93 wt%) led to a 45–55 % decrease in BET surface area, yet the pore size distribution and overall structural architecture remained unchanged, confirming that the salt primarily occupies pores without damaging the MOF skeleton [120]. Similarly, salt-in-MOF systems such as $CaCl_2$-in-UiO-66 and LiCl-in-MIL-101(Cr) demonstrate that the rigid and permanent porosity of MOFs provides a confined space for salt deliquescence, preventing leakage and agglomeration while maintaining stable sorption pathways [121]. This confinement effect accelerates adsorption–desorption kinetics and preserves the intrinsic water-uptake characteristics of the MOF, enabling the composite to outperform both the pristine salt and the bare MOF in cycling stability and low-humidity adsorption. These observations suggest that although some pore blockage is inevitable, MOFs generally retain their structural stability and continue to serve as effective matrices for hosting hygroscopic salts. Nevertheless, excessive salt loading may introduce secondary issues such as corrosion risks-particularly for systems relying on metal nodes susceptible to ion exchange [122]. In this regard, strategies that balance capacity with corrosion resistance are essential.

Hybridized MOFs, as another strategy, offer an emerging alternative for improving water harvesting properties. Due to their tunable structural characteristics, these composites enable better adsorption profiles compared to pure MOFs. For example, Hu et al. synthesized MOF-801@MIL-101(Cr) core–shell composites, where the MOF-801 shell pre-concentrates water, enhancing MIL-101′s ability to trap water at low humidity, resulting in a superior water collection rate of 0.253 L kg^{-1} per day under 10–20 % RH. Their results demonstrated that the water uptake capacity of the synthesized supraparticles was approximately 225 and 390 % higher than that of pure MOF-801 and MIL-101, respectively, under low humidity (RH = 8 %) [123]. Luo et al. enhanced water adsorption performance by synthesizing a two-linker MOF (mixed-MOFs(Al)) composed of MIL-160(Al) and Al-fumarate. The combination of two different organic linkers introduces defects and enhances porosity, which results in significantly higher water uptake compared to the single-MOF system. At low RH levels (30, 25, and 20 %), the mixed-MOFs(Al) exhibits superior performance, with water uptake capacities reaching 0.37, 0.31, and 0.25 g g^{-1}, respectively, demonstrating the effectiveness of linker hybridization as a strategy to boost adsorption under dry conditions [124].

Hydrogels and aerogels have also emerged as promising platforms for enhancing the water adsorption performance of MOF-based materials. Hydrogels are used for AWH due to their customizable hydrophilic-hydrophobic structure, stability across different RH ranges, and high-water capacity. Yilmaz et al. developed a polymer-MOF (PC-MOF) hybrid matrix using MIL-101(Cr) nanoparticles (NPs) in a PNIPAM matrix, which combined the water adsorption of MOFs with the hydrophobic properties of PNIPAM [125]. This design allowed continuous adsorption–desorption and efficient self-sustained water delivery, achieving 6.39 g g^{-1} day^{-1} at 90 % RH, with 95 % of the harvested water directly collected.

Building on salt-based systems, Yan et al. created a PML hydrogel composite with MIL-101(Cr) and LiCl, which exhibited a high-water vapor adsorption capacity of 0.614 g g^{-1} at 40 % RH while preventing salt leakage [126]. In parallel, aerogel provides another route for performance enhancement, as their ultralight and highly porous structure with nanoscale pores favors both water adsorption and vapor transport. Wu et al. incorporated Ti_3C_2 into UiO-66-NH_2(TUN) composites and embedded it into a cross-linked sodium alginate (SA) polymer network, creating a vertically aligned porous TUN/SA monolith [127]. This structure not only enhances the material's photothermal properties but also facilitates water vapor diffusion, improving water adsorption–desorption kinetics. The composite achieved a water production rate of 57.8 mL $kg^{-1}h^{-1}$ at 20 % RH. Building on the idea of monolithic structures, He et al. addressed the limitations of MOF powders by creating a monolithic MOF-801 with improved porosity and mechanical strength, using

sol–gel phase separation techniques and subsequent acid-thermal post-processing methods. The resulting material exhibited excellent moisture adsorption at 30 % RH, performing 1.2 times better than conventional MOF-801 powder [128].

2.2. Steep water uptake at low humidity

Given that many regions facing water scarcity are landlocked or arid, water adsorbents must exhibit rapid water uptake at low humidity (RH < 40 %). As outlined in the previous section, MOFs with high surface area, large pore volume, and ultra-high porosity provide more accessible adsorption sites for water, with both large pore volume and high surface area being directly correlated with enhanced water adsorption capacity. However, the strategies discussed in Section 2.1 are not sufficient to develop MOFs capable of efficiently adsorbing water under low RH conditions. For instance, some representative MOFs (MOF-801, MIL-101, MOF-74, MOF-303, etc.) show a water uptake lower than 1 g g^{-1} at low humidity [91 88 7 123]. To enhance the water affinity of MOFs under these conditions, several approaches have been proposed, as illustrated in Fig. 2b, which will be briefly explored below. (i) *Engineering hydrophilic networks*. The hydrophilicity of MOFs arises from a complex interplay between metal nodes and organic linkers. While short polar linkers such as terephthalic acid or pyrazole-based dicarboxylates can contribute to hydrophilic behavior by enabling hydrogen bonding with water molecules, this is not universal. In many cases, aromatic linkers or specific topologies may impart hydrophobic character, as observed in frameworks like MIL-53 or ZIF-8. Therefore, both the chemical nature of the linkers and the coordination environment of the metal centers must be considered when designing hydrophilic MOFs for water adsorption. Water adsorbents with a pore size of about 5–9 Å and short chains (e.g. CAU-10, UiO-66, MIL-160, MOF-801, CAU-6, MOF-303) show that hydrophilic micropores can more effectively capture water molecules by forming hydrogen bonds [96 93 91 129 130]. (ii) *Introducing heterocycle and heterocyclic atom*. Replacing of benzene rings with heterocycles causes to increase in the pore volume and thus increases the water adsorption capacity. Also, the exchange of carbon atoms with heterocyclic atoms (i.e., S, N, O, –NH) could improve the hydrophilicity and hold the pore volume of the structures [94 95]. (iii) *Functionalization*. The introduction of hydrophilic functional groups (e.g., –COOH, –OH, $–NH_2$, $–SO_2$) in MOFs can improve the water uptake at low humidity through shifting the water adsorption inflection point α toward lower relative pressure. In contrast, hydrophobic groups (e.g., $–CH_3$, –F, $–OCH_3$) shift inflection α to higher relative pressure. This approach has been applied for the preparation of MIL-101-NH_2, UiO-66-NH_2, CAU-10-NH_2, etc., all of which exhibit higher affinity compared to their original MOFs [29 93 131 132]. (iv) *Immobilization of adsorption sites*. This strategy focuses on enhancing water uptake by anchoring hydrophilic groups within the MOF structure, thereby creating localized adsorption centers that attract and retain water molecules more efficiently. Li et al. developed a chemically stable MOF, Zr-adip, by incorporating nitrogen Lewis base sites into MIP-200, enhancing pore hydrophilicity and creating secondary adsorption sites for better water molecule attractions. Zr-adip showed a water uptake of 0.43 g g^{-1} at 30 °C and $P/P_0 = 0.25$, outperforming MIP-200 (0.39 g g^{-1}) [133]. Song et al. explored the effect of adsorption sites on water transport, noting that while larger sites improve hydrophilicity, too many (over 30 %) can increase diffusion resistance. An optimal 40 at.% of adsorption sites is desirable. A nanoporous carbon (NC) (Steam-80) with 40 at. % nitrogen sites was synthesized, showing a water uptake of 0.15 L kg^{-1} at 20 % RH [134]. (v) *Creating defects*. Introducing defects into MOF building blocks provides additional unsaturated adsorption sites with stronger primary adsorption strength for water molecules. For instance, the primary isosteric adsorption heat of pristine UiO-66 is about −15 kJ mol^{-1}, whereas defect-engineered UiO-66 can reach up to −60 kJ.mol^{-1}, indicating more hydrophilic pores [33]. Hu et al. synthesized a hollow-structured MIL-101 with abundant defect sites via acid etching, which exhibited enhanced water adsorption compared to pristine MIL-101, further confirming the beneficial role of defects in improving uptake performance. [109]. Also, after applying the defect on MOF-801 single crystal, the water adsorption inflection point of MOF-801 shifted to lower relative pressure [91]. (vi) *Composite strategies*. Recent studies have focused on MOF composites to enhance AWH performance in arid regions. MIL-101, known for its high-water uptake, structural stability, and easy regeneration, has been widely studied for dehumidification and water collection. However, its water uptake typically occurs above 40 % RH due to hydrophobic pore limitations. To overcome this, MOF-801@MIL-101 supraparticles with a core–shell structure were synthesized, exhibiting a pronounced water uptake at RH values as low as 8 % RH. This steep uptake was driven by the synergistic effect between the water-capturing shell (MOF-801) and the high-capacity storage core (MIL-101), enabling efficient adsorption under extremely dry conditions [123]. Additionally, a LiCl@MIL-101 composite, where hygroscopic LiCl was confined within MIL-101′s mesopores, demonstrated an improved water uptake of 0.77 g g^{-1} at 30 % RH and 30 °C, significantly outperforming pure MIL-101 [115].

2.3. Fast adsorption–desorption kinetics

The key factors affecting the adsorption–desorption kinetics are shown in Fig. 2c. Although the located environmental conditions (humidity, wind velocity, temperature, etc.) directly affect the efficiency of water harvesting [135], the adsorption–desorption kinetics of adsorbent also depends on other factors. For SAWH, incorporating photothermal materials to achieve fast kinetics and multi-cycle performance is key [83]. For instance, Tian et al. integrated carbon black (CB) as a photothermal additive into MOF-303@LiCl, enabling rapid desorption under one-sun illumination. The composite reached 66.1 °C without optical focusing and completed desorption within 60 min, supporting multiple adsorption–desorption cycles per day [116]. The crystal size of water adsorbents also has a direct effect on the transport of water molecules and water production [82]. Smaller crystals facilitate faster kinetics due to shorter intraparticle diffusion paths. Water production is also dependent on interparticle transfer, which depends on the size and tortuosity of interparticle voids and even affects the total mass transport [136 137]. The thickness of water-adsorbents and optimal packing density can be estimated by simulation calculations [138]. For fast water vapor diffusion and adsorption–desorption kinetics, a thicker water adsorbent layer is preferred. But heat transfer and mass transfer are interrelated [139]: while increasing the thickness

of water adsorbent materials and packing density improves heat transfer, it simultaneously hinder interparticle vapor transport due to reduced porosity. This negative impact of interfacial heat and mass transfer resistance can be minimized by incorporating a thermally conductive agents within a thin adsorbent layer [85 140]. For instance, Tao et al. synthesized nickel metal foam (MF)-incorporated MIL-101(Cr) (MF@MOF) composite [26]. After crosslinking the infilled slurry with sodium alginate (SA) and Ca^{2+}, followed by freeze-drying, a MF@MOF/SA was obtained. These composites address the thermal insulating nature of MOF monoliths by incorporating metal foam, which not only serves as a mechanical support to enhance robustness but also acts as a low-cost heating element. This allows for rapid heat transfer under localized eddy current heating (LECH). By utilizing LECH, the composites overcome the inherent thermal insulation limitations of MOF monoliths, enabling rapid and uniform heating, thus improving the water desorption kinetics and overall efficiency in AWH applications (Fig. 2d). Additionally, high-frequency water vapor sorption cycling was achieved by fluidizing MOF-801, resulting in dynamic steady-state cycles and high AWH rates of 0.33 L $kg^{-1}h^{-1}$ at 18 % RH (40 cycles per day at 22 °C) [141].

Pore architecture also plays a key role in transport behavior. 1D penetrative pore channels reduce collision frequency and accelerate water diffusion, whereas 3D interconnected cavities restrict diffusivity due to increased collision events. As an example, Sun et al. developed a distinct two-dimensional covalent organic framework (COF)-based system designed to capture moisture from air efficiently and release it rapidly under low-temperature conditions. Their findings indicated that the incorporation of a limited number of hydrophilic functional groups within the otherwise hydrophobic and penetrable pore channels significantly enhanced the adsorption–desorption rate by creating a well-balanced microenvironment for water uptake [142].

The strength of interaction between water molecules and adsorbents, often evaluated through isosteric heat of adsorption, plays a crucial role in determining the regeneration temperature. While weak van der Waals forces (~7.7 kJ mol^{-1}) contribute minimally to adsorption energy, hydrogen bonds (ranging from 9.7 to 29.0 kJ mol^{-1}) offer an optimal balance, promoting faster water release. In contrast, overcoming stronger interactions, such as covalent O–H bonds (~459.3 kJ mol^{-1}) or capillary condensation commonly observed in mesoporous structures, requires significantly higher energy input. Consequently, hydrogen-bond-driven adsorption within micropores represents the most energy-efficient pathway for reversible water uptake and release [136 143 144].

3. Key Criterion: Photothermal performance of MOFs

In addition to achieving high water adsorption efficiency, enhancing the release of adsorbed water from MOFs is a crucial aspect of SAWH [28 96]. Although the strategies presented in Section 2.3 are beneficial for improving the speed and efficiency of water desorption, the most critical factor in SAWH systems is effective heating through the photothermal response of MOFs. Ideally, solar energy holds great potential, if directly converted into heat for water desorption. However, most MOFs used for water harvesting exhibit weak photothermal properties due to their typically white or light-colored nature, which limits their ability to absorb light efficiently [28 119 145]. Therefore, developing innovative strategies to enhance solar absorption and efficiently convert light into heat is essential for providing MOFs with sufficient energy to accelerate the desorption process.

3.1. General photothermal mechanisms

Photothermal mechanisms are dependent on the nature of the adsorbents and generally involve the following three mechanisms, as shown in Fig. 3(a-c): (i) *Plasmonic heating*. The plasmonic heating mechanism converts light into heat within a wavelength range of approximately 300–1000 nm [146]. In plasmonic materials, electromagnetic radiation is mainly absorbed through intraband transitions [147]. This absorption, known as free carrier absorption, occurs when free conduction electrons are excited to higher energy states within the conduction band [148]. When incident light stimulates the resonance oscillation of valence electrons in a plasmonic material, this phenomenon is called Surface Plasmon Resonance (SPR) [149]. In nanometer-sized structures, SPR is referred to as Localized Surface Plasmon Resonance (LSPR) [149], as illustrated in Fig. 3a. LSPR represents a resonant photon-induced coherent oscillation of charges, which happens when the photon frequency matches the natural frequency of material surface electrons, known

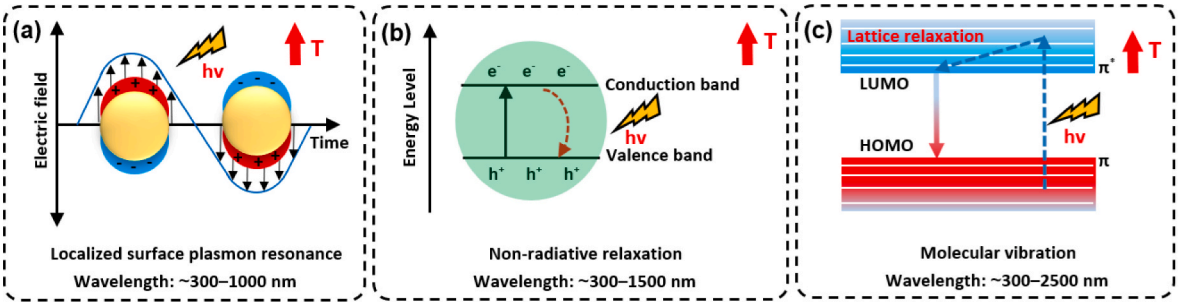

Fig. 3. Schematic representation of the three main photothermal mechanisms. (a) Localized surface plasmon resonance (LSPR)/plasmonic heating, typically active within the ~ 300–1000 nm wavelength range; (b) non-radiative relaxation in semiconductors, generally occurring across ~ 300–1500 nm depending on the bandgap; and (c) molecular vibration–induced heating, primarily associated with mid-infrared absorption (≈300–2500 μm).

as the LSPR frequency [150]. This unique optical phenomenon typically occurs in metallic structures, but several other materials exhibit metal-like optical properties in specific wavelength ranges [151]. Metals in NP form, such as gold (Au) and silver (Ag), have a much higher surface area and exhibit more surface plasmon activity [149]. The LSPR frequency in these NPs tends to fall within the visible range of the electromagnetic spectrum, resulting in higher absorption of light. In MOF-based systems, this mechanism is observed in composites like AuBP@UIO-66 [66] and Bi_2Se_3@ZIF-8 [152], where MOFs stabilize nanoparticles and enhance heat generation. The LSPR effect leads to three primary phenomena: near-field enhancement, hot electron generation, and photothermal conversion [150]. The plasmon-assisted photothermal process initiates electron gas fluctuations, exciting electrons from occupied states to unoccupied states. This creates hot electrons, which lead to an uneven charge distribution [153]. The energy generated by these hot electrons is transferred to the lattice phonons, which are vibrational energy units resulting from oscillating atoms within a crystal structure [154]. Ultimately, the system's local temperature increases due to the energy exchange between electron–electron interactions and lattice cooling via phonon–phonon coupling [155]. (ii) *Non-radiative relaxation*. The conversion of light to heat via the non-radiative relaxation mechanism occurs within a wavelength range of approximately 300–1500 nm, which is specific to semiconductor materials [156]. These materials are typically opaque in the visible spectrum and translucent in the infrared (IR) region [148]. Their absorption in the visible range is primarily due to the generation of free carriers, a process that is dependent on the semiconductor's bandgap. Some transition metal semiconductors, however, exhibit absorption in the nearby IR region, which is attributed to the LSPR effect and interband transitions. In these materials, light absorption is strongly dependent on the wavelength near the bandgap energy and occurs through interband electron transitions. When exposed to light, electron-hole pairs are generated, with energy approximately equal to the bandgap energy [157]. The transition of electrons by photoexcitation can release heat in the nonradiative relaxation process to return to the ground state (Fig. 3b) [158]. MOF-based composites such as CdS@MIL-101(Cr) [159] and Cu_7S_4@ZIF-8 [160] demonstrate enhanced photothermal performance through efficient charge separation and non-radiative relaxation. Optical and electronic interband transitions can be classified as direct or indirect [161]. In a direct transition, the photon-electron interaction occurs without a change in the wave vector, meaning that the crystal momentum of the electrons and holes remains the same in both the conduction and valence bands [161]. In contrast, an indirect transition involves the participation of photons, electrons, and lattice phonons, which results in a change in the wave vector [161]. In terms of enhancing light absorption, direct interband transitions are generally more efficient than indirect transitions. (iii) *Molecular vibration*. Heat generation via the molecular vibration mechanism typically occurs in organic materials following light absorption, which results from molecular electronic transitions [162]. The molecular vibration mechanism absorbs light over a broad wavelength range of approximately 300–2500 nm, consistent with the behavior of organic and graphene-like materials (Fig. 3c) [163]. In general, molecular electronic transitions happen when electrons in a molecule are excited from one energy level to a higher energy level. These electrons reside in molecular orbitals, which are categorized into the lowest unoccupied molecular orbital (LUMO) and the highest occupied molecular orbital (HOMO). Covalent bonding is the primary means of connection in organic compounds, and it encompasses various types of interactions. Among these, two are of particular significance: the sigma (σ) bond and the pi (π) bond [148]. These bonds are formed through the overlap of atomic orbitals. Sigma bonds are the strongest covalent bonds and arise from the end-to-end overlap of atomic orbitals in the HOMO-LUMO bandgap. In organic compounds, most single bonds, such as O–H, C-O, C–H, and C–C, have substantial energy gaps between the σ and σ^* orbitals, which prevents σ to σ^* transitions under solar irradiation [148 164]. Conversely, π bonds are generally weaker than σ bonds due to the less tightly bound electrons, and they are formed when the lobes of atomic orbitals overlap [165]. Electrons in π bonds can be excited to the π^* orbital with relatively lower energy input [165]. In graphene-like materials, π-π^* bonds form across a wide range of wavelengths of sunlight irradiation, and as the π-π^* bonds increase, the HOMO-LUMO energy gap decreases [148 166]. Furthermore, π-π^* bonds can induce a red-shift in the absorption spectrum [167]. Eventually, the excited electrons dissipate their energy via electron–phonon interactions, transferring the absorbed photon energy into lattice vibrations. This process leads to a localized temperature rise within the organic matrix [168]. In MOFs and MOF@COF composites, such as MOF-303@LiCl@CB [116] or NH_2-MIL-125@TAPB-PDA [169], π-π bond vibrations in the organic linkers contribute to local temperature rise.

3.2. General approaches to enhance photothermal efficiency

The total sunlight absorptance at a specific angle is determined by weighting the spectral absorptance against the solar spectral irradiance distribution of the standard solar spectrum (AM1.5) and integrating over the wavelengths where sunlight radiation reaches the surface of the material. According to the AM1.5 standard, the wavelength range of 300–400 nm (ultraviolet region) accounts for approximately 3 % of the total power, the 400–700 nm range (visible light) contributes about 45 %, and the 700–2500 nm range (infrared region) makes up around 52 % of the total power [148] (Fig. 4a). This indicates that absorbers should exhibit high absorbance across the 300–2500 nm wavelength range [170]. Furthermore, to optimize the absorption of solar energy and efficiently convert it into heat, the reflectance of the absorber must be minimal [171]. To achieve high sunlight absorption, it is essential to design absorber materials with enhanced intensity and a broad optical absorption range. There are several approaches available for adjusting the optical properties of photothermal materials, as shown in Fig. 4b.

3.2.1. Change in the LSPR

The surface plasmon band is influenced by several factors, including material nature, shape [172], particle size [173], dielectric constant [174], and coulombic charge [175]. Modifying these factors can lead to various outcomes, as shown in Fig. 4c-e, which illustrates how changes in shape [176], size [177], and material [178] affect the LSPR wavelength (frequency). However, the effect on broadening the absorption range is limited [179]. To extend the LSPR spectral range, introducing hollow structures or reducing shape

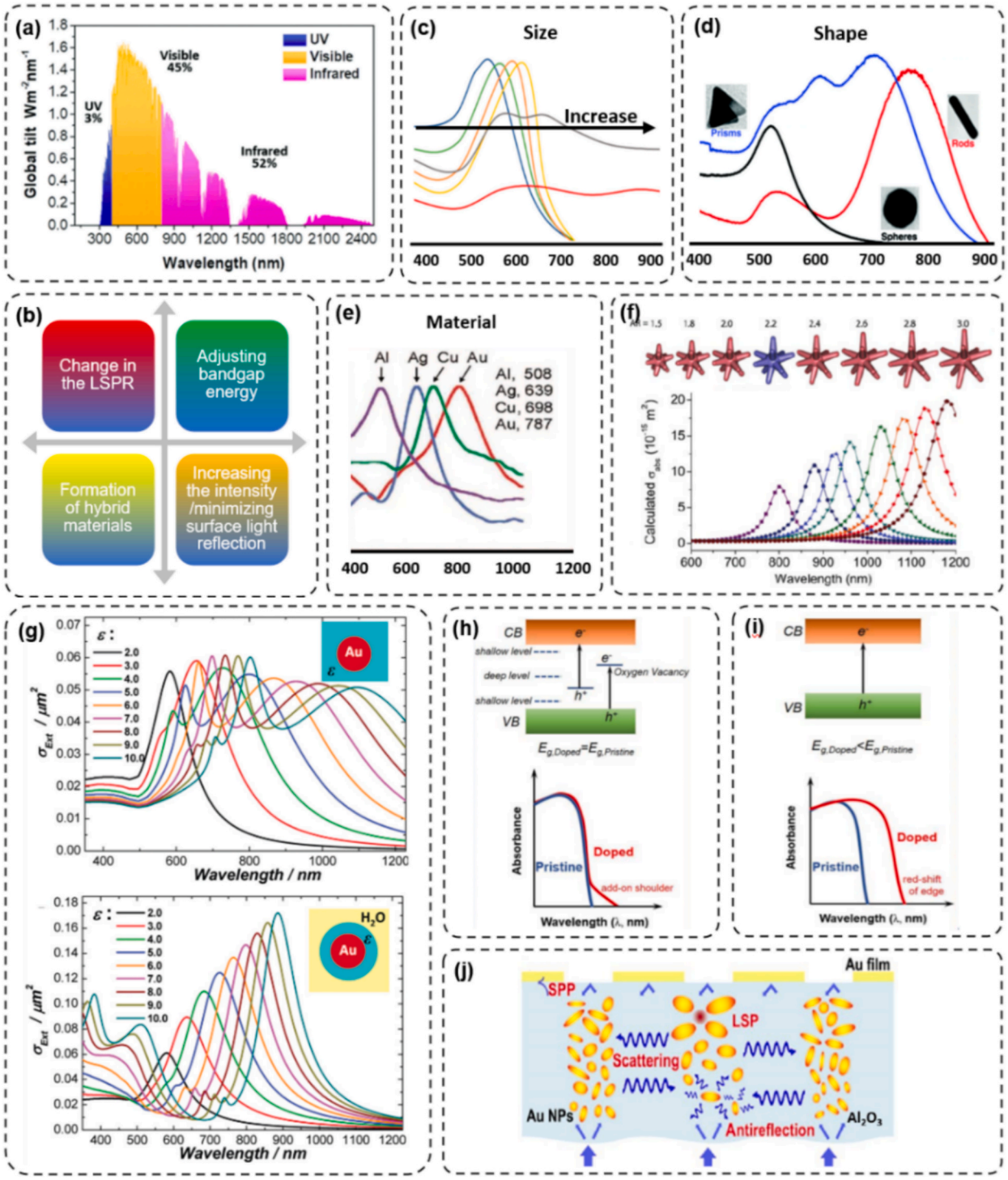

(caption on next page)

Fig. 4. (a) Spectral distribution of solar irradiance under AM1.5, highlighting the UV, visible, and infrared regions [132]. Copyright 2019 Royal Society of Chemistry. (b) Strategies for enhancing light absorption and minimizing reflectance in photothermal materials. (c–e) Effects of NPs size [151], shape [66], and material [152] composition on the LSPR peak position. Copyright 2018 MDPI (Open Access), Copyright 2015 Royal Society of Chemistry, and Copyright 2008 American Chemical Society, respectively. (f) Polarization-averaged absorption as a function of aspect ratio in asymmetric nanostar structures; 3D geometries shown above illustrate shape variations used in the simulations [153]. Copyright 2012 IOPscience. (g) Simulated extinction spectra of gold-based nanostructures under varying dielectric conditions: (top) Au nanospheres in media with different dielectric constants; (bottom) Au@dielectric core–shell NPs with fixed core size and variable shell permittivity [154]. Copyright 2012 American Chemical Society. Schematic strategies for engineering the electronic band structure of semiconductors to enhance light absorption, including doping-induced formation of (h) shallow/deep energy levels [155] and (i) band gap narrowing [155]. Copyright 2015 Royal Society of Chemistry. (j) Broad-spectrum light absorption using Au NP–Al_2O_3 composite structure [156]. Copyright 2016 Science.

symmetry (Fig. 4f) can be helpful [180]. Studies have examined the effects of geometric modifications through simulations of various structures, such as concave shapes, nanocubes, octagons, nanostars, octahedrons, and nanocages [163]. The results show that plasmonic heat generation is concentrated at the tips, corners, and edges, where electromagnetic fields intensify. Sharp, thin structures allow better penetration of the electric field, engaging the entire plasmonic material in heating. Non-symmetrical and hollow structures, on the other hand, enhance broadband absorption.

In addition to geometric factors, the optical properties of plasmonic materials, like absorption resonance wavelength and intensity, are sensitive to the surrounding environment. Changes in the dielectric medium can shift the plasmon resonance wavelength [181], as shown in Fig. 4g. To address this, the dielectric layer surrounding the particles can be made from semiconductors with suitable bandgaps to improve light absorption. Achieving an effective photothermal effect depends on the nature, porosity, and thickness of the dielectric medium, which must be carefully controlled, as improper coatings may reduce plasmonic properties [181].

Another factor influencing LSPR is plasmonic optical coupling, which can occur in isolated NPs or between two neighboring ones [182]. Plasmonic coupling allows for the creation of a new plasmon mode by modifying the nanostructure, enabling multiple localized surface plasmon polariton resonances (SPPR) within a compatible range [183]. For instance, nanostars or nanoflowers with multiple tips can induce intraparticle coupling, resulting in a red-shift and enhanced dipole moment [184]. Placing NPs close together concentrates the electric field in the gap, leading to stronger photothermal effects. In MOFs, plasmonic nanoparticles embedded within frameworks, e.g., AuBP@UIO-66 [66] or Pt/ZIF-8 [185], show improved LSPR-driven photothermal conversion due to MOF stabilization and electronic interaction. The overall photothermal performance depends on the coupling effect between particles, enhancing collective heating, and is influenced by factors such as incident light direction, gap distance, and particle number [186 187].

3.2.2. Adjusting bandgap energy

The concentration of free carriers in semiconductors is much lower than in metals [188]. A common method to increase free carrier concentration and modify the absorption range of semiconductors is doping, which involves adding impurities or creating disorder within the nanomaterials [189]. MOF-semiconductor composites like CdS@MIL-101(Cr) [159] and UiO-66(Ce)/CdS/g-C_3N_4 [190] utilize this approach for efficient light harvesting and charge separation. Doping plays a significant role in enhancing the absorption capacity of semiconductors, thereby boosting photothermal conversion efficiency by promoting nonradiative recombination. One of the key effects of doping is the creation of localized states, which serve as the dominant centers for optical excitation and relaxation [191 192]. These states effectively extend the absorption tail of the semiconductor's absorption spectrum to longer wavelengths, compared to the pristine material (Fig. 4h). Additionally, doping results in a shift of the conduction or valence band, narrowing the bandgap (Fig. 4i), which causes a redshift at the absorption spectrum's edge [191]. Eventually, the excited electrons release their energy and return to a lower energy state. This energy release can occur either through radiative relaxation, in the form of photon emission, or non-radiative relaxation, where energy is transferred to impurities or surface bonds as phonons. When energy is released as photons, it causes localized heating within the lattice, leading to temperature distribution across the material depending on its optical absorption properties and recombination dynamics in both the bulk and surface regions. The photothermal effect results from the diffusion of optically absorbed energy, followed by the recombination of electron-hole pairs, causing temperature variation within the material.

3.2.3. Increasing intensity and minimizing surface light reflection

Improving the sunlight absorption ability of absorbers depends not only on broadening the absorption range but also minimizing surface light reflection and increasing the intensity. One of the most effective approaches to increase sunlight absorption is to create porous absorbers [193 194]. Porosity can minimize light reflection by reducing the effective refractive index of materials and the angular dependence of radiant light. Besides, pores act as optical micropores to limit light through multiple light reflections and scattering [194]. Porous MOFs such as MOF-303@LiCl [116] provide efficient light trapping, improving photothermal performance under solar irradiation. Another example is carbon sponges, which exhibit very low optical transmittance (~0.1 %) and reflectance (~3%). These properties indicate strong attenuation of light across the solar spectrum, primarily due to extended light travel within the structure and enhanced scattering by the nanoscale fibrous network [195].

3.2.4. Formation of composite materials

Another approach to achieve enhanced absorption is the formation of composite materials with complementary and/or synergistic optical properties, which provide both combinatorial optical responses and tailored structural designs for light scattering. Improving optical behavior can also be accomplished through engineered architecture within these composite systems. For example, plasmonic

particles embedded in 1D columnar scattering media have been shown to achieve exceptionally high solar absorption up to 99 % across the full solar spectrum. For instance, Zielinski et al. demonstrated how combining material composition with geometric design in bimetallic Ag/Au hollow nanostructures with mesoporous shells effectively promotes absorption and suppresses scattering across a broad spectral range [196]. In another study, Ansari et al. reviewed the development of metal oxide/carbon dot nanocomposites, where carbon dots played a dual role: increasing light absorption in the visible spectrum and enhancing pollutant adsorption, thus boosting photocatalytic activity [197]. Zhou et al. developed a system with 99 % light absorption over an exceptionally broad spectrum (400 nm to 10 μm) by utilizing a nanoporous aluminum oxide template as an efficient light-trapping medium, combined with randomly distributed self-assembled Au NPs to generate a hybridized LSPR effect (Fig. 4j) [198]. The synergistic combination of different materials, leveraging their intrinsic optical and structural properties, plays a key role in enhancing both the absorption range and intensity of light. MOF-based composites, including Cu@HKUST-1 [199] and MOF@COF systems like NH_2-MIL-125@TAPB-PDA [169], exploit synergistic interactions to boost photothermal efficiency. These examples clearly highlight how hybridization-through band structure engineering, synergistic morphology, and multi-component optical integration-offers an effective route to improve solar light utilization in photothermal systems.

3.3. *Specific approaches to enhance photothermal efficiency in MOFs*

To enhance photothermal efficiency in MOFs, various approaches have been categorized into different strategies. An overview of these strategies is schematically illustrated in Fig. 5. Importantly, not all approaches directly target photothermal performance. Instead, many focus on improving the overall photoactivity of MOF-based systems, such as light absorption, charge separation, and photothermal catalytic/photocatalytic reactivity, which in turn contribute to, or reveal, their latent photothermal potential. It is important to note that while conventional photothermal materials, such as carbon-based absorbers, plasmonic nanoparticles, and semiconductor nanostructures, often exhibit high intrinsic light-to-heat conversion, their direct integration into sorbent beds is not straightforward for SAWH applications. External photothermal layers or fillers typically reduce the accessible surface area of the sorbent, partially block transport pathways, alter pore hydrophilicity, or introduce non-porous domains that hinder vapor diffusion. For instance, a recent study on MOF-801 composites with graphite (G) and CNT demonstrated that adding these carbon materials significantly reduces the BET surface area, micropore volume, and saturated water uptake capacity [200]. As a result, despite their high photothermal efficiency, these materials may significantly suppress adsorption/desorption kinetics and reduce overall water harvesting yield. In contrast, MOFs allow intrinsic or framework-confined photothermal modification while preserving structural integrity and mass-transport continuity. The ability of MOFs to incorporate photoactive ligands, metal clusters, radicals, or confined nanoparticles without severely compromising sorption channels provides a unique advantage over traditional photothermal materials. This synergy between photothermal activation and efficient water transport underpins the growing interest in MOF-based photothermal sorbents for SAWH systems. In this section, we explore a range of synthetic and structural modification methods that, while

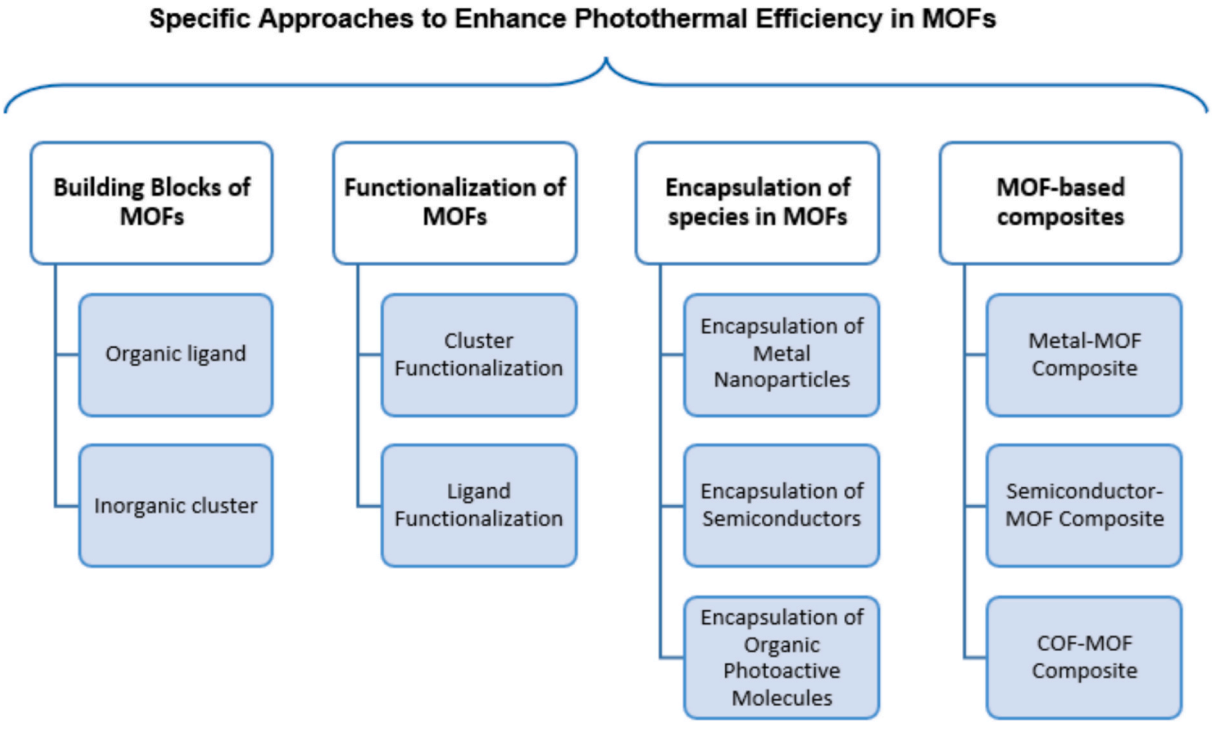

Fig. 5. Classification of specific approaches to enhance photothermal efficiency in MOFs.

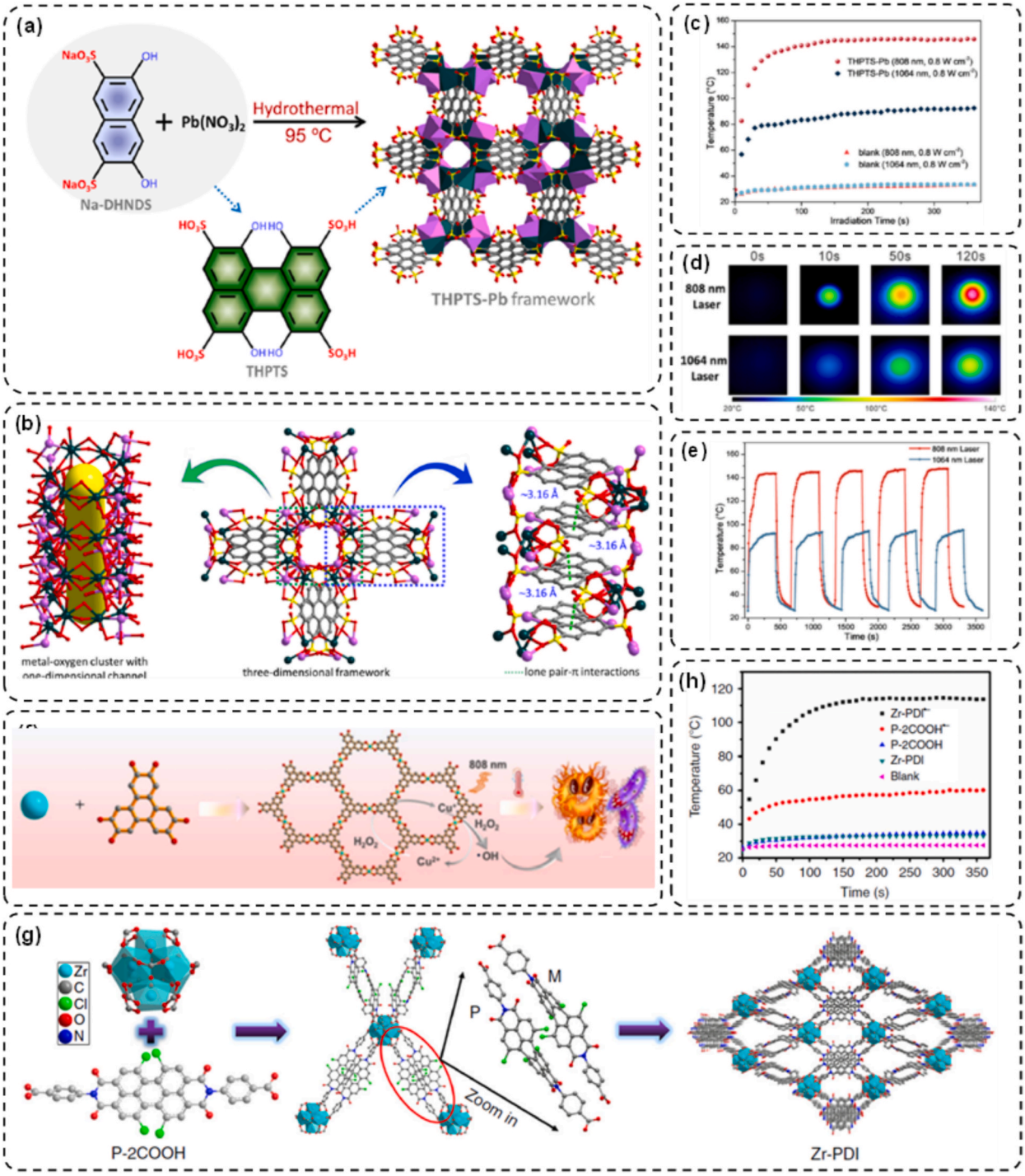

Fig. 6. (a) Schematic of the in situ hydrothermally synthesized THPTS-Pb framework [184]. (b) Structure and key interactions in the THPTS-Pb framework. Atom colors: Na (pink), Pb (dark blue), S (yellow), O (red), C (dark gray) [184]. (c) Photothermal response of THPTS-Pb film under 808 and 1064 nm laser irradiation [184]. (d) IR thermal images of THPTS-Pb film under 808 and 1064 nm laser illumination [184]. (e) Photostability of THPTS-Pb film during heating–cooling cycles [184]. Copyright 2024 American Chemical Society. (f) Schematic of the CHMOF framework [185]. Copyright 2024 Elsevier. (g) Schematic of the synthesis and structure of 3D porous Zr-PDI [186]. (h) Photothermal conversion curves of Zr-PDI$^{\bullet-}$ film [186]. Copyright 2019 Nature (Open Access).

often aimed at enhancing photoresponsive behaviors, provide valuable insights into the tunability and application of MOFs in photothermal-related processes. Collectively, these approaches reflect the broader goal of activating and optimizing the intrinsic or composite photoactive capabilities of MOFs for use in SAWH systems.

In the pursuit of developing efficient photothermal MOFs, selecting the most suitable organic ligand and metal cluster is the first crucial step. These components directly influence the MOF's ability to absorb light, convert it into thermal energy, and enhance its photothermal efficiency. A well-chosen inorganic cluster with the right electronic properties, coupled with an organic ligand that optimizes light absorption, forms the foundation for achieving effective photothermal performance in MOFs.

For instance, Cao et al. developed a dual-aromatic MOF ($Cu_{14}I_{14}$–CuTPyP) constructed from an inorganic aromatic copper-iodide cluster node ($Cu_{14}I_{14}$) and porphyrinic ligands, achieving an impressive NIR photothermal conversion efficiency of 63.77 % under 1064 nm laser irradiation. This high efficiency was attributed to extensive electron delocalization and ultrafast nonradiative relaxation (2.1 ps), demonstrating how deliberate selection of MOF building blocks can significantly enhance photothermal performance [201]. In another study, Liao et al. hydrothermally synthesized a distinctive THPTS-Pb MOF composed of 2,7-dihydroxynaphthalene-3,6-disulfonate (DHNDS) and $Pb(NO_3)_2$ (Fig. 6a) [202]. Its unique structure, consisting of alternating spatial arrangements of metal–oxygen clusters and perylene derivatives, allows for significant inherent charge transfer (CT). The crystal structure of THPTS-Pb,

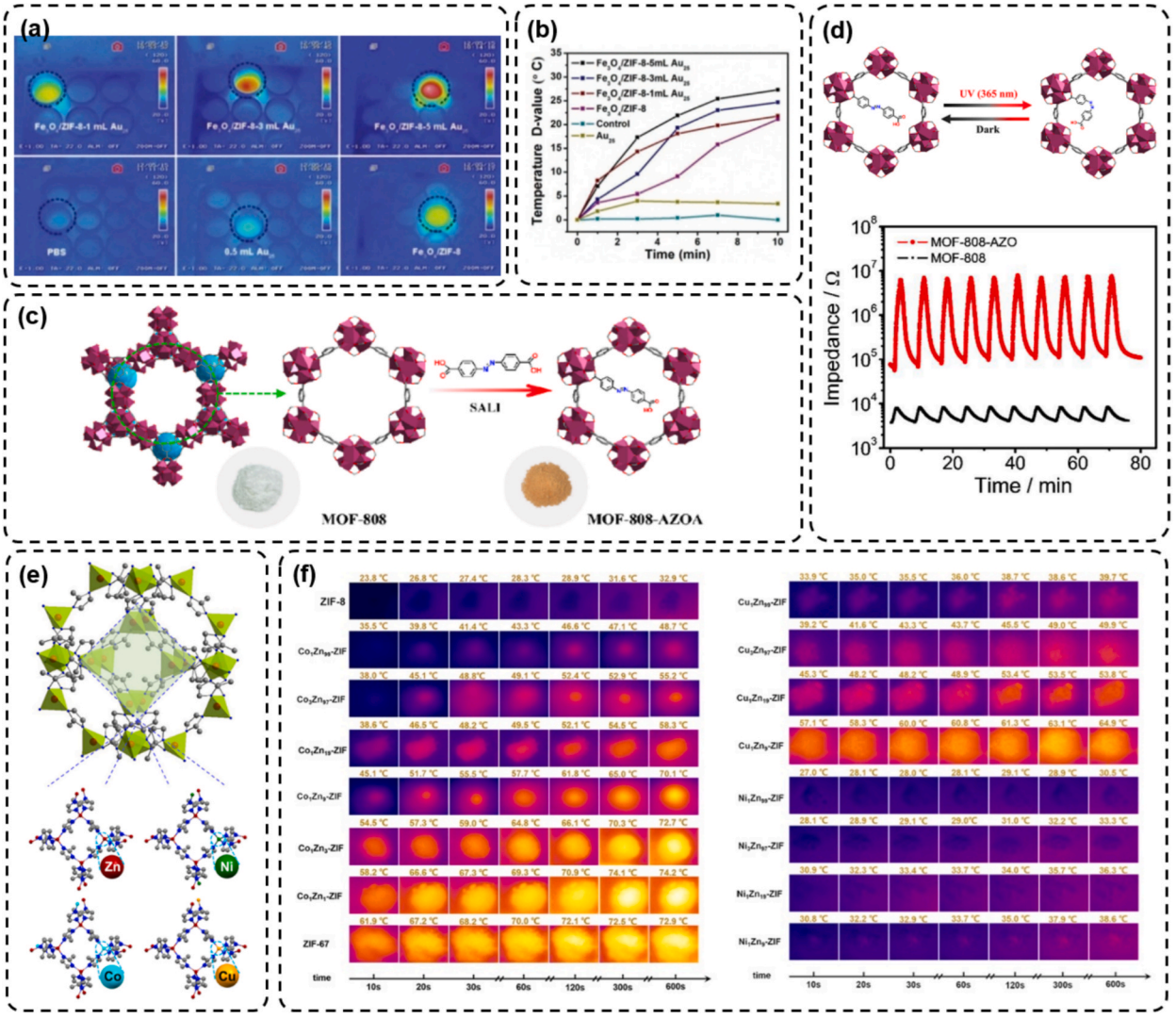

Fig. 7. (a,b) Infrared thermal photograph of a 96-well HeLa cell-culture plate after 808 nm NIR irradiation (0.5 W cm^{-2}) for 5 min and the corresponding temperature profiles [188]. Copyright 2015 Royal Society of Chemistry. (c) Schematic representation of the synthesis process of MOF-808-AZOA, with the inset displaying optical images of MOF-808 and MOF-808-AZOA [189]. (d) Comparison of the impedance response of MOF-808 and MOF-808-AZOA under 100 s of UV light irradiation per cycle, with the inset illustrating the cis − trans isomerization of the AZOA group in MOF-808-AZOA [189]. Copyright 2023 American Chemical Society. (e) Schematic of the crystal structures of ZIF-8 and M/Zn-ZIFs (M = Co, Ni, Cu) [190]. (f) Photos taken by an infrared camera for Co/Zn-ZIFs, Cu/Zn-ZIFs, and Ni/Zn-ZIFs during simulated sunlight irradiation [190]. Copyright 2023 Elsevier.

determined through X-ray diffraction, revealed a tetragonal framework with sodium and lead cations. The lead cation adopts a distorted pentagonal bipyramidal geometry, coordinating with oxygen atoms from hydroxyl and sulfonic acid groups, while the sodium cation coordinates with sulfonic acid and water molecules. These interactions result in a 1D metal–oxygen cluster with channels, as shown in Fig. 6b. The sodium and lead cations are bridged by oxygen atoms from THPTS molecules, and noncovalent lone pair-π interactions occur between the sulfonic acid oxygen and the aromatic perylene ring, as depicted in Fig. 6b. This results in a narrow band gap (1.11 eV) and excellent panchromatic absorption, including NIR photothermal conversion. The building blocks in this structure act as both electron donors and electron acceptors, contributing to effective charge separation. The material also shows excellent stability, retaining its air-, water-, and photo-stability, which is crucial for its photothermal applications. Upon 808 and 1064 nm laser irradiation, the MOF demonstrated effective photothermal conversion (Fig. 6c-e). The findings suggest that MOFs or coordination polymers incorporating both extended conjugated planes and electron-donating/accepting substituents can be designed to form materials with intrinsic CT and excellent photothermal properties, potentially advancing NIR photothermal conversion applications.

Building on this principle, other researchers have developed complementary strategies to exploit extended conjugated structures and donor–acceptor functionalities for NIR responsiveness. Gao et al. developed a novel NIR photoactive MOF (CHMOF) based on Cu^{+}/Cu^{2+} metal nodes and 2,3,6,7,10,11-hexahydroxytriphenylene organic ligands, which demonstrated excellent photothermal and photodynamic properties (Fig. 6f) [203]. The research demonstrated the material's ability to trigger photothermal therapy (PTT) under NIR light and enhance the Fenton effect, resulting in significant antibacterial activity. Lu et al. developed a three-dimensional MOF based on perylenediimide (PDI), termed Zr-PDI, constructed from the ligand N,N′-di-(4-benzoic acid)-1,2,6,7-tetrachloroperylene-3,4,9,10-tetracarboxylic acid diimide (P-2COOH) and $Zr_6(\mu_3\text{-}O)_4(\mu_3\text{–}OH)_4$ clusters (Fig. 6g) [204]. The twisted geometry of P-2COOH improves its solubility in polar media, facilitating successful formation of the MOF through solvothermal methods. Under near-infrared (NIR) laser exposure, a plain quartz glass exhibited a temperature increase of only 2.4 °C, whereas a quartz surface coated with Zr-PDI showed a 9 °C rise, attributable to the MOF's efficient NIR absorption (Fig. 6h). These results imply that the Zr-based framework incorporating PDI radical anions ($PDI^{\bullet-}$) exhibits remarkable photothermal conversion properties. Zirconium (Zr^{4+}) was chosen due to its proven stability and high porosity, contributing to the framework's ability to trap electron donors and facilitate the formation of radical anions in situ via photo-induced electron transfer (PET). The radical anions generated within the framework also exhibited high NIR photothermal conversion efficiency ($\eta = 52.3$ %). This exceptional efficiency was attributed to the high yield and stability of the radical anions, which form the basis for efficient NIR photothermal conversion. This work offers a simple and efficient strategy to stabilize radical anions at ambient conditions, which is significant for potential applications in photothermal therapy.

3.3.1. *Functionalization of MOFs*

MOFs can be functionalized to enhance their photothermal performance by modifying inorganic clusters, organic ligands, or pore structures, thereby improving solar absorption and its conversion into thermal energy.

Functionalizing inorganic clusters in MOFs is a powerful strategy to enhance their photoactive properties, enabling improved light absorption, CT, and responsive behaviors. For instance, Cheng et al. demonstrated a cluster functionalization strategy in MOF-808 by introducing ethylenediaminetetraacetic acid (EDTA) via post-synthetic modification, which enhanced both hydrophilicity and structural stability. The chelating ability of EDTA further enabled selective uptake of Cu^{2+} ions, followed by the in-situ formation of light-absorbing CuS NPs within the framework. This dual modification significantly improved water sorption performance and enabled solar-driven water release, providing a multifunctional platform for advanced AWH systems [69]. Similarly, Qin et al. performed post-synthetic functionalization of the metal clusters within a bimetallic FeAg-MOF, leading to the in-situ formation of Ag_2O NPs (~6 nm) confined within the MOF framework. This cluster functionalization enhanced solar light harvesting and promoted efficient photocatalytic microplastic upcycling coupled with hydrogen production [205].

Building on this concept, cluster-node functionalization has also been shown to boost photothermal performance. Yang et al. developed a multifunctional Fe_3O_4/ZIF-8-Au_{25} (IZA) nanoplatform, designed through a green and economical synthesis route [206]. This system effectively utilizes NIR light to trigger photothermal and photodynamic effects. The embedded Fe_3O_4 nanocrystals contribute to hyperthermia generation, while the ultrasmall Au_{25}-based clusters not only enhance the photothermal effect but also facilitate reactive oxygen species (ROS) production under NIR irradiation. This dual functionality significantly improves photothermal and photodynamic actions (Fig. 7a,b). The study underscores the importance of systematic nanoplatform design in optimizing photothermal performance, paving the way for MOF-based photothermal applications. In another example, Liu et al. introduced a novel approach for achieving light-responsive proton conduction in MOFs through cluster-node functionalization [207]. By grafting photoactive azobenzene-4,4′-dicarboxylic acid (AZOA) onto the $Zr_6(\mu_3\text{-}O)_4(\mu_3\text{-}OH)_4$ nodes of MOF-808 via terminal formate substitution, they obtained MOF-808-AZOA (Fig. 7c), which displayed reversible trans–cis isomerization upon UV irradiation, enabling switchable proton conduction with a high ON/OFF ratio, fast response time, and excellent reversibility (Fig. 7d). This study not only demonstrates the potential of cluster-node functionalization for designing stimuli-responsive MOFs but also highlights its relevance in developing photoactive MOFs with enhanced light absorption and energy conversion properties.

Doping strategies at MOF nodes provide another efficient strategy for improving the photothermal performance of MOFs. For instance, Li et al. investigated the photothermal disinfection capabilities of metal-ion-doped ZIF-8 MOFs (M/Zn-ZIFs) to address microbial contamination (Fig. 7e) [208]. By incorporating Co^{2+}, Ni^{2+}, and Cu^{2+} ions into ZIF-8 at varying concentrations, they systematically studied the effects of band structure modification, photothermal efficiency, and charge separation. Their findings revealed that metal ion doping enhances light absorption and promotes photothermal conversion. Notably, Co^{2+}-doped ZIF-8 (5 % doping) exhibited the highest photothermal efficiency under simulated sunlight (Fig. 7f). Adding metal ions at the MOF nodes can lead to the creation of heterometallic or mixed-metal MOFs, which are highly effective in improving the physical and chemical properties of the

materials. The introduction of different metal ions into the MOF nodes has been an effective way to enrich the topology and enhance the material's light-harvesting and energy-conversion properties. Recent developments have shown that the incorporation of metal ions into MOF nodes can improve light absorption, extend the photothermal response, and optimize CT processes. For example, mixed-metal MOFs such as Ce- and Ti-doped UiO-66-NH_2-type MOFs exhibit an improved ligand-to-cluster charge transfer (LCCT) process, which results in more efficient energy utilization and longer-lived charge-separated states, further enhancing the material's photoactive properties [209]. The synergy of different metal ions in these MOFs improves their efficiency for light absorption, heat generation, and energy transfer.

Beyond simple doping, introducing heterometallic or mixed-metal nodes can further enrich MOF topology and improve energy-conversion efficiency. For example, one study systematically examined a series of Ce-doped UiO-66-type MOFs using naphthalene-2,6-dicarboxylate (NDC) as the organic linker. By varying the Ce content from 0 to 100 %, the researchers evaluated how metal composition affects the structural, optical, and photodynamic behavior of the frameworks. The results revealed that at a Ce content of 9 %, the material exhibited optimal photocatalytic performance, achieving a 20 % increase in overall water-splitting efficiency compared to the undoped Zr-based MOF. This enhancement was attributed to more efficient photoinduced ligand-to-cluster CT and the formation of long-lived charge-separated states [210]. Additionally, trimetallic MOFs, which create a multi-electron-channel system, can accelerate the separation of charge carriers and improve the material's photothermal activity. For example, in trimetallic UiO-66 (Zr/Ce/Ti), the enhanced charge separation efficiency resulted in improved photoactive properties, allowing more effective utilization of light energy for heating applications [211].

Metal node functionalization with photosensitive species is another approach to enhancing the photothermal properties of MOFs. For instance, functionalizing MOFs like UiO-66 with Fe(III) ions demonstrated to extend the visible light absorption range, thereby improving the material's ability to absorb light. This is due to the metal-to-cluster charge transfer (MCCT) from Fe(III) to the Zr-oxo clusters, which results in the generation of holes that facilitate the oxidation of water and contribute to the overall photoactivity [212]. In a related study, a new Zr-based MOF featuring rare Zr_9 nodes with an (4,12)-connected topology was synthesized through a carefully designed ligand strategy that controlled the nuclearity of Zr-oxo clusters. Post-synthetic incorporation of Fe(III) onto these Zr_9 nodes significantly enhanced the MOF's photocatalytic activity and selectivity in the oxidation of toluene. This enhancement was attributed to optimized binding sites for Fe(III) and efficient C–H activation under light irradiation. The study highlights the potential of MOFs with tunable cluster nuclearity as structurally well-defined platforms for mechanistic investigations in photocatalysis [213]. Organic post-modification of MOFs is also a promising approach for improving metal node functionalization in confined spaces. For example, the integration of perylene-based photosensitizers into MOF-520 allows for better spatial distribution of the photosensitive species [214]. This leads to enhanced photoactive properties, as the well-distributed photosensitizers within the MOFs can effectively absorb light, without undergoing aggregation, thereby improving the overall photoactive response.

While the inorganic metal centers in MOFs often behave similarly to semiconductor quantum dots, the organic linkers primarily function as light-absorbing antennae that facilitate the capture and transport of charge carriers. *Organic ligand functionalization,* either by in-situ or post-modification methods [215 216], therefore represents a powerful strategy to improve photoactive properties.

First, ligand functionalization can be achieved during the in-situ preparation of MOFs. For instance, Cu^{2+} ions were in-situ introduced into the porphyrinic linker of PCN-224 during the MOF synthesis, effectively metallating the ligand and enhancing its visible-light absorption [217]. This metalation suppresses electron-hole recombination and facilitates CT under light irradiation, thereby improving the overall photoactivity and photothermal performance of the MOF. Another highly effective approach for in situ ligand functionalization involves incorporating electron-donating substituents during MOF synthesis to enhance light absorption properties. A notable example is the replacement of 1,4-benzenedicarboxylic acid (BDC) with amino-functionalized NH_2-BDC in MIL-125(Ti), where the $–NH_2$ group directly into the linker backbone alters the electronic structure of the MOF, leading to a red-shift in light absorption into the visible region [218 219 220 221]. A similar in situ ligand modification strategy has been applied to the synthesis of NH_2-UiO-66(Zr), resulting in a visible-light-responsive material, in contrast to the UV-absorbing parent UiO-66(Zr). The enhanced light absorption in the visible region arises from the electron-donating nature of the $–NH_2$ group, which interacts with the π^*-orbitals of the benzene ring in the linker. This interaction leads to an elevation of the HOMO energy level, effectively narrowing the band gap and shifting the absorption spectrum toward the visible region [222 223 224 225]. This amino-functionalization strategy has also been extended to Fe-based MOFs such as MIL-101(Fe), MIL-53(Fe), and MIL-88B(Fe), leading to broadened and intensified absorption in the visible-light region [226]. This red-shift and increased optical response are due to dual excitation mechanisms: direct excitation of Fe-O clusters and excitation of the amine-modified linker, followed by electron transfer. Thus, in situ modification of linkers with $–NH_2$ groups offers a versatile route to tune molecular orbital energy levels and enhance photophysical properties.

Ligand functionalization of MOFs can also be achieved by post-modification of MOFs. In one study, Wu et al. introduced aromatic heterocycles to NH_2-MIL-125(Ti) by performing Schiff base reactions, resulting in functionalized frameworks such as QUI-MIL-125 (Ti), where QUI represents 2-quinolinecarboxaldehyde [227]. Computational analysis using DFT revealed a noticeable narrowing of the band gap and improved absorption in the visible region, attributed to the strong π-conjugation between the ligand and MOF backbone. HOMO-LUMO distributions further supported these electronic enhancements. Expanding on this concept, incorporating donor–acceptor (D-A) units into MOFs has emerged as a powerful route for boosting light absorption, charge mobility, and energy transfer processes. Upon illumination, such D-A systems can sustain long-lived charge carriers and efficient separation, contributing to enhanced photothermal performance. For instance, Jin et al. synthesized a D-A-D-type organic ligand based on a pyrazole–benzothiadiazole-pyrazole motif, which was used to construct the MOF JNU-204 [228]. Owing to its broad light absorption, suitable band alignment, and fast charge dissociation, JNU-204 exhibited high photothermal efficiency in catalytic applications. In another study, Xu et al. created a donor–acceptor MOF by integrating a porphyrin-based donor ligand (H_2DPBP) into a Zr-MOF featuring a naphthalene diimide (NDI) acceptor, resulting in the composite Zr-NDI-H_2DPBP [229]. Both theoretical and

experimental assessments confirmed their strong photothermal behavior. Additionally, mixed-ligand strategies have been explored to construct D-A frameworks. Fiankor et al. embedded porphyrin acceptor ligands (H_2TCPP/NiTCPP) within a N,N′-bicarbazole-donor-based Zr-MOF named NPF-500 [230]. Owing to the specific positioning of coordinated unsaturated sites (CUS) in the octahedral cage structure, the porphyrin ligands were accurately incorporated. The effective spectral overlap between donor emission and acceptor absorption facilitated efficient energy transfer under light exposure, leading to superior photothermal output. Yan et al. designed and synthesized a novel Zn-based MOF by incorporating both tetrathiafulvalene tetrabenzoate acid (H_4TTFTB) as an electron donor and N, N′-bis(4-pyridylmethyl)-1,4,5,8-naphthalene diimide (bpmNDI) as an electron acceptor (Fig. 8a) [231]. The unique 2-fold interpenetration of the structure, along with the flexibility of the bpmNDI ligand, allowed TTF and NDI moieties from different frameworks to align face-to-face, forming a well-defined D-A arrangement. The nearly parallel orientation of TTF and NDI, with a spacing of 3.673 Å and a dihedral angle of approximately 3.542°, further confirmed the presence of strong D-A and π-π interactions, resulting in broad NIR absorption and efficient photothermal conversion. As shown in Fig. 8b, the HOMO orbitals were primarily localized on the electron-donating TTF units, while the LUMO orbitals were concentrated on the electron-accepting NDI units. The energy gap of 1.51 eV between HOMO and LUMO was significantly lower than that of the individual organic ligands, explaining the enhanced CT at the molecular level. To assess the NIR photothermal performance of the synthesized Zn-MOF, temperature variations were monitored under laser irradiation using an IR thermal camera. This imaging technique provided a clear visualization of the material's heating behavior under 808 nm laser exposure (Fig. 8c). When irradiated with a laser at a power density of 0.4 W.cm^{-2}, the powder's temperature rapidly increased from room temperature to 247.6 °C within 15 s, ultimately reaching approximately 255 °C after 24 s. Once the laser was turned off, the material cooled down swiftly, demonstrating efficient and reversible photothermal conversion. For comparison, the background temperature remained nearly unchanged under identical conditions, confirming the material's exceptional photothermal response. This study highlights the importance of donor–acceptor design in creating MOFs with advanced photothermal responses.

3.3.2. *Encapsulation of species in MOFs*

In addition to modifying the organic linkers, *tailoring the pore environment* of MOFs, offers a promising route to enhance photothermal efficiency. One approach involves incorporating molecular photoactive units into the cavities of the MOF framework, thereby transforming them from homogeneous to heterogeneous systems. This not only improves light absorption but also promotes spatial separation of charge carriers. Alternatively, nanoscale entities such as metal nanoparticles or semiconductor materials can be embedded within the pores to create heterojunction interfaces with aligned energy levels, facilitating more efficient charge separation. This section highlights pore-level functionalization strategies that exert the most pronounced impact on MOF performance. Notably, integrating photoresponsive components into the porous matrix is a key method for improving photothermal behavior, and this is effectively achieved through targeted tuning of the pore space. For example, Qiu et al. employed a facile pore functionalization strategy by integrating ultrasmall (<5 nm) silver NPs (Ag NPs) into the cavities of Zr-TTFTB (TTFTB = tetrathiafulvalene tetrabenzoate) via a double-solvent impregnation followed by chemical reduction. This composite showed strong photocatalytic activity for the degradation of the antibiotic sulfamethoxazole (SMZ) under visible light. It maintained high performance across a wide pH range (3.0–9.0) and after four reuse cycles, with minimal leaching (Ag 0.18–0.61 % and Zr 0.01–0.05 %), indicating excellent chemical stability. Mechanistic studies suggested that the heterojunction between Ag NPs and the TTFTB-based MOF promotes efficient electron

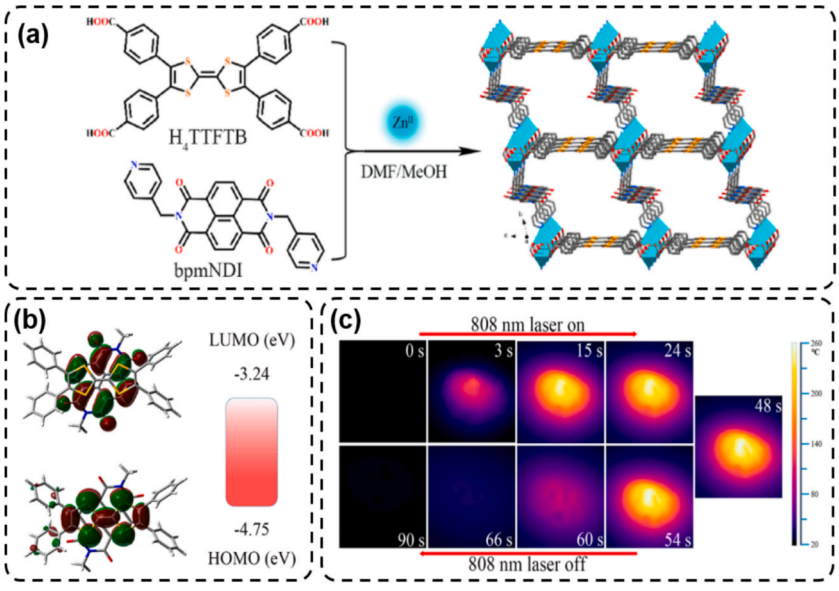

Fig. 8. (a) Schematic representation of the synthesis of Zn-MOF [213]. (b) Molecular orbital diagrams and calculated energy diagrams of Zn-MOF [213]. (c) Thermal images of Zn-MOF powder under 808 nm irradiation (0.4 W cm^{-2}) [213]. Copyright 2022 American Chemical society.

transfer and generates ROS, which are key to the observed photocatalytic degradation. In another study, Wang et al. introduced a bioinspired MOF cocrystal ($Ni_3(HIB)_2$-CHL) formed by the co-assembly of the MOF [Ni_3(hexaiminobenzene)$_2$, $Ni_3(HIB)_2$] and p-chloranils (CHLs) [232]. This cocrystal, due to its 2D conjugated nature and the formation of persistent anion radicals, exhibits excellent photothermal properties, making it highly effective for solar-driven interfacial water evaporation. The presence of organic anion radicals in $Ni_3(HIB)_2$-CHL was confirmed through Electron Paramagnetic Resonance (EPR) spectroscopy, revealing a sharp peak with a *g* value of 2.002, indicating the formation of anion radicals. These radicals are believed to inhibit radiative transitions, thereby enhancing the photothermal conversion capability of the material. The broad absorption spectrum in the visible to NIR (vis-NIR) range further supports the material's excellent photothermal properties. Upon exposure to sunlight, the temperature of $Ni_3(HIB)_2$-CHL increases rapidly, showcasing its ability to efficiently convert solar energy. This material was tested for its solar-driven interfacial water evaporation performance by loading it onto cotton fabrics. Under one-sun illumination, a cotton cloth loaded with 30 mg of $Ni_3(HIB)_2$-CHL demonstrated an evaporation rate of 4.04 $kg.m^{-2}h^{-1}$, one of the highest reported values for photothermal materials. This research demonstrates the design and production of photothermal cocrystal materials with high water transport rates and outstanding solar-driven evaporation performance, offering promising potential for applications in water purification and desalination technologies. Lu et al. adopted a partial ligand substitution approach to encapsulate the metallophthalocyanine molecule Zn-H_4Pc (H_4Pc = 2,9,16,23-tetrakis(4-pentyloxycarbonyl)-phthalocyanine) with excellent light-harvesting ability into the pore of UiO-67 [233]. Under the synergistic effect of separated charge carriers generated by the photoexcited ZnPc moieties, UiO-67-ZnPc exhibited significantly enhanced photoactive behavior, resulting in an improved photothermal response. A versatile template-directed synthesis approach

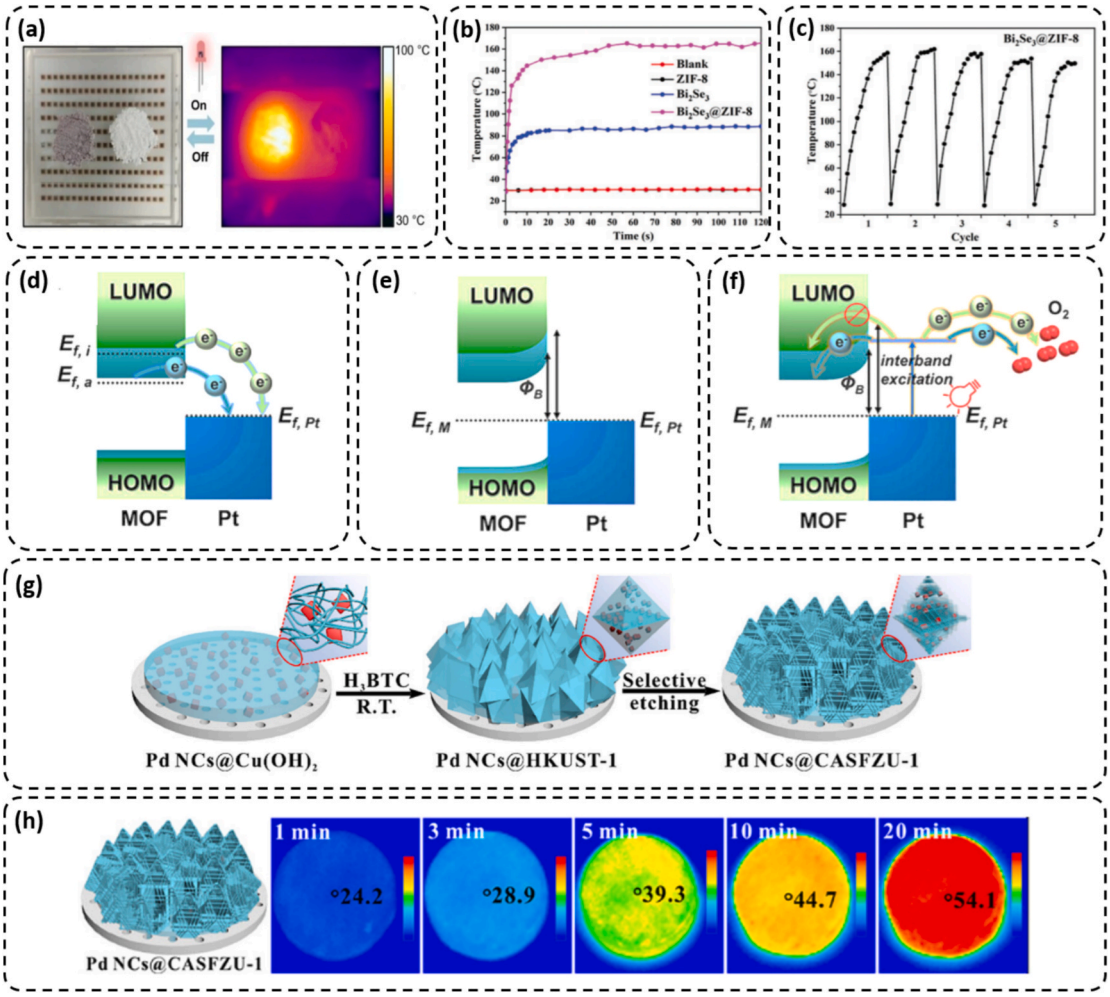

Fig. 9. (a) IR and visible images of AuBP@UIO-66 and UIO-66 before and during IR LED exposure (LED area: 5 cm^2) [224]. Copyright 2024 Nature. (b) Temperature rise of blank, ZIF-8, Bi_2Se_3, and Bi_2Se_3@ZIF-8 under 808 nm laser irradiation (0.65 W cm^{-2}, 2 min) [226]. (c) Photothermal stability of Bi_2Se_3@ZIF-8 over multiple irradiation cycles [226]. Copyright 2021 Royal Society of Chemistry. (d–f) Schematic band diagrams for Pt/MOF systems: (d) Schottky junction formation via electron transfer from MOF to Pt; (e) Fermi level alignment; (f) electron migration from Pt interband excitation under light. Green and cyan represent inert (ZIF-8) and active (UiO-66, MIL-125) MOFs, respectively [227]. Copyright 2022 WILEY. (g) Schematic of Pd NCs@CASFZU-1 synthesis [229]. (h) IR thermal images of Pd NCs@CASFZU-1 composite films under continuous light irradiation [229]. Copyright 2024 WILEY.

using homogeneous photoactive species as structure-directing templates has also been developed to prepare new types of MOFs with encapsulated photoactive species. For example, a polypyridine ruthenium (II) complex, $[Ru\text{-}(bpy)_3]^{2+}$ (bpy = 2,20-bipyridine), can be successfully immobilized into a series of MOFs with zeolite-like structures [234]. Due to the well-dispersed photoactive $[Ru\text{-}(bpy)_3]^{2+}$ and the facilitated mass transport induced by the high porosity of MOFs, the obtained $Ru(bpy)_3$@MOFs exhibited outstanding photoactive performance. Additionally, a series of dyes@UiO-66 s were prepared by encapsulating fluorescein (FL), rhodamine B (RhB), or eosin Y (EY) into the porosity of UiO-66 and Bim-UiO-66 [235]. These robust dyes efficiently sensitize the MOF hosts, significantly influencing their band structures and corresponding photoactive properties. Among these, FL@Bim-UiO-66 demonstrated superior photothermal activity for the green synthesis of various [1,2,5]thiadiazole[3,4-g]benzoimidazoles, offering excellent yields (498 %), stability, and reusability.

Pore space functionalization of MOFs through integration with bimetallic NPs is another promising approach to optimize their photoresponse properties. For instance, Sun et al. with a chemical reduction process, encapsulated bimetallic CuPd nanoclusters into the pore space of NH_2-UiO-66(Zr) by combining the double-solvent impregnation method [236]. The encapsulated Cu acted as an electron mediator, promoting CT from the photoexcited MOF to the metallic Pd. As a result, CuPd@NH_2-UiO-66(Zr) showed enhanced photoresponse performance in contrast to the single metal-incorporated Pd@NH_2-UiO-66(Zr) counterpart [236 237]. Finally, Fang et al. functionalized the pore space of a type of MOF (Zr-ferrocene (Zr-Fc)) with phosphomolybdate (PMo_{12}) via electrostatic interactions method. By combining the abundant Lewis sites provided by PMo_{12} with the high photothermal effect of Zr-Fc MOFs, the resulting PMo12@Zr-Fc MOF showed suitable photothermal properties [238].

3.3.3. *Mof-based composites*

The integration of MOFs with functional components such as plasmonic NPs, semiconductors, and covalent organic frameworks (COFs) has led to the emergence of advanced composite materials with superior photothermal and light-harvesting capabilities. These MOF-based composites capitalize on the synergistic interactions between the framework and the guest materials, resulting in enhanced charge separation, broadened light absorption, and improved thermal conversion. In the following, we will refer to some of these studies.

Plasmonic NPs improve light absorption while maintaining their redox capabilities [239]. Schottky junctions can form between NPs and MOFs, which enhance charge carrier separation and transfer [240 241]. Additionally, the interaction between NPs and the MOF support can mediate the electronic properties of the metal, influencing its overall photoactive behavior. Shelonchik et al. developed a novel, rapid light-induced synthesis method for MOFs by leveraging the plasmonic photothermal properties of bipyramidal gold NPs (AuBPs) [66] using of four different MOFs (UIO-66, MIL-88A, HKUST-1, and MOF-5) and different photothermal agents and wavelengths (520, 660, and 850 nm). Notably, photothermal synthesis was significantly faster than conventional solvothermal methods, improving the efficiency of the reaction. By controlling light exposure, AuBPs can either be embedded within the MOF structure or remain in the supernatant. An example of this is the AuBP@UIO-66 composite, where AuBPs were embedded in the MOF, retaining their plasmonic properties and contributing to the enhanced photothermal response. The photothermal AuBP@UIO-66 showed remarkable heating capabilities, making it useful for ultrafast desorption and MOF activation (Fig. 9a). The photothermal activation process not only reduced synthesis time but also maintains the structural integrity of the MOF, as evidenced by stable S_{BET} and PXRD after repeated activation. The approach opens new possibilities for efficient MOF synthesis and applications in areas such as photothermal desorption, MOF activation, and catalysis, showcasing the potential for the combination of photothermal materials and MOFs in a wide range of applications.

Using an in-situ assembly of MOFs and distinct heterogeneous heating under visible light [242], Biswas et al. employed a cobalt chloride molecular complex as an efficient and stable light-to-heat converter to initiate the formation of MOFs. This study revealed that photothermal activation plays a key role in the formation of MOF superstructures, with the MOF crystals themselves acting as additional photothermal agents. Furthermore, palladium NPs (PdNPs) were used as competing photothermal agents, shedding light on the dynamics between different heat sources within the reaction, leading to the formation of MOF-NP composites. The versatility of this photothermal approach was demonstrated in the light-assisted synthesis of the cobalt-2,5-dihydroxyterephthalate Co-DHBDC, where different light-to-heat converters were employed at two distinct wavelengths, 520 and 660 nm. The cobalt chloride complex was found to be highly efficient and stable, enabling remote control over the temperature and reaction activation. Depending on the wavelength used, Co-DHBDC could form individual rods or assemble into larger superstructures. Additionally, the study tested the hypothesis that newly formed MOF particles function as photothermal agents (PTAs), which promoted further growth of superstructures. Similarly, Sun et al. constructed a composite material, Bi_2Se_3@ZIF-8 NPs, using a one-pot method to enhance the photothermal conversion efficiency of Bi_2Se_3 NPs [152]. The heterostructure formed between Bi_2Se_3 and ZIF-8 effectively prevented the radiative recombination of hot electrons and holes, significantly boosting the photothermal effect. The temperature of the Bi_2Se_3@ZIF-8 NPs increased to 130 °C within 6 s and stabilized at 165 °C, showcasing a remarkable enhancement in photothermal performance (Fig. 9b). Additionally, the composite maintained its structural integrity and photothermal conversion capacity after multiple irradiation cycles, making it a promising candidate for photothermal applications (Fig. 9c).

Supports that lack redox activity typically offer limited benefits in enhancing photothermal performance, as their electronic coupling with metal species is relatively weak. For instance, Sun et al. [185], both inert and redox-active MOFs were employed as platforms for immobilizing platinum nanoparticles (Pt NPs) to assess their photoactivity. Interestingly, the Pt-loaded inert MOF (Pt/ZIF-8) exhibited significantly higher catalytic efficiency in the aerobic oxidative coupling of benzylamine compared to its counterparts, Pt/UiO-66 and Pt/MIL-125, which are based on redox-active MOFs. The integration of Pt NPs with MOFs leads to substantial modulation of their electronic and optical behavior. As depicted in Fig. 9d, the difference in Fermi levels between Pt and the MOF framework induces electron transfer from the MOF to Pt, effectively altering the local electron density and band alignment. This results

in the formation of Schottky barriers with material-dependent heights (Fig. 9e), which significantly influence the direction and efficiency of charge carrier movement under illumination. Upon visible-light irradiation, interband excitation of Pt generates hot electrons, which may be injected back into the MOF LUMO levels (Fig. 9f), depending on the energetic alignment. In the case of Pt/ZIF-8, the LUMO lies far above Pt's Fermi level, restricting back-transfer and confining photoexcited electrons near the metal surface. In contrast, Pt/UiO-66 and Pt/MIL-125, with LUMO levels closer to Pt's Fermi level, allow partial electron reinjection into the MOF, leading to distinct light-induced charge dynamics across the composite interface. These interactions modify the photo-response profile of the system, indicating that even optically inert MOFs like ZIF-8 can exhibit altered light absorption and charge behavior through interfacial engineering with plasmonic or semi-plasmonic metals.

Wang et al. introduced a straightforward dissolution-coordination approach to integrate octahedral Cu_2O nanocrystals within the framework of HKUST-1 MOF [199]. By precisely regulating the interplay between the etching of Cu_2O and the concurrent growth of the MOF shell, they achieved directed assembly of HKUST-1 around the nanocrystals. Subsequent in situ reduction during the hydrolysis of NH_3BH_3 led to the formation of a Cu@HKUST-1 composite that preserved its structural integrity. Notably, this composite outperformed its conventionally prepared counterpart, Cu/HKUST-1, in which copper particles are randomly distributed, in terms of both photothermal efficiency and durability in single-step catalytic reactions. This improvement stems from the synergistic interaction between the photothermal properties of metallic copper and the structural advantages provided by the MOF. Zhu et al. explored the incorporation of metal NPs (MNPs) into 3D-stacked-MOF nanosheet (CASFZU-1) and was explored to enhance photoactive property of MOF (Fig. 9g) [243]. The challenge addressed was the optimization of 3D nano-architectures for efficient light harvesting. It was reported that this structure enabled the uniform encapsulation of MNPs, thereby enhancing broadband light absorption, as evidenced by IR thermal imaging (Fig. 9h). In a different strategy, core–shell nanowires composed of Ag cores coated with a ZIF-8 shell have been effectively utilized to separate trace amounts of bioalcohols from water [244]. The ZIF-8 shell imparts high adsorption efficiency to the nanocomposite, while the inherent photothermal properties of the silver nanowires enable easy regeneration and recyclability by facilitating the release of bioalcohols from the MOF structure upon light irradiation. In another example, single gold nanorods (Au NRs) encapsulated within ZIF-8 NPs demonstrate a finely tunable photothermal response paired with impressive drug-loading abilities [245]. This system allows for controlled drug release triggered by changes in pH, highlighting its potential in targeted delivery applications.

Semiconductors have attracted significant attention due to their ability to enhance the photothermal properties of materials. MOFs can exhibit improved photothermal behavior when combined with semiconductors, forming composites that exhibit synergistic effects. In particular, the creation of heterojunctions within these composites facilitates the efficient migration of charge carriers between the conduction and valence bands of the components [246]. For instance, CdS, a semiconductor known for its strong light-harvesting capacity in the visible light region, has been used extensively to improve the photoactive properties of different materials [247]. In this sense, Wu et al. successfully incorporated CdS quantum dots (QDs), only a few nanometers in size, into the MIL-101

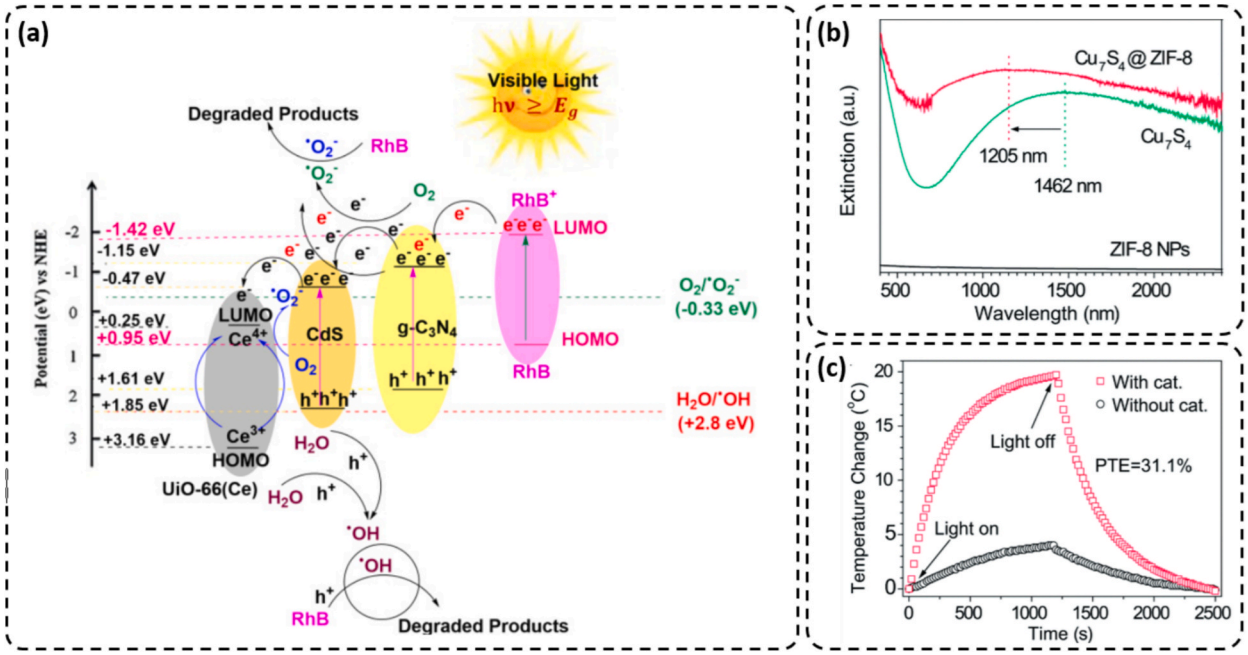

Fig. 10. (a) Proposed mechanism illustrating the degradation pathway of Rhodamine B (RhB) under visible light irradiation using the UiO-CdS-CN-5 nanocomposite, highlighting the role of various reactive species [240]. Copyright 2025 Elsevier (Open Access). (b) Extinction spectra of Cu_7S_4, ZIF-8, and Cu_7S_4@ZIF-8 NPs, measured by dispersing the materials in a KBr matrix [243]. (c) Steady-state temperature profiles of dichloromethane solutions with and without Cu_7S_4@ZIF-8 NPs under 1450 nm laser irradiation (500 mW cm^{-2}), demonstrating the photothermal heating effect of the nanocomposite [243]. Copyright 2016 Royal Society of Chemistry (Open Access).

(Cr) using a double-solvent method [159]. The resulting CdS@MIL-101 composite showed significantly enhanced performance in photocatalytic imine synthesis, including both symmetrical and asymmetrical types, through coupling reactions involving amines and alcohols or via self-coupling of amines. This enhancement was mainly attributed to improved light-harvesting ability and the strong interfacial interaction between CdS QDs and the MOF, which facilitated charge generation and separation compared to the bare MOF. With a therapeutic aim, Liu et al. designed a multifunctional nanocomposite, Cu-BTC@PDA, by combining Cu-BTC with polydopamine (PDA) to enhance the photothermal therapy (PTT) and chemodynamic therapy (CDT) [71]. Density Fumctional Theory (DFT) calculations revealed that the plasmonic vibrations from the Cu d-d transitions in Cu-BTC@PDA enhanced the photothermal performance of PDA. In an acidic tumor microenvironment, Cu^{2+} ions released from Cu-BTC@PDA were reduced to Cu^{+} by glutathione (GSH), which then catalyzed hydrogen peroxide (H_2O_2) to generate hydroxyl radicals, synergizing with PTT for effective melanoma therapy. Carbon nitride (C_3N_4), a polymer semiconductor, is another promising material for improving the photoactive properties of MOFs [248 249]. C_3N_4 is known for its stability, simple synthesis, and potential as a photoactive material when integrated with MOFs [250 251]. Liu et al. achieved a successful combination of UiO-66-NH_2 with hexagonal phosphorus-doped tubular C_3N_4 (p-TCN) via a solvothermal method [252]. The composite exhibited improved light-harvesting capacity and efficient CT between p-TCN and UiO-66-NH_2, enhancing its photoactive properties. In a recent investigation, Yassin et al. introduced a novel ternary nanocomposite based on UiO-66(Ce), CdS, and g-C_3N_4, aimed at enhancing visible-light-driven photocatalysis [190]. UiO-66(Ce), a Ce-based MOF, was chosen due to its notable redox properties, efficient ligand-to-metal CT, and strong electron-hole separation ability. Based on the analysis, the proposed electron–hole transfer mechanisms are illustrated in Fig. 10a. The CN component, due to its narrow band gap, responds effectively to visible light, allowing excitation of electrons from its valence band (VB) to conduction band (CB). Since the CB of CN (−1.15 eV vs. NHE) is more negative than those of CdS (−0.47 eV) and UiO-66 (+0.25 eV), the photoexcited electrons in CN cascade toward CdS and further into the MOF, driven by internal electric fields in the multi-component structure. These electrons are also capable of transferring to the LUMO of UiO-66′s BDC linker or to Ce-oxo clusters via LMCT, modulating the redox state of Ce. In addition, UiO-66′s VB edge (+3.16 eV vs. NHE) is suitably aligned to oxidize water and hydroxide ions into hydroxyl radicals, emphasizing the strong oxidizing potential of its photogenerated holes. In contrast, CN's less positive VB (+1.61 eV) means its holes contribute less directly to oxidative reactions. CdS, with a narrow band gap (2.32 eV), absorbs visible light efficiently, generating photoinduced electrons and holes. Overall, the system demonstrated efficient charge separation and directional migration of photogenerated carriers. In another study, Daliran et al. encapsulated the nontoxic, lead-free halide perovskite semiconductor $CsCu_2I_3$ into the channels of the highly stable mesoporous MOF PCN-222(Fe) using an antisolvent/inverse solvent infiltration method [253]. The resulting composite, $CsCu_2I_3$@PCN-222(Fe), demonstrated enhanced photoactive properties, benefiting from the synergistic effects between $CsCu_2I_3$ and PCN-222(Fe).

Semiconductor materials are also advantageous for utilizing NIR light, thanks to their high extinction coefficients and wide band tunability. For example, copper chalcogenides exhibit photothermal properties like those of gold NPs [254]. Wang et al. constructed a core–shell Cu_7S_4@ZIF-8 nanostructure, where the Cu_7S_4 core provided photothermal functionality and the ZIF-8 shell contributed to charge carrier separation [160]. As shown in Fig. 10b, the Cu_7S_4@ZIF-8 structures exhibit a broad extinction band in the NIR region, unlike conventional copper sulfide nanocrystals that typically show sharper peaks. This broadening is likely due to the combined effects of plasmonic nanocrystal behavior and the optical resonance within the hollow cavity. Upon forming the core–shell Cu_7S_4@ZIF-8 structure, a blue shift in the plasmonic band was observed, attributed to the reduction in the surrounding dielectric constant (from 2.43 in KBr to 1.8 in ZIF-8). Interestingly, this core–shell architecture showed enhanced light absorption compared to the sum of the individual Cu_7S_4 and ZIF-8 components, suggesting a synergistic optical effect that improves light-harvesting efficiency. Photothermal performance was evaluated by irradiating a dispersion (2.5 g L^{-1}) of Cu_7S_4@ZIF-8 under NIR light, yielding a photothermal conversion efficiency (η) of 31.1 % and a maximum temperature increase (ΔT) of 19.8 °C (Fig. 10c). In contrast, the control sample without the composite showed only a minimal temperature rise, confirming that the observed photothermal effect arises predominantly from the Cu_7S_4@ZIF-8 nanostructure.

Apart from conventional semiconductors, certain carbon-based materials like CB have also been utilized to enhance the photothermal performance of MOF composites. CB acts primarily as a broadband photothermal agent, converting absorbed solar energy directly into heat. This property makes it particularly useful in applications such as water harvesting, where thermal desorption is crucial. For instance, Tian et al. developed a MOF-303@LiCl composite by incorporating LiCl into MOF-303 and further enhanced its performance with the addition of CB [116]. The resulting composite demonstrated a high-water uptake capacity and rapid desorption under one-sun illumination, reaching temperatures up to 66.1 °C without optical focusing. This enabled efficient water release within 60 min and supported multiple adsorption–desorption cycles daily, showcasing its potential for SAWH under real-world conditions.

As a new class of porous organic polymers, COFs have shown great promise in enhancing the photothermal properties of materials due to their high surface area, excellent chemical stability, and tunable CT properties [255 256 257]. Composites of MOFs with COFs allows for the retention of the unique characteristics of both components, such as abundant active sites and large surface areas, while also improving the overall photoactive behavior of the material [258 259]. Currently, core–shell MOF@COF composite materials are commonly fabricated by grafting amino-functionalized MOFs with imine-based COFs [169 260 261]. For instance, Zhang et al. synthesized a core–shell composite material (NH_2-MIL-68@TPA-COF) by integrating a COF shell onto a MOF core [262]. This combination significantly enhanced the surface area (from 450 to 540 $m^2\ g^{-1}$), introduced hierarchical porosity, and reduced the band gap (from 2.82 to 2.21 eV), thereby improving visible-light absorption. This improvement confirms that COF integration can boost the photoactivity and porous architecture of MOFs. Sun et al. developed a composite material (TiATA/LZU1) by growing a COF shell on a Ti-based MOF (TiATA) and further doped it with palladium to obtain Pd/TiATA/LZU1 [263]. The introduction of the COF layer significantly improved the material's photoactive efficiency. Mechanistic studies showed that the COF acted as an electronic mediator, enhancing CT and enabling a donor-mediator-acceptor system. Lu et al. introduced a simple seed growth method, utilizing the

chemical Schiff base reaction between the aldehyde groups in the COF and the amino groups on the MOF to coat the NH_2-MIL-125 MOF with COF TAPB-PDA, resulting in the NH_2-MIL-125@TAPB-PDA composite structure [169]. Notably, the thickness of the COF shell can be controlled by varying the concentration of COF monomers. The enhanced photoactive performance of the MOF@COF composite was attributed to the accelerated transfer of photoactive charge carriers (e^- and h^+) between the MOF core and the COF shell through the formation of covalent bonds. Another example of a core–shell MOF@COF composite was reported by Zhang et al., where they used NH_2-MIL-125 (Ti-MOF), which contains amino functional groups for covalent bonding, as the core, and TpTt-COF, functionalized with triazine and keto groups, as the shell [261]. The composite was prepared by reacting Ti-MOF with 2,4,6-triformylphloroglucinol (Tp), creating Ti-MOF-CHO with covalent connecting sites. Tuning the proportion between Ti-MOF-CHO and TpTt-COF precursors allows the formation of a nanobelt-shaped TpTt shell with reduced thickness and enhanced exposure of active sites. The improved photoactive properties were due to the efficient migration of photoinduced electrons from the Ti-MOF core to the TpTt shell, concentrating the electrons on the surface and enhancing the overall photothermal activity of the composite. The Ti-MOF@TpTt composite exhibited significantly improved performance than individual Ti-MOF or COF components, demonstrating the synergistic effect in enhancing the photoactive capabilities of the system.

4. Critical Factor: Stability of MOFs

The long-term reliability of sorbent materials is a defining requirement for the practical deployment of MOF-based SAWH systems. Beyond adsorption capacity and kinetics, the stability of MOFs under real operating conditions, ranging from continuous exposure to water vapor to repeated thermal cycling and outdoor solar irradiation, plays a critical role in determining overall device performance and lifetime. This section examines three key dimensions of MOF stability essential for SAWH applications: water stability, thermal stability, and UV stability.

4.1. Water stability

A simple and straightforward experimental approach to assess the hydrolytic stability of MOFs involves exposing them to a specific concentration of water vapor and then comparing the XRD patterns of the exposed samples with those of the original samples. While this approach is widely adopted, it provides only a partial picture of stability since hydrolytic degradation may also involve defect formation, compositional changes, or other structural modifications that are not always detectable by diffraction techniques, requiring further characterization (surface, composition, etc).

Based on such XRD-based evaluations, early studies showed that most MOFs were not hydrolytically stable, which posed a major challenge for their use in AWH systems. Although hydrolysis of MOFs is possible under prolonged exposure to humidity, elevated

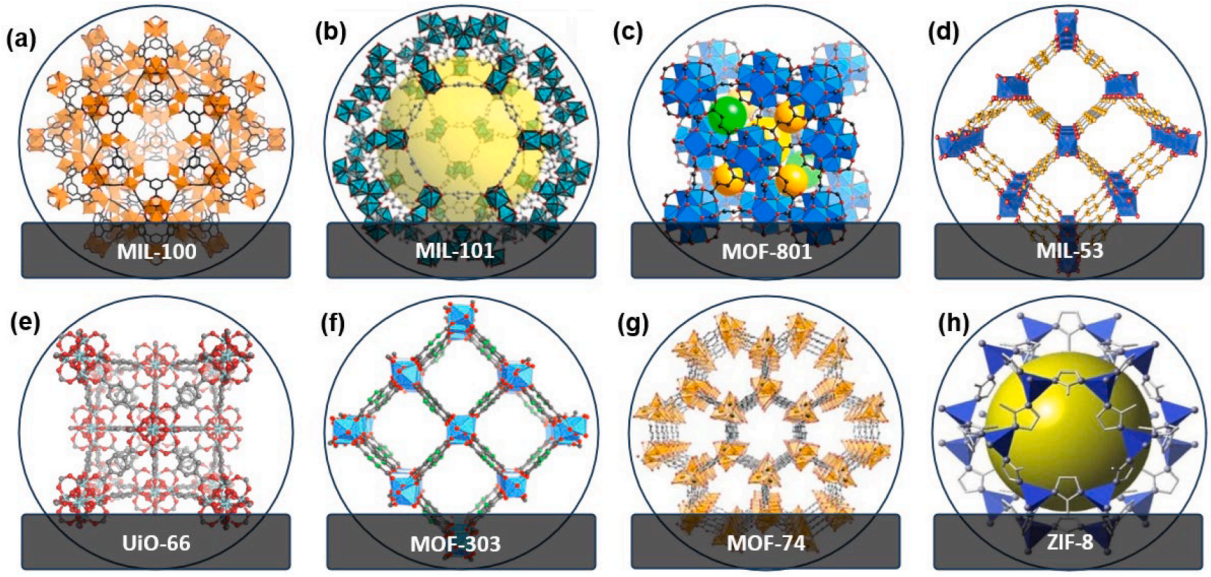

Fig. 11. Structures of selected MOFs commonly used for AWH. (a) MIL-100(Fe) with mesoporous cages accessible via pentagonal and hexagonal windows; Fe (orange octahedra), O (red), C (black), H omitted [254]. Copyright 2025 American Chemical Society (Open Access). (b) MIL-101(Cr) with mesoporous cages accessible through pentagonal and hexagonal windows; C (gray), O (red), Cr (blue), pores (yellow spheres) [255]. Copyright 2022 MDPI (Open Access). (c) MOF-801, a small Zr-MOF with fcu topology; C (black), O (red), Zr (blue polyhedra), pores (yellow/orange/green spheres) [256]. Copyright 2014 American Chemical Society. (d) MIL-53(Fe); C (yellow), O (red), Fe (blue) [257]. Copyright 2021 MDPI (Open Access). (e) UiO-66; Zr (cyan), O (red), C (grey), H omitted [258]. Copyright 2019 Nature. (f) MOF-303; C (grey), N (green), O (red), Al (blue polyhedra) [259]. Copyright 2018 Science. (g) MOF-74 [260]. Copyright 2023 Royal Society of Chemistry. (h) ZIF-8; Zn (polyhedra), N (spheres), C (lines) [261]. Copyright 2013 Elsevier.

temperature, or repeated cycling, it is noteworthy that no study in the SAWH literature has reported detectable leaching of linkers, metal ions, or other degradation-derived species into the condensed water harvested by MOF-based sorbents. This outcome is attributed to the vapor–liquid separation intrinsic to AWH, which limits the transfer of nonvolatile species into the collected condensate. Nonetheless, the potential for framework hydrolysis underscores the importance of incorporating standardized water-quality assessments in future SAWH studies to fully validate the long-term safety and reliability of MOF-based systems. Continued research has led to the design of frameworks with markedly improved water stability, opening new opportunities for their application. Among the early successful examples, MIL-101(Cr) emerged as a notable candidate for water adsorption [264]. In recent years, the number of water-stable MOFs has steadily increased, and several families have garnered particular attention for AWH applications. Fig. 11(a-h) illustrates representative structures, including MIL-100(Fe) [265], MIL-101(Cr) [266], MOF-801(Zr) [91], MIL-53(Cr or Fe) [267], UiO-66(Zr) [268], MOF-303(Al) [269], MOF-74(Zn) [270], and ZIF-8(Zn) [271]. Table 2 provides a comprehensive overview of some water-stable MOFs employed in AWH. Understanding the hydrolysis mechanism and identifying the factors that affect it is crucial for the design and synthesis of future MOF-based materials. It should be noted that for several MOFs listed in Table 2, the original literature does not provide detailed cycling test parameters (e.g., RH range or temperature), which limit comparability across datasets. Moreover, cycling performance in most studies is evaluated over a relatively small number of cycles, and long-term durability under extended operation remains insufficiently explored. This absence of long-duration testing presents a significant constraint for assessing the practical reliability of MOFs in SAWH applications.

4.1.1. Mechanisms of hydrolysis of MOFs

The reactions involving metal oxide clusters in MOFs when exposed to an aqueous environment encompass both ligand exchange and hydrolysis processes. During these reactions, water molecules are integrated into the metal coordination bonds through ligand displacement, as represented in the following equation:

$$Metal - Ligand + H_2O \rightarrow Metal - (OH_2) \cdots Ligand \quad (1)$$

In the hydrolysis process, the coordination bond between the metal and the ligand is cleaved, causing the water molecule to dissociate into protons (H^+) and hydroxide ions (OH^-). The hydroxide ions then attach to the metal center, while the protons interact with the displaced ligand, resulting in the reaction shown in the following equation [278]:

$$Metal - Ligand + H_2O \rightarrow Metal - (OH) + (Ligand - H) \quad (2)$$

Zr-based MOF is commonly used to study the degradation mechanism of MOFs in aqueous environments [279]. Its degradation process, shown in Fig. 12a, involves the breakdown of metal–ligand coordination bonds due to hydrolysis. When exposed to water, the metal oxide clusters in Zr-MOFs undergo hydrolytic attack, leading to the dissociation of the metal–ligand bond. Water molecules are introduced into the coordination sphere, displacing the original ligands. In the hydrolysis reaction, the coordination bond between the metal (Zr) and the ligand is broken and replaced by water molecules. For the practical application of MOFs in AWH, it is essential to enhance their hydrolytic stability. As depicted in Fig. 12b, addressing these stability issues is key to improving their long-term performance in environments with fluctuating humidity and water exposure [280]. Thus, ongoing research is focused on modifying the structural components of MOFs to enhance their resilience against hydrolysis, ensuring that they can function effectively in real-world AWH systems.

4.1.2. Factors affecting the water stability of MOFs

The water stability of MOFs is generally governed by two distinct aspects: thermodynamic and kinetic stability. The former concerns the Gibbs free energy change driving the degradation process, whereas the latter involves the energy barrier that must be overcome to initiate structural decomposition [281 282 84].

Table 2
Summary of some water-stable MOFs Employed in AWH.

MOF Types	Water Adsorption Capacity	RH (%)	Temperature (°C)	Cycles	Ref
MOF-801	0.26 g g^{-1}	20	25	–	[27]
MOF-303	0.48 g g^{-1}	15	–	150	[269]
MOF-74(Ni)	0.48 g g^{-1}	50	25	–	[272]
MOF-74(Mg)	0.68 g g^{-1}	50	25	–	[273]
UiO-66-NH_2	0.38 g g^{-1}	90	25	–	[274]
MIL-53	0.09 g g^{-1}	90	25	–	[274]
MIL-101-NH_2	0.90 g g^{-1}	90	25	–	[274]
co-MOF-31	0.78 g g^{-1}	30	25	20	[275]
MIL-100(Fe)	0.72 g g^{-1}	45	25	40	[276]
MIL-100(Al)	0.45 g g^{-1}	45	25	40	[276]
MOF-LA2-1	0.68 g g^{-1}	26	25	75	[277]
MOF-841	0.42 g g^{-1}	30	25	–	[27]
UiO-66	0.37 g g^{-1}	40	25	–	[27]
PIZOF-2	0.63 g g^{-1}	80	25	–	[27]

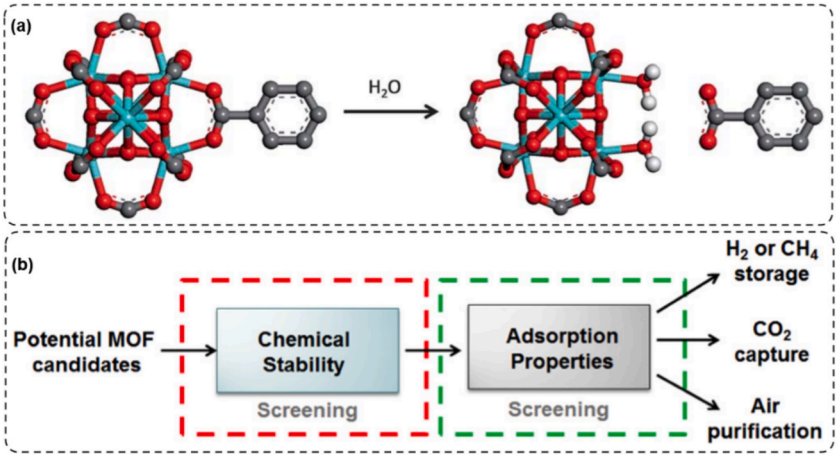

Fig. 12. Suggested mechanism illustrating the structural degradation of Zr-MOFs when exposed to water. Atoms of C (gray), H (white), O (red), and Zr (light blue) are highlighted, with H atoms omitted for simplicity [268]. Copyright 2013 Royal Society of Chemistry. (b) Significance of water stability in practical MOF applications [269]. Copyright 2014 American Chemical Society.

4.1.2.1. Kinetic stability. Kinetic factors play a dominant role in the hydrolytic stability of MOFs. A MOF can remain stable in an aqueous environment if it is kinetically stable, even if it is thermodynamically unstable. From a kinetic perspective, both hydrophobicity and spatial shielding play crucial roles in enhancing the water stability of MOFs.

To improve the water stability of MOFs, increasing the hydrophobicity of the framework is crucial. Researchers have explored post-synthetic modification techniques such as pore impregnation and surface modification to prevent water molecules from binding to metal centers [283]. For pore impregnation, hydrophobic molecules are introduced into porosity, where they can react with the active sites of the MOFs [284]. Nguyen and Cohen incorporated hydrophobic alkyl chains and exposed various synthesized MOFs, such as IRMOF-1 and NH_2-BDC, IRMOF-3, to ambient air or immersed them in water [285]. Their study demonstrated that hydrophobic groups effectively enhanced the hydrolytic stability of MOFs. Also, Ding et al. modified MOF-5 by reducing the size of its micro-holes from about 1.2 nm to ultra-micro-holes (0.7 nm), which improved the water stability of PN@MOF-5 [286]. However, these methods have strict requirements for the reaction centers on the backbone and the insertion components, limiting the range of MOFs and molecules that can be used for modification. Furthermore, they may reduce the original porosity and alter the physical and chemical properties, potentially decreasing water adsorption capacity [284].

An alternative approach is the external coating method. Zhang et al. successfully coated MOFs such as MOF-5, HKUST-1, and ZnBT with polydimethylsiloxane (PDMS), preserving their original crystalline properties and pore structures while significantly improving hydrolytic stability [287]. Building on this, Ding and Jiang introduced a one-step surface polymerization strategy [288]. Using HKUST-1 as an example, they applied free radical co-polymerization of trifluoroethyl methacrylate and 3-methacryloxypropyltrimethoxysilane to form a hydrophobic polymeric layer on the MOF's surface, producing HKUST-1-P. This hydrophobic polymer coating improved both the catalytic conversion and cycling stability of organic reactions in water, surpassing the water-sensitive properties of the original HKUST-1. Similar coatings were also applied to ZIF-67 and MIL-125, resulting in enhanced stability. It is important to note, however, that coating strategies must ensure that the polymer remains located on the external surface and does not penetrate into the porosity, since elongated polymer chains may weakly adsorb within the porosity through cumulative interactions. Such unintended infiltration can reduce accessible surface area and compromise the MOF adsorption properties.

Another approach to enhancing the water stability of MOFs involves factors that reduce the dynamic reactivity of water molecules with metal centers [280]. A key factor is spatial shielding, which creates an activation energy barrier, making it harder for water molecules to interact with the metal. Researchers have identified three strategies to improve spatial shielding [7]: (1) Increasing the connectivity of SBUs. High connectivity between metals strengthens the MOF structure, even when large amounts of water are adsorbed. For example, in UiO-66, each SBU is coordinated with 12 organic linkers, making it harder for water molecules to reach the metal centers, enhancing its water stability. By contrast, in Cu-BTC and Mg-MOF-74, the coordination numbers of metal atoms are lower, leaving the metal centers more exposed and susceptible to water absorption, even at low humidity levels [289]. The high number of coordinated metals in UiO-66 leads to an overcrowding effect that prevents water clusters from forming near the metal centers. (2) Using larger linkers. Larger linkers protect the metal centers from water. For instance, when Li et al. modified the pore channels of MOFs with various aliphatic groups, they found that longer aliphatic chains improved water stability [290]. Bio-MOF-14, modified with longer chains, maintained its crystallinity and porosity even after a month in water. Hungerford et al. also demonstrated that substituting certain ligands in Zn-DMOF improved its water stability, with the ADC-functionalized Zn-DMOF showing the highest stability [291]. (3) Introducing interpenetration. Interpenetration, where multiple MOF frameworks occupy the same space, also contributes to stability. This improvement arises not only from reduced porosity, which limits water access, but also from strengthened intra-framework interactions. Duan et al. synthesized Zr-IAM-4, which retained its crystallinity after boiling water treatment, demonstrating ultra-high hydrolytic stability due to its interpenetrating structure [292]. Similarly, Lei et al. developed double

interpenetrating MOFs like SNNU-324 and SNNU-325, which exhibited exceptional water stability [293]. However, this interpenetration generally reduces pore volume and adsorption capacity, limiting performance in adsorption-based applications.

In addition to these factors, the rigidity of the MOF's framework plays a significant role in its stability. Liu and Telfer discovered that MUF-77-ethyl, despite being a quaternary MOF, showed remarkable stability to water vapor, unlike other quaternary MOFs like MUF-7a [294]. This difference was attributed to the more rigid backbone of MUF-77-ethyl, which hindered hydrolysis. Similarly, Lv et al. found that Zr-MOFs with more rigid ligands exhibited better stability than those with flexible ligands [295]. The rigidity of the framework, including the geometry and topology of the pores, contributes to stability by reducing the likelihood of structural collapse under water exposure.

4.1.2.2. Thermodynamic stability. Even kinetically unstable MOFs can maintain stability in water due to thermodynamic factors. The thermodynamic stability of MOFs in an aqueous environment can be assessed by comparing the change in free energy during the hydrolysis process. Specifically, it involves calculating the difference between the free energy of the MOF after forming coordination complexes with water molecules and the free energy of the MOF with water molecules before the hydrolysis reaction takes place [280]. This calculation, however, is quite complex and challenging to perform.

The key structural feature of thermodynamically stable MOFs is the presence of inert metal clusters. In MOFs, the metal coordination centers act as electrophiles, while the oxygen in water is nucleophilic. If the metal coordination center is not inert enough to prevent interaction, water molecules will bind to the metal, triggering the hydrolysis of the MOF. In certain cases, the strength of the metal–ligand bonds can be a reliable indicator of a MOF's hydrolytic stability. According to the Hard and Soft Acid-Base (HSAB) theory, “soft” acids react faster with “soft” bases, forming stronger bonds, while “hard” acids react more readily with “hard” bases, also forming stronger bonds. Generally, “soft-soft” and “hard-hard” interactions are more stable [296 297]. In MOFs, the organic linker and the binding group in the metal center of the SBU act as a Lewis acid-base pair. Water, acting as an electron donor, can attack the metal–ligand bond, replacing the ligand and causing hydrolysis. When the metal–ligand bond is weak, the MOF structure is more prone to decomposition. Therefore, the hardness of both the ligand and metal ions is crucial for determining water stability. Colombo et al. were the first to apply the HSAB theory in the synthesis of MOFs, using this framework to create a series of pyrazolate-based MOFs [298]. Pyrazolate groups have higher pKa values than carboxylates, and as a result, they offer excellent thermal and chemical stability. Building on this, Xue et al. synthesized new heterogeneous metal MOFs by introducing a second metal into monometallic lead-based MOFs, proving their chemical stability through XRD and immersion tests in water at various pH levels [299]. The pKa value, which can be calculated using tools like the SPARC pKa calculator, is an important indicator of the thermodynamic stability of the designed MOFs [300]. Typically, linkers with high pKa values are considered hard bases, and stable MOFs are often created by combining hard base linkers, such as carboxylates, pyrazoles, or tetrazoles, with hard acid metal ions (e.g., Zr^{4+}, Cr^{3+}, Al^{3+}, Ti^{4+}) [301].

In addition to the metal–ligand bond strength, the reduction potential of metal ions plays a significant role in the thermodynamic stability of MOFs. MOFs with lower reduction potentials are more prone to hydrolytic degradation. Liu et al. tested aged and steamed Mg-MOF-74 and Ni-MOF-74. The results revealed that the crystal structure of Ni-MOF-74 broke down when treated with water vapor, resulting in a reduced surface area [302]. Conversely, Mg-MOF-74 maintained its crystal structure, but its specific surface area decreased significantly after water vapor treatment. Furthermore, Ni-MOF-74 showed a smaller reduction in surface area after long-term storage compared to Mg-MOF-74, indicating that Ni-MOF-74 is more stable. This is because Mg is a stronger reducing agent than Ni, making the Mg in Mg-MOF-74 more likely to react with water or oxygen in the air, which leads to structural damage. Kang et al. studied the effect of central metal ions on the stability of porous MOF materials by comparing the chemical and thermal stability of MOFs such as MIL-53(Al), MIL-53(Cr), and MIL-47-(V) [303]. Their findings showed that the stability of MOFs increased with the inertness of the central metal ion, regardless of the strength of the metal–ligand bonds. MIL-53-Cr displayed exceptional stability due to the significant energy difference between the water and chromium orbitals.

4.2. Thermal stability

Thermal stability represents a central requirement for MOFs employed in AWH, where the material undergoes continuous adsorption at ambient temperatures followed by desorption triggered by moderate heating. In practice, thermal stability in AWH encompasses two interconnected dimensions: the intrinsic structural stability of the framework under elevated temperatures, typically assessed through thermogravimetric analysis (TGA/DTG), and the operational durability of the MOF during repeated thermal cycling, which reflects real device conditions. Both aspects must be satisfied for long-term field deployment.

Intrinsic thermal robustness ensures that the MOF framework does not chemically decompose or undergo structural collapse during water desorption. TGA and DTG analyses are widely used to evaluate this property. For instance, the MOF-303@LiCl composite demonstrates strong thermal robustness with no signs of degradation under heating, confirming the stability of its composite structure [116]. Similarly, Al-fumarate-based MOFs exhibit high decomposition temperatures; however, structural modifications such as incorporating Fe into Al-fumarate can shift the decomposition peak from ~ 478 °C to ~ 433 °C, indicating that bimetallic bonding environments influence thermal stability signatures [304]. Other examples include MOF-808 and EDTA-modified MOF-808, both of which retain their phase purity and octahedral morphology up to ~ 250 °C, as confirmed by PXRD, SEM, and TGA analyses, demonstrating that chemical post-modification does not compromise thermal robustness [69]. Composite systems can also exhibit altered TGA behavior; for instance, embedding MIL-101(Cr) into PDMAPS hydrogels shifts the DTG peak from 191 °C to 208 °C, signaling stronger MOF–polymer interactions and improved water-binding behavior under heating [305].

While high decomposition temperatures ensure that the internal framework remains stable, thermal-cycling durability determines

whether a MOF can maintain adsorption capacity after dozens or hundreds of heating–cooling cycles within realistic AWH temperature ranges. This parameter is essential for practical systems that leverage daily solar-driven regeneration. Several studies highlight the importance of this behavior. For example, both PCGF-MMOF and Mix-MOF(5) preserved nearly 100 % of their performance after 100 adsorption–desorption cycles conducted between 25 °C (adsorption) and 60 °C (desorption) at 30 % RH, demonstrating strong operational stability without structural fatigue [306]. Monolithic Al-fumarate structures also show excellent thermal durability, retaining their water adsorption capacity under repeated cycling while offering advantages for industrial AWH manufacturing due to their mechanical strength and high hydrothermal resistance [304]. Thermal cycling stability is also influenced by heat-transfer pathways within the adsorbent module. For example, in situ growth of Al-based MOFs on aluminum foils not only simplifies fabrication but also enhances thermal transport due to the high thermal conductivity of the metallic substrate, thereby mitigating thermal stress and improving regeneration efficiency [307]. Such MOF-on-metal configurations have been reported for CAU-10(Al), MIL-96/MIL-100(Al), and HKUST-1 films, underscoring their promise for scalable AWH devices. Kinetic inertness and linker rigidity also play critical roles. MIL-101(Cr), with its robust metal clusters, retains both structural integrity and water adsorption performance under repeated solar-driven heating cycles, even when integrated with photothermal components such as Ni_3S_2. The composite maintains its morphology, elemental distribution, and crystallinity before and after cycling, confirming that thermally induced degradation is negligible under realistic operational temperatures [308].

4.3. UV stability

In outdoor SAWH systems, sorbent materials are continuously exposed to sunlight, including ultraviolet (UV) radiation, which can induce photochemical degradation of MOFs over long-term operation. UV photons may interact with organic linkers, causing bond cleavage, defect formation, or partial amorphization, ultimately reducing water uptake capacity. Although direct studies on UV stability of AWH-specific MOFs are still limited, evidence from related MOF-based systems clearly demonstrates the protective and degradative mechanisms relevant to UV-exposed environments. For example, studies have shown that encapsulating active molecules within MOF pore structures can significantly reduce UV-induced decomposition by physically blocking or absorbing incoming radiation. In one report, confining chlorantraniliprole inside MIL-101(Fe)-based carriers markedly suppressed photodegradation, with the MOF framework acting as a UV-shielding matrix that prolonged the functional lifetime of the encapsulated compound [309]. Similarly, systems based on metal-phenolic networks surrounding MIL-101 were shown to protect incorporated fungicides from UV-driven breakdown, as the Fe^{3+}-tannic acid coordination complexes effectively absorbed or scattered UV radiation before it reached the encapsulated cargo [310]. These studies, though not focused on water harvesting, highlight a broader principle that MOF structures or MOF-derived coatings can play a strong protective role against UV radiation by limiting direct photon interaction with sensitive chemical bonds.

This insight directly informs strategies for improving UV stability in SAWH sorbents. Given that UV-induced damage is cumulative and may progress slowly over time, evaluating UV stability for SAWH applications requires long-term outdoor aging experiments or well-controlled UV-exposure setups. Periodic structural and chemical characterization (e.g., XRD, FTIR, UV–vis spectroscopy, and adsorption isotherms) is essential to detect early signs of linker degradation or changes in sorption capacity. Considering that many SAWH devices are intended for regions with intense solar exposure, rigorous assessment of UV stability is critical to ensuring the long-term reliability and durability of MOF-based adsorbents in real operational settings.

5. Supporting Factors: Auxiliary conditions for enhanced SAWH performance

Beyond the primary adsorbent prerequisites, such as water adsorption capacity, photothermal efficiency, and structural stability, the practical performance of SAWH systems is strongly shaped by several auxiliary factors that govern how MOFs operate under real-world conditions. These factors include both MOF shaping and structuring for improved mass and heat transfer, and the management of chemical and airborne contaminants that may affect water quality. Addressing these complementary aspects is essential for translating high-performance MOFs into efficient, durable, and safe water-harvesting technologies.

5.1. Shaping methodologies for MOFs

The practical deployment of MOFs in SAWH devices requires materials that not only exhibit excellent intrinsic adsorption–desorption properties but can also be fabricated into mechanically robust, thermally conductive, and mass-transfer-efficient architectures. Since most MOFs are synthesized as fine powders, shaping is essential to enhance their handling, reduce pressure drop, and enable efficient heat and mass transfer. Broadly, shaping approaches fall into two categories: binder-free strategies, which better preserve the native porosity and surface area but often suffer from limited mechanical strength, and binder-assisted methods, which significantly improve robustness and processability at the cost of potential pore blocking or reduced accessible surface area. This section reviews these two major shaping methodologies, outlining how each approach influences the structural integrity, performance, and practical usability of MOFs.

5.1.1. Mofs shaping without binders

Binder-free shaping techniques aim to retain the intrinsic textural properties of MOF powders, such as surface area and pore volume, while transforming them into macroscopic forms suitable for handling and device integration. Although the mechanical strength of the resulting structures is generally lower than binder-assisted counterparts, these methods remain attractive because they

avoid pore blockage and chemical interference arising from external additives. A range of morphologies can be produced through such techniques, including films, coatings, gels, aerogels, monolithic blocks, pellets obtained via mechanical compression, and composite structures prepared by direct growth on porous supports.

In film and coating fabrication, MOFs are integrated onto or within substrates to improve transport properties and enable selective separations. Composite polymer-MOF membranes have been widely explored for gas separation applications, though interfacial leakage remains a challenge [311]. Strategies such as integrating ZIF-90 with cellulose nanofibers have demonstrated highly selective CO_2/CH_4 separation by forming dense, defect-free layers [311]. Multilayered MOF-on-MOF architecture has also been produced, enabling multifunctional film designs [312]. Coating MOFs onto monolithic supports such as cordierite improves macroscopic stability and handling, though reductions in accessible surface area and adsorption capacity relative to powders are commonly observed [313]. Nevertheless, optimized seeding and coating methods have achieved higher loadings and improved hydrothermal stability, enabling applications in heat exchangers and gas adsorption processes [314].

Binder-free shaping also includes sol–gel routes that yield MOF gels, xerogels, and aerogels with tunable porosity and often larger surface areas than their powdered precursors. Examples include ZIF-8 gels formed under high-concentration conditions [315], mechanically robust HKUST-1 monoliths synthesized through mild sol–gel drying [316], and UiO-66 xerogels/aerogels exhibiting significantly enhanced pore volume [317]. Aerogel forms of MIL-100(Fe) similarly maintain permanent porosity with high BET surface areas, although their mechanical properties remain a limiting factor [318]. Freeze-casting provides another binder-free pathway for producing directionally porous monoliths, such as HKUST-1 blocks with controllable macropore size; however, their poor water stability restricts broader applicability [319]. Alternatively, MOFs can be grown onto elastic porous substrates (such as sponges) to create mechanically robust and recyclable 3D composites with notable solvent uptake capacities and structural resilience [320].

Mechanical compression of MOF powders offers a straightforward means of producing granules and tablets without binders, and the resulting density can be tuned by adjusting the applied pressure [321]. Depending on the rigidity of the framework, compression may partially collapse the pore structure, as observed for MOF-177, which exhibits reduced microporosity after densification despite improved volumetric storage performance [322]. Similar effects have been reported for HKUST-1, where compressed pellets show substantial loss in adsorption capacity. In contrast, more structurally resilient MOFs such as CPO-27-Ni and ZIF-8 retain much of their porosity even under high pressures and demonstrate stable adsorption performance during cycling [323]. For flexible frameworks like MIL-53(Al), however, compression leads to significant reductions in surface area and pore volume [323].

5.1.2. Mofs shaping with binders

Shaping MOFs with binders provides a practical route to form mechanically stable pellets, granules, and monoliths, though it inevitably introduces trade-offs between robustness and retention of porosity. Inorganic binders offer good thermal stability. While clay-based binders require calcination and are incompatible with MOFs [324], non-calcination options such as ρ-alumina and silica sol have been successfully applied. Using 5 wt% ρ-alumina, several MOFs (MIL-100, MIL-101, UiO-66) were shaped into millimeter-sized pellets that maintained reasonable adsorption performance despite reduced BET area [325], though their crushing strengths (2.5–6.7 N) remained below packed-bed requirements [325]. With 10 wt% silica sol, MIL-100(Fe) granules retained ~ 90 % surface area and outperformed zeolite 13X in SF_6 breakthrough tests [326]. In contrast, pressing UiO-66 with 1 wt% graphite led to a 22 % reduction in surface area [327]. Overall, inorganic binders provide structural reinforcement but require careful tuning to limit porosity loss.

Organic binders offer strong adhesion and tunable mechanical strength but frequently cause pore blockage [328]. Chitosan@UiO-66 and sucrose-bonded UiO-66 pellets showed major decreases in surface area and H_2 uptake [329], though they exhibited excellent drop and abrasion resistance. Resorcinol-formaldehyde binders similarly reduced BET area and pore volume [330], especially in the microporous range. Binder compatibility is critical for flexible MOFs: MIL-53(Al) cracked upon heating when binder-free [331], while poly(vinyl alcohol) (PVA) improved strength but caused 32–81 % pore-volume loss depending on activation temperature. Methyl cellulose, however, preserved breathing behavior and maintained CO_2 and CH_4 uptake close to powder levels, with only modest pore-volume reductions [332].

Freeze-assisted shaping enables lightweight, highly porous monoliths using small amounts of binder. UiO-66/PVA structures with densities as low as 12 mg cm^{-3} were achieved with only 1 wt% binder [333]. Ice-templated UiO-66–chitosan monoliths retained near-original adsorption toward MCPP but lost surface area due to macropore formation [334]. The freeze-casting method was used to produce monoliths of aluminum fumarate (Alfum), MIL-160(Al), and MIL-101(Cr) using six polymer binders, such as poly(acrylic acid) (PAA), sodium polyacrylate (PAANa), polyethylene glycol (PEG), polyethylenimine (PEI), PVA with two hydrolysis degrees, and polyvinylpyrrolidone (PVP). These MOF@polymer monoliths, developed for water adsorption applications and adsorption-based cooling, showed reduced surface area and pore volume upon polymer addition, with PVA(98) and PVP causing the least reduction and PEI the most [335].

Phase-separation shaping forms monoliths through polymer–solvent mixing [336]. MIL-101(Cr) monoliths prepared with PVA exhibited improved mechanical strength but ~ 20 % lower BET area and water uptake [337]. More advanced variants of this method have produced low-density foams (<0.1 g cm^{-3}) containing up to 80 wt% MOFs with hierarchical porosity [338], suitable for membrane-reactor concepts.

Beyond granulation, extrusion, and the other shaping methods mentioned earlier, 3D printing has emerged as a highly promising technique that is gaining widespread attention. 3D printing offers precise control over geometry and is compatible with various binder systems [339]. Direct ink writing has been used to shape MOF-74(Ni) and UTSA-16(Co) monoliths using bentonite and PVA, delivering stable structures with compressive strengths of 0.48 and 0.56 MPa and acceptable adsorption performance [340]. Printed acrylonitrile butadiene styrene (ABS) and MOF (HKUST-1 and ZIF-8) composites retained theoretical surface area despite low MOF content [341]. COF monoliths have also been printed with < 8 % performance loss [342], indicating the method's broad potential.

5.2. Management of contaminants

One significant challenge in SAWH systems is the presence of VOCs and semi-volatile organic compounds (SVOCs) in water sources such as seawater, lake water, and atmosphere, which can contaminate the collected water [343 344 345 346 347 348]. These water sources often contain harmful VOCs and SVOCs, including benzene, toluene, phenol, formaldehyde, acetaldehyde, methylglyoxal, and benzaldehyde, which can evaporate, condense, or accumulate in the harvested water during SAWH processes [349]. Current methods for separating and removing VOCs and SVOCs rely on energy-intensive technologies like distillation and high-pressure-driven reverse osmosis (RO) [350 351]. This underscores the urgent need for advanced techniques capable of efficiently separating high-concentration VOCs and SVOCs from water.

Zeng et al. conducted a year-long study on a portable zeolite-based sorption-based AWH system deployed in residential and office buildings in the arid southwestern United States [349]. As illustrated in Fig. 13a, room air is drawn through an air filter, condenser unit, and rotating desiccant wheel by a fan. Approximately three-quarters of the wheel area is used for water vapor adsorption, while the remaining quarter undergoes regeneration via an electric heater. The released water vapor is cooled by incoming air across a condenser, resulting in liquid water collection. Continuous rotation enables uninterrupted operation. The system maintained a constant power consumption of 0.46 kWh throughout the study, consistent with manufacturer specifications and verified by power monitoring. The energy efficiency (L kWh^{-1}) was calculated based on water yield and operation time, with local temperature and RH recorded using environmental sensors. The device demonstrated reliable performance, achieving a median daily water yield of 3.6 L at a production cost approximately 30 % lower than commercial bottled water (Fig. 13b). However, beyond operational efficiency, the study highlighted a significant concern regarding the quality of the harvested water, particularly the elevated levels of VOCs and

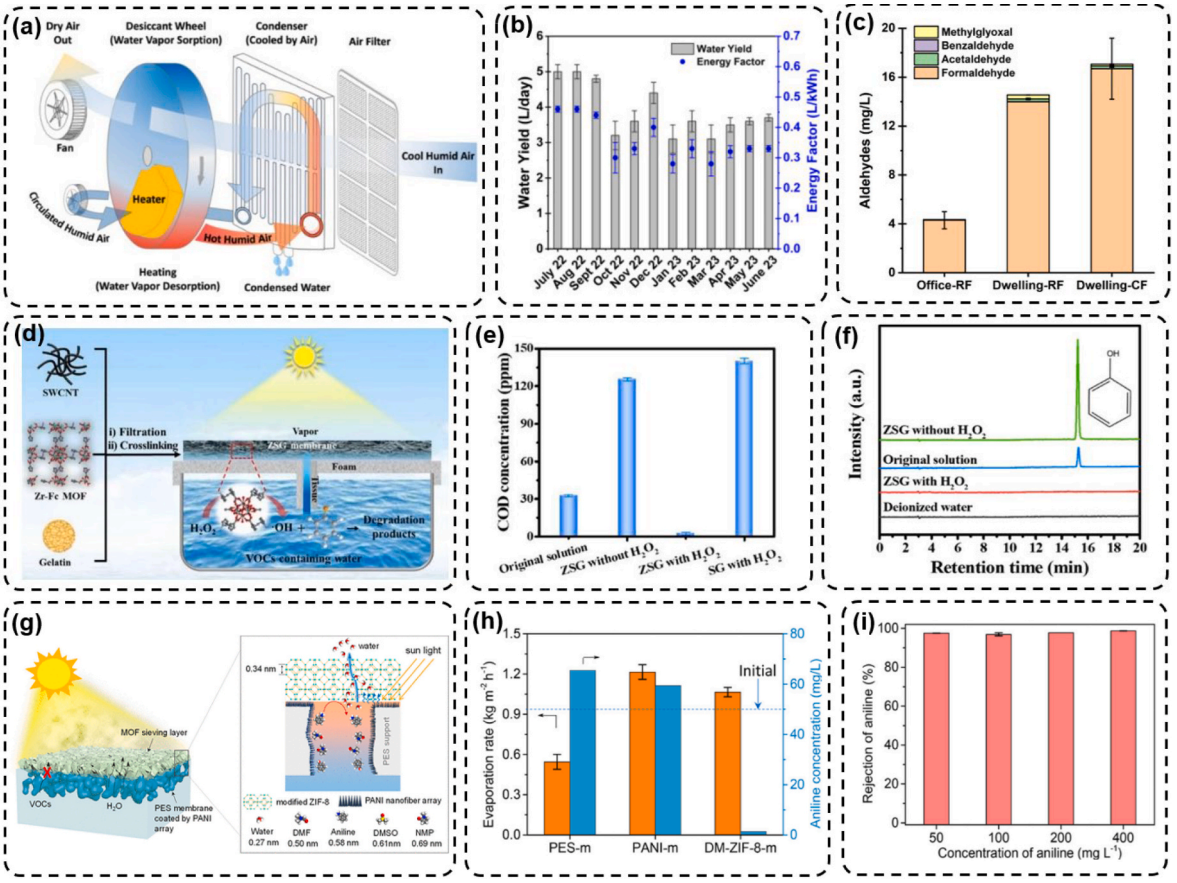

Fig. 13. (a) Schematic representation of a SAWH device [300]. (b) Results of a year-long SAWH study in a residential setting [300]. (c) Distribution of aldehyde compounds in water samples obtained from SAWH systems operated in both office and residential environments [300]. Copyright 2024 Elsevier. (d) Schematic showing the fabrication process of the ZSG membrane and the configuration of solar evaporation devices [303]. (e) COD levels of VOC-contaminated seawater before treatment and in the regenerated water collected post-evaporation [303]. (f) HPLC chromatograms of various samples analyzed using a mobile phase composed of ethanol and 0.1 % formic acid [303]. Copyright 2020 Royal Society of Chemistry. (g) Schematic of a PANI/ZIF-8 composite photothermal membrane designed for VOC removal from water via molecular sieving [304]. (h) Water evaporation rates and residual aniline concentrations in the distillate following treatment with PES-m, PANI-m, and DM-ZIF-8-m membranes under 1 sun irradiation (initial aniline concentration: 50 mg L^{-1}) [304]. (i) Aniline rejection efficiency of the DM-ZIF-8-m membrane at different feed concentrations (50, 100, 200, and 400 mg L^{-1}) [304]. Copyright 2022 American Chemical Society.

SVOCs, including formaldehyde, acetaldehyde, methylglyoxal, and benzaldehyde. These compounds originate from common indoor sources such as furniture, building materials, household products, and cooking emissions. Notably, formaldehyde concentrations reached up to 14 mg L^{-1} in residential samples, and total pollution levels were found to be nearly ten times higher than those measured in outdoor sorption-based AWH systems (Fig. 13c). Furthermore, the study established a strong correlation between pollution levels and both temperature and water conductivity, suggesting that temperature-dependent VOC emissions and ionic organic species significantly influence water chemistry. The acidic nature of the harvested water and its low buffering capacity were also linked to the presence of organic acids derived from VOCs. Despite the use of a carbon fiber air filter as a pre-treatment step, the system was not effective in removing these low molecular weight polar organics.This finding emphasizes the necessity for improved treatment strategies to manage VOC- and SVOC-derived contaminants.

Two promising approachs are to degrade VOCs in the contaminated water before evaporation and molecular sieving. The potential of MOFs in both areas has been demonstrated through research on Direct Solar Steam Generation (DSSG) systems, highlighting a promising future for the development of SAWH systems. Ma et al. fabricated a free-standing MOF-based membrane (ZSG) by mixing the Zr-Fc MOF (Z), SWCNT (S), and Gelatin (G) and used in a DSSG system (Fig. 13d) [352]. On one side, the membrane's hierarchical porosity, strong light-to-heat conversion efficiency, and favorable hydrophilicity collectively enabled a notable water evaporation rate of 1.53 kg m^{-2} h^{-1}, corresponding to a solar-vapor conversion efficiency of 95.6 % under standard solar illumination (1 sun). On the other side, the incorporation of ferrocene units into the ligand framework imparts the Zr-Fc MOF with significant Fenton-like catalytic activity, effectively decomposing VOCs and preventing their accumulation in the harvested water. They utilized the system illustrated in Fig. 13d with a Zr–Fc MOF/SWCNT/gelatin (ZSG) membrane, to regenerate water from VOCs-contaminated water. Phenol, a toxic VOC, was chosen as the model compound for the experiment. After condensation, the collected water's chemical oxygen demand (COD) and ion concentrations were analyzed. COD serves as an indicator of organic content in the water. As seen in Fig. 13e, the COD value in the water collected using the ZSG membrane, without the addition of H_2O_2, was about four times higher than its original value, indicating significant phenol accumulation. However, when H_2O_2 was introduced, the COD value in the collected water was substantially reduced. This trend was also observed in the High-Performance Liquid Chromatography (HPLC) data (Fig. 13f). Notably, the COD value of the collected water (2.3 mg L^{-1}) was below the drinking water hygiene standards set by China (GB5749-2006, 3 mg L^{-1}), suggesting that the ZSG membrane is capable of effectively producing drinking water from VOCs-contaminated sources. VOC removal from the contaminated water is also studied by the MOF-based DSSG system with other approaches. Peng et al. developed a composite photothermal membrane composed of a zeolitic imidazolate framework-8 (ZIF-8) and polyaniline (PANI) nanofiber array, aimed at removing high concentrations of VOCs from water through a size-selective filtration process integrated with solar-driven steam generation [63]. Since water molecules possess a smaller kinetic diameter than most VOCs, tailoring the membrane's effective pore size to fall between these two allows selective passage of water while blocking VOCs (Fig. 13g). In their design, a modified form of ZIF-8 (ZIF-8-m) with an aperture size of approximately 0.34 nm served as the molecular sieving layer, while the underlying PANI nanofibers functioned as the photothermal component, converting sunlight into heat to drive water evaporation. To improve resistance to hydrothermal degradation, the ZIF-8-m layer was further functionalized via ligand exchange using a hydrophobic molecule, 5,6-dimethylbenzimidazole (DM), resulting in the DM-ZIF-8-m structure. This composite membrane demonstrated both strong photothermal performance and excellent VOC rejection capabilities. Under simulated sunlight (1 sun), it achieved a water evaporation rate near 1.0 kg $m^{-2}h^{-1}$ while maintaining a VOC removal efficiency of up to 99 % for feedwaters containing VOC concentrations as high as 400 mg L^{-1} (Fig. 13h,i). Additionally, the system showed durable separation performance under prolonged operation and increased solar intensity.

Beyond VOCs and SVOCs, recent studies have shown that SAWH systems may also introduce other secondary contaminants into the collected water, including dissolved inorganic species, trace metal ions, potential microbial impurities, and airborne contaminants. Several experimental investigations on AWH devices demonstrate that most major ions, such as Na^+, K^+, Ca^{2+}, and Mg^{2+}, remain well below WHO drinking-water thresholds, even when hygroscopic salts or mixed-ion hydrogels are used as sorbents. For example, Zhang et al. employed a hygroscopic hydrogel-LiCl system and reported that all measured cations (including Li^+) were significantly lower than WHO limits based on ICP-MS analysis of the harvested water [353]. Similarly, Entezari et al. evaluated water produced by a Li/Ca-alginate-FCNT sorbent at 70–80 °C and found Ca^{2+} concentrations in the range of 2.9–12.3 ppm, with Li^+ and Cl^- also remaining within WHO-defined safe limits [354]. Lyu et al. further demonstrated that water obtained from the SAWH system contained Na^+, K^+, Ca^{2+}, and Mg^{2+}, Pb^{2+}, and Al^{3+} at concentrations below WHO standards, confirming that heavy metal release from sorbent frameworks is minimal under typical operating conditions [355]. In active Atmospheric Water Generator (AWG) systems, which share similar condensation pathways with SAWH devices, metal-ion release and organic contamination have also been systematically assessed. A large-scale survey of 83 AWG water samples collected in heavily industrialized regions revealed that nearly all measured ions and trace metals were below Environmental Protection Agency (EPA), and European Union (EU) regulatory limits; only sporadic detections of Ni (up to 0.61 mg L^{-1} in a minority of samples) and dichloromethane were reported, while most toxic metals remained undetectable [356]. Importantly, microbial analysis of AWG-produced water confirmed the absence of coliforms and pathogenic species such as E. coli and P. aeruginosa, indicating that constrained air-surface contact times and enclosed storage significantly reduce biological contamination risks [357].

In real-world SAWH deployments, sorbent materials are exposed to various airborne pollutants such as sulfur dioxide (SO_2), and nitrogen oxides (NO_x). These contaminants can interact with the MOF surface, alter coordination environments, or compete with water for adsorption sites. Such processes can compromise sorption kinetics, reduce total water uptake, or necessitate additional purification steps after condensation. Recent studies have shown that certain water-harvesting MOFs, such as MOF-303, exhibit significant affinity toward specific airborne contaminants, particularly SO_2. Computational analyses using GCMC and DFT have demonstrated that SO_2 can hydrogen-bond to the MOF-303 framework with higher binding energies than water, enabling pollutant molecules to occupy

adsorption sites at low pressures. This behavior highlights how airborne gases can interfere with water uptake depending on concentration and environmental conditions. In contrast, the same studies reveal negligible uptake of NO and NO_2, suggesting that the degree of vulnerability to air pollutants varies strongly with MOF chemistry and pollutant identity. Importantly, mixture adsorption simulations indicate that at higher water vapor pressures, H_2O molecules outcompete SO_2, displacing it from the framework (a dynamic that prevents irreversible site poisoning but may still reduce performance under certain pollutant loads) [358].

These findings collectively highlight that, in addition to VOC transfer, potential leaching of metal ions from MOF structures (especially under acidic or highly humid cycling), accumulation of airborne contaminants, inorganic residues, and microbial growth in storage vessels must also be considered when evaluating the potability of SAWH-collected water. Future SAWH designs should therefore integrate both material-level stability (hydrolytic robustness, minimal ion release) and device-level hygienic strategies (closed collection pathways, anti-biofouling management) to ensure long-term production of safe drinking water.

6. Progress in MOF-based SAWH studies

Although several MOF-based AWH and SAWH systems and materials have been referenced in previous sections to elucidate key strategies and performance mechanisms, this section provides a dedicated and in-depth review of representative studies to systematically highlight the evolution of MOF enabled SAWH research. As illustrated schematically in Fig. 14, the proportion of MOF based SAWH publications has steadily increased each year, with a noticeable acceleration in 2025. The data were collected from the Web of Science database over the period 2017- June 2025. Table 3 provides a consolidated overview of representative MOF based SAWH systems, summarizing key aspects such as the sorption and photothermal agents, water uptake, and harvested amounts under specific RH, temperature (T), and solar intensity (I) conditions.

The first significant demonstration of a MOF-based SAWH system was reported by Kim et al. in 2017, who developed a passive system based on MOF-801 and Graphite, known for its steep water uptake isotherm at low relative humidity (as low as 20 % RH) [27]. In their design, MOF-801 was embedded in a copper foam substrate to improve thermal conductivity and structural integrity. MOF-801 exhibits a water uptake exceeding 0.25 g g^{-1} at vapor pressures above 0.6 kPa, corresponding to 20 % RH at 25 °C. Using 1 sun illustration (1 kW m^{-2}), the system achieved a water yield of up to 2.8 L kg^{-1} day^{-1}, without any external energy input or active cooling. Their work, supported by both experimental validation and numerical modeling, laid the foundation for future developments in passive solar water harvesting from arid air. Building upon this pioneering work, in 2018, the same group introduced an improved design by infiltrating MOF-801 powder into a porous copper foam and coating the opposing surface with pyromark paint as photothermal layers [359]. This adsorbent shows a water uptake of 0.25 g g^{-1} at 30 % RH at 15–25 °C. The integration of these materials enabled desorption temperatures up to 70 °C under natural sunlight and maintained a comparable water yield of ≈0.12 L kg^{-1}, confirming the viability of photothermal-enhanced passive SAWH. In parallel, Fathieh et al. developed an all-in-one SAWH system incorporating 33 wt% nonporous graphite into a MOF-801 layer (MOF-801/G) and evaluated its performance under real desert climate conditions [269]. At 30 % RH and 25 °C, MOF-801/G exhibits a water uptake of around 190 cm^3 g^{-1}. Their prototype, tested both in the laboratory and the Arizona desert, achieved a water production rate of ≈95 g kg^{-1} day^{-1} using only natural cooling and ambient

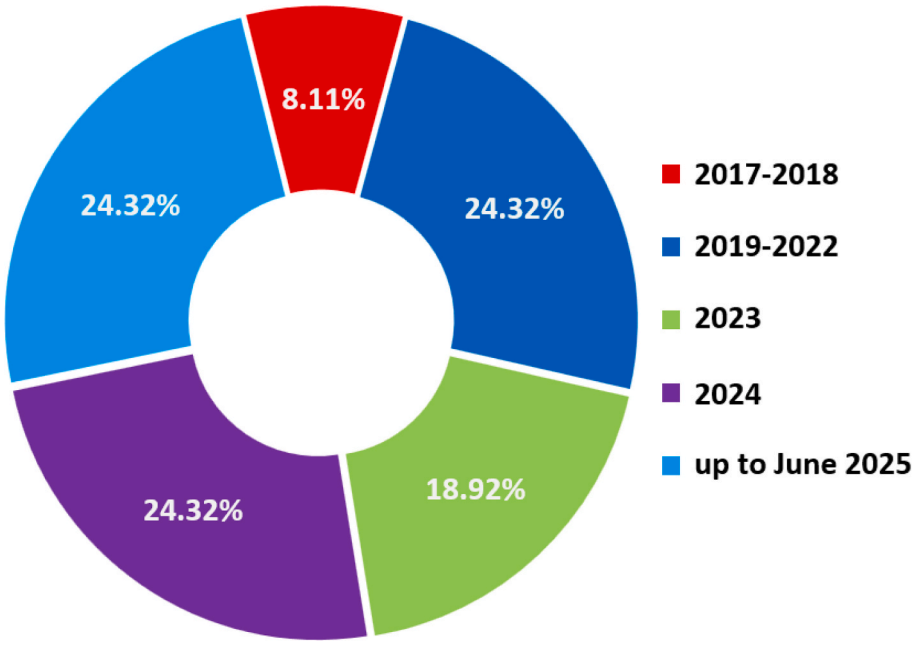

Fig. 14. Yearly distribution of MOF-based SAWH publications from 2017 to June 2025, based on data collected from the Web of Science database, illustrating the accelerating research momentum in the field.

Table 3
Overview of MOF-based SAWH systems.

SAWH Material	Sorption Agent	Photothermal Agent	Water Uptake (RH(%), T(°C))	Water Harvested (I(kWm^{-2}), RH(%), T(°C))	Ref
MOF-801-G	MOF-801	Graphite	0.25 gg^{-1} (20, 25)	≈2.8 Lkg^{-1}day^{-1} (1, 20, 25)	[27]
MOF-801-P	MOF-801	Pyromark	0.25 gg^{-1} (30, 15–25)	≈0.12 LKg^{-1}day^{-1} (1, 30, 25)	[359]
MOF-801/G	MOF-801	Graphite	190 cm^{3}g^{-1} (30, 25)	≈95 gkg^{-1} (1, 40, 15)	[269]
MOF-303/G	MOF-303	Graphite	350 cm^{3}g^{-1} (30, 25)	≈230 gkg^{-1} (1, 40, 15)	[269]
LiCl@MIL-101(Cr)-CB	LiCl@MIL-101(Cr)	CB	0.77 gg^{-1} (30, 30)	–	[360]
$CaCl_2$@Fe-Fc-HCPs	$CaCl_2$	Fe-Fc-HCPs	2.685 gg^{-1} (80, 25)	–	[118]
M−8010	MOF-801@MIL-101(Cr)	CNT	0.18 gg^{-1} (10, 25)	≈0.253 LKg^{-1}day^{-1} (1, 15, 25)	[123]
TUN/SA	UiO-66-NH_2	MXene Ti_3C_2	≈0.25 gg^{-1} (30, 25)	≈58 mLkg^{-1}h^{-1} (1, 20, 25)	[127]
CGF-mixed-MOFs(Al)	mixed-MOFs(Al)	mixed-MOFs(Al)	0.37 gg^{-1} (30, 25)	–	[124]
CACS	Al-Fum	MWCNT	≈0.32 gg^{-1} (35, 25)	≈1.4 Lkg^{-1}day^{-1} (1, 32, 23)	[361]
MOF-derived NC	MOF	NC	≈0.13 Lkg^{-1} (20, 25)	≈0.18 Lkg^{-1}h^{-1} (1, 30, 25)	[134]
HMC-2	MIL-101(Cr)	CNT	1.074 gg^{-1} (90, 25)	≈3.22 Lkg^{-1}day^{-1} (1, 90, 25)	[109]
HMF	MIL-101(Cr)	Fc(COOH)$_2$	1250 cm^{3}g^{-1} (50, 25)	≈1.72 kgm^{-2}day^{-1} (1, 80, 25)	[362]
PM NCM	MIL-101(Cr)	CNT	1.04 gg^{-1} (98, 25)	≈15.9 Lkg^{-1}day^{-1} (1, 50, 25)	[363]
PGF-BMOF	BMOF(3)	PGF	0.23 gg^{-1} (30, 25)	≈1.19 gg^{-1}day^{-1} (1, 30, 25)	[304]
$CaCl_2$@MOF-808	$CaCl_2$@MOF-808	Solar Panel	0.56 gg^{-1} (30, 25)	≈1.8 kgkg^{-1}day^{-1} (1, 30, 25)	[117]
PCC-42	Ca-MOF, $CaCl_2$	Carbon	≈0.6 gg^{-1} (30, 25)	1.13 Lkg^{-1}day^{-1} (1, 30–60, 25)	[119]
MOF-801/CNT	MOF-801	CNT	0.219 gg^{-1} (20, 25)	–	[200]
MOF-801/CB	MOF-801	CB	0.146 gg^{-1} (20, 25)	–	[200]
MOF-801/G	MOF-801	G	0.123 gg^{-1} (20, 25)	–	[200]
Al-Fu@Cu@CuxS	Al-Fum	Cu_xS	0.223 gg^{-1} (40, 25)	–	[364]
CS/PDA-Mix-MOF(5)	Mix-MOF(5)	CS/PDA	0.44 gg^{-1} (30, 25)	≈0.94 gg^{-1}day^{-1} (1, 40–70, 25)	[306]
LiCl@Al-Fum@MWCNT	LiCl@Al-Fum	MWCNT	0.9 gg^{-1} (40, 25)	–	[112]
FO@HK@CP	FO@HK	CP	≈0.25 gg^{-1} (30, 25)	2.62 Lkg^{-1}day^{-1} (1, 25, 25)	[365]
Ni-doped MOF-801	MOF-801	Ni	0.29 gg^{-1} (30, 25)	≈0.39 gg^{-1}h^{-1} (1, 30, 25)	[366]
PML hydrogel	MIL-101(Cr), LiCl	PDMAPS	0.614 gg^{-1} (40, 25)	<0.1 gg^{-1}h^{-1} (1, 40, 25)	[305]
AHN_Al_M	Al-MOF	Hydrogel	0.26 gg^{-1} (40, 25)	≈0.79 kgm^{-2}h^{-1} (1, 60, 40)	[367]
PMC	MOF-801-G	PPy	0.386 gg^{-1} (20, 25)	≈1.081 kgkg^{-1}day^{-1} (1, 61, 33)	[368]
SA-TA@MOF	MOF-801	Fe^{3+}-tannic acid	0.14 gg^{-1} (20, 25)	≈1.4 Lkg^{-1}day^{-1} (1, 20, 25)	[369]
Ni-Ni_3S_2 mesh/BMOF	MIL-101(Cr)	Ni-Ni_3S_2 mesh	0.635 gg^{-1} (60, 25)	≈0.0032 gg^{-1}min^{-1} (1, 60, 25)	[308]
Cu_xS-Cu/Al-MOF	Al-Fum	Cu_xS	0.161 gg^{-1} (30, 25)	≈1.081 Lkg^{-1}day^{-1} (1, 30, 15)	[307]
E-MOF-808@CuS	E-MOF-808	CuS	0.39 gg^{-1} (25, 25)	≈0.05 gg^{-1}h^{-1} (1, 35–45, 24–26)	[69]
TCMs	Monolithic MOF	Ti_3C_2/sHBP	0.31 gg^{-1} (35, 25)	≈1.84 Lkg^{-1}day^{-1} (1, 35, 25)	[370]
MOF-CT/PVA	Zn-TCPP, CT, PVA	Zn-TCPP	1.21 gg^{-1} (30, 25)	≈8.46 gg^{-1}h^{-1} (1, 90, 25)	[371]
PCL	LiMOF, LiCl	PC	1.21 gg^{-1} (20, 25)	≈0.15 Lkg^{-1}h^{-1} (1, 60, 25)	[372]
Cu_3(HHTP)$_2$	Cu_3(HHTP)$_2$	Cu_3(HHTP)$_2$	0.24 gg^{-1} (20, 25)	≈8.16 gm^{-2}h^{-1} (1, 20, 25)	[373]
VHN_AlM/$CaCl_2$	$CaCl_2$	NH_2-MIL-53(Al)	0.62 gg^{-1} (50, 25)	≈2.98 kgm^{-2}h^{-1} (1, 90, 25)	[374]
NPC_{MAF-47}	MOF-74	Carbon	405 mgg^{-1} (30, 25)	≈542 mgg^{-1}h^{-1} (1, 90, 25)	[375]
MOF-303@LiCl-CB	MOF-303@LiCl	CB	0.61 gg^{-1} (30, 25)	≈0.21 gg^{-1}h^{-1} (1, 30, 25)	[116]
WCBs@SA/MNPs/MOFs	MOF-801	MNP	0.24 gg^{-1} (20, 25)	≈1.41 Lkg^{-2}day^{-1} (1, 20, 25)	[376]

sunlight, without any external cooling or additional energy input. Replacing MOF-801 with MOF-303 (MOF-303/G) increases the water uptake significantly to around 350 cm^3 g^{-1} at 30 % RH and 25 °C. This substitution more than doubled the water yield (≈230 g kg^{-1} day^{-1}), demonstrating the significant potential of material choice in improving water harvesting efficiency. Furthermore, the adsorbent layer's surface temperature could rise to around 100 °C, enhancing thermal efficiency for water desorption. Their desert field trials provided valuable insights into airflow, energy balance, and material requirements for practical deployment in extreme arid zones, highlighting MOF-303′s potential in next-generation SAWH systems.

These early studies-spanning from 2017 to 2018-not only proved the concept of passive, solar-driven water harvesting using MOFs, but also paved the way for continued innovation in this area. Building on the initial breakthroughs, subsequent advancements up to 2023 have significantly expanded the landscape of MOF-based SAWH systems. One of the earliest and most effective strategies for improving water uptake under arid conditions involved the incorporation of hygroscopic salts into porous MOF frameworks, enabling synergistic sorption mechanisms at low RH. For instance, Xu et al. focused on integrating hygroscopic salts into porous frameworks and enhancing solar-driven water desorption through photothermal coatings [360]. In this work, a high-performance composite sorbent, LiCl@MIL-101(Cr)-CB, was developed specifically for efficient SAWH under arid conditions (Fig. 15a). LiCl was confined within the MIL-101(Cr) porosity, enabling synergistic water uptake through chemisorption, deliquescence, and solution absorption, achieving a water uptake of ≈0.77 g g^{-1} at 30 % RH and 30 °C. To facilitate solar-driven desorption, a CB coating was applied as an independent photothermal layer, which increased the composite temperature from 30 to 97 °C under one sun irradiation, enabling complete water release within 100 min without external energy input (Fig. 15b). Hu et al. developed $CaCl_2$@Fe-Fc-HCPs, a composite material combining hygroscopic $CaCl_2$ with photothermally active Fe-ferrocene MOF-based hollow microspheres (Fe-Fc-HCPs), designed to synergistically enhance water harvesting efficiency [118]. In this structure, $CaCl_2$ acts as the water sorbent, while the Fe-Fc-HCPs provide efficient solar-driven heat for rapid water release. The hollow microsphere architecture prevents $CaCl_2$ dissolution in absorbed water, improves water vapor access, and facilitates mass transport. As a result, at 80 % RH and 25 °C, the composite achieves a water uptake of ≈2.685 g g^{-1}, which corresponds to a 2.23 times greater value than that of pure $CaCl_2$. Thanks to the excellent

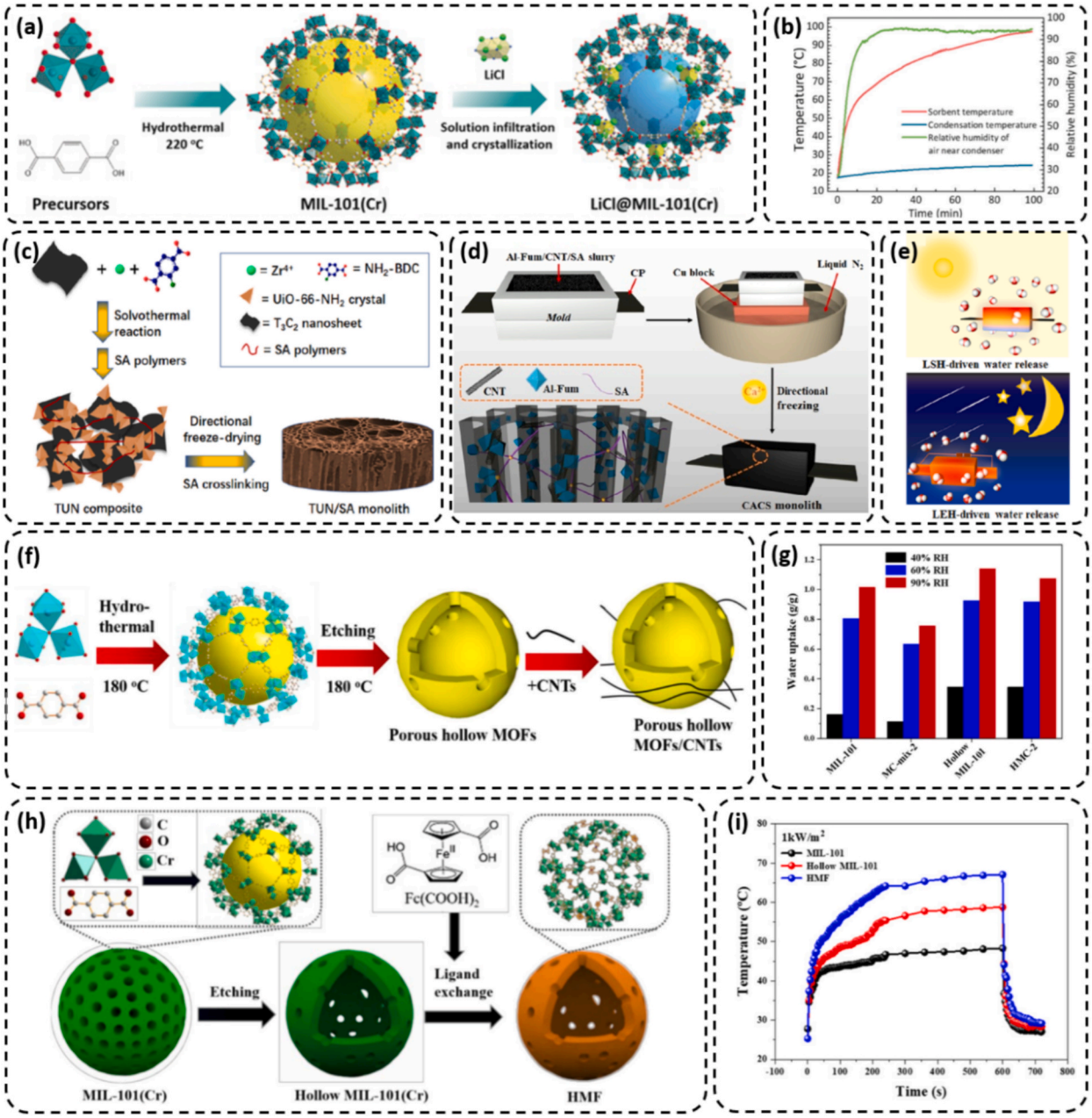

Fig. 15. (a) Schematic illustration of the fabrication process of LiCl@MIL-101(Cr) [307]. (b) Representative temperature profiles for composite sorbent temperature [307]. Copyright 2020 WILEY (Open Access). (c) A schematic representation of the fabrication process for TUN/SA monoliths [309]. Copyright 2021 American Chemical Society. (d) Schematic diagram illustrating the preparation steps of the CACS monolith [310]. (e) Water release from the CACS monolith under LSH and LEH conditions [310]. Copyright 2022 American Chemical Society. (f) Schematic illustration of the chemical structure design and fabrication process of porous hollow MIL-101/CNTs [311]. (g) Water adsorption of MIL-101, MC-mix-2, hollow MIL-101 and HMC-2 composites at 25 °C, 40 % RH, 60 % RH and 90 % RH, respectively [311]. Copyright 2022 Elsevier (Open Access). (h) Schematic Illustration of the Structure and Fabrication Process of Hollow MIL-101(Cr)/$Fc(COOH)_2$ Spheres [312]. (i) Temperature changes of MIL-101, hollow MIL-101, and HMF under simulated sunlight (1 kW m^{-2}, light turned off after 600 s) [312]. Copyright 2022 American Chemical Society.

photothermal performance of the Fe-Fc MOFs, complete water desorption is achieved under 1 sun irradiation, without any optical concentration. The material also exhibits good cyclic stability, with no performance loss over 5 adsorption–desorption cycles, demonstrating its durability for real-world SAWH applications. This work offers a cost-effective and scalable route to enhance traditional desiccant-based systems by integrating them with photothermal MOFs, paving the way for efficient and sustainable freshwater generation. In a related study, Hu et al. introduced a polyvinylpyrrolidone (PVP)-assisted self-assembly method to fabricate core–shell MOF-801@MIL-101(Cr) supraparticles (M−8010) for enhanced SAWH in arid environments [123]. To improve

photothermal performance, CNTs are incorporated into the structure, enabling faster water release under solar irradiation. The synergistic design, featuring a MOF-801 shell for water preconcentration and a MIL-101 core for high-capacity storage, significantly enhanced sorption performance, with water uptake at 8 % RH being 225 % and 390 % higher than that of pure MOF-801 and MIL-101, respectively. At 25 °C and 10 % RH, the material achieved a water uptake of 0.18 g g^{-1}. Additionally, a water collection rate of 0.253 L kg^{-1} day^{-1} was obtained under 10–20 % RH, confirming the material's potential as a stable and efficient sorbent for solar-driven water harvesting in extremely arid climates. To address scalability and structural limitations of powder-based sorbents, researchers began engineering monolithic, integrated systems with vertically aligned porous architectures that offer mechanical stability and enhanced mass/heat transfer. For instance, Wu et al. addressed the critical limitation of batch-mode operation [127]. They developed composite monoliths by incorporating MXene Ti_3C_2 into UiO-66-NH_2, forming vertically aligned porous structures known as TUN/SA (Fig. 15c). These monoliths demonstrated improved photothermal performance and accelerated water adsorption–desorption kinetics under low-humidity conditions. At 30 % RH and 25 °C, TUN/SA exhibits a water uptake of around 0.25 g g^{-1}. A key innovation in their work was the design of a SAWH system with a flippable dual-layer TUN monolith configuration, enabling continuous rather than cyclical water production. This system achieved a water harvesting rate of up to 58 mL $kg^{-1}h^{-1}$ under simulated sunlight (1 sun, 298 K, 20 % RH), marking a significant step toward scalable and cost-effective water production in arid climates. The enhanced performance was attributed to the synergistic effects of the MXene component and the optimized porous architecture, which collectively improved solar absorption and moisture transport within the material. In a parallel effort to develop scalable and mechanically robust water sorbents, Luo et al. developed a robust and efficient monolithic water sorbent by functionalizing glass fiber paper (CGF) with mixed-linker Al-MOFs, composed of MIL-160(Al) and Al-fumarate, via in situ self-assembly [124]. To enhance MOF loading (up to 306.7 %), a chitosan polyelectrolyte layer was first applied to the CGF substrate, leveraging electrostatic and hydrophilic interactions. The resulting CGF-mixed-MOFs(Al) monolith exhibited superior water adsorption performance and faster kinetics at low humidity levels due to the increased number of active sites. At 30, 25, and 20 % RH, the material achieved uptake capacities of 0.37, 0.31, and 0.25 g $g^{-}1$, respectively. A lab-scale SAWH device demonstrated the material's practicality in low-humidity environments, while 50-cycle tests confirmed its structural stability, crystallinity, and lack of MOF leakage. This work presents a scalable, cost-effective, and long-lasting strategy for atmospheric water harvesting in arid climates.

Recognizing the need for uninterrupted water production across varying environmental conditions, hybrid heating systems combining solar and electrical inputs were developed to maintain high performance during both day and night. For instance, Tao et al. developed an innovative sandwich-structured MOF monolith called CACS to improve the flexibility and efficiency of MOF-based SAWH systems (Fig. 15d) [361]. CACS features vertically aligned porous channels and dual localized heating methods: localized solar heating (LSH) and localized electrical heating (LEH) (Fig. 15e). It was fabricated by embedding carbon paper (CP) within a MOF monolith composed of Al-fumarate (Al-Fum), multiwalled CNTs (MWCNTs), and cross-linked SA polymer networks. This dual-mode heating strategy enabled the system to operate under varying environmental conditions, during both sunlight-rich periods and times with insufficient solar irradiation, such as at night or on cloudy days. Compared to LSH, LEH provided more rapid and uniform thermal distribution across the monolith, significantly improving the kinetics and efficiency of water desorption. CACS showed a water uptake of 0.31–0.34 g g^{-1} at 35 % RH and 25 °C, slightly lower than bare Al-Fum/SA (0.37 g g^{-1}), mainly due to the low adsorption capacity of the CNT component (0.02 g g^{-1}). Utilizing the CACS monolith as the sorbent material, a multifunctional SAWH prototype was constructed, capable of operating in three distinct modes: LSH-only, LEH-only, and a hybrid LSH/LEH mode. In the hybrid mode, the device achieved a water productivity of 1.4 L kg^{-1} day^{-1} (32 % RH, 23 °C), representing a 5.4-fold increase over LSH-alone performance (0.26 L kg^{-1} day^{-1}), while requiring 17.9 % less energy than the LEH-only mode, albeit with a 22.2 % reduction in water yield. This study represents a significant advance in the field of SAWH, demonstrating a versatile and energy-conscious design that allows for all-day water production with tunable operation modes based on climatic conditions, desired water output, and energy availability.

Another key innovation in MOF-based SAWH focused on accelerating the kinetics of water capture and release, aiming to enable multiple rapid sorption–desorption cycles per day for improved water yield. For example, Song et al. developed a copper halide MOF ($CuCl_2$(4,4′-bipyridine))-derived NC adsorbent via pyrolysis and steam-selective etching, featuring abundant nitrogen-containing sites that impart excellent hydrophilicity and rapid water capture capability [134]. This sorbent can capture up to 90 % of its equilibrium water loading (0.18 L kg^{-1}) within just 40 min (30 % RH). Moreover, it demonstrates outstanding water release performance, desorbing more than 99 % of the absorbed water in only 10 min under one-sun illumination. This work offers a promising design strategy to develop high-yield, SAWH systems with fast cycling for advanced freshwater generation, especially suitable for arid environments. Recent studies have turned to molecular engineering approaches, such as ligand exchange and nanostructure decoration, to precisely tailor the photothermal efficiency, water sorption kinetics, and multifunctionality of MOF-based materials. Hu et al. synthesized a hollow MIL-101(Cr)-CNTs structure via acid etching, which enhances visible light absorption by extending the light path through multiple reflections [109]. Decorating these hollow MIL-101(Cr) particles with CNTs, resulting in the composite HMC-2 (Fig. 15f), further improved water adsorption capacity and kinetics. The hierarchical porous hollow structure offers abundant defect sites and reduces mass transfer resistance, facilitating efficient water molecule adsorption and diffusion. HMC-2 achieved a maximum water uptake of 1.074 g g^{-1} at 25 °C and 90 % RH (Fig. 15g). Impressively, at low humidity, its water adsorption capacity increased by 113 and 203 % compared to pure MIL-101(Cr) and CNT-decorated MIL-101(Cr), respectively. The synergistic effect of CNTs and hollow MIL-101(Cr) enhanced solar-thermal heat generation, enabling fast desorption kinetics with complete water release within 90 min under one-sun illumination. A full adsorption–desorption cycle completes in 210 min, allowing up to three cycles daily, which translates to a potential water yield of 3.22 L kg^{-1} in high-humidity environments. These superior water uptake and release rates position HMC-2 as a highly promising material for efficient AWH, especially under solar-driven conditions. In another study, Hu et al. developed multifunctional hollow MIL-101(Cr) nanospheres via post synthetic ligand exchange using ferrocene dicarboxylic acid (Fc$(COOH)_2$), resulting in the HMF composite (Fig. 15h) [362]. Under 1 kW m^{-2} solar irradiation for 10 min, HMF achieved a

significantly higher temperature (67.1 °C) compared to MIL-101 (48.3 °C) and hollow MIL-101 (58.8 °C) (Fig. 15i), demonstrating an improved photothermal conversion efficiency of approximately 61.6 %. These enhancements are attributed to the unique electronic band structure and coordination of the Fc ligand. At 50 % RH and 25 °C, HMF exhibits a water uptake of around 1250 $cm^3\ g^{-1}$. Water adsorption and desorption by HMF nanospheres proceeded 2.3 and 4.5 times more rapidly, respectively, than in unmodified MIL-101 (Cr). In outdoor testing, HMF achieved a water harvesting capacity of 1720 $g\ m^{-2}$ per cycle (at an 8 mm bed thickness), demonstrating excellent performance under natural sunlight. Additionally, the material exhibited antibacterial activity of 91.4 %, suggesting it not only enhances water collection efficiency but also contributes to safe water harvesting. This study introduces a molecular-level design strategy via ligand exchange to create MOFs with tailored photothermal and functional properties for high-efficiency SAWH applications.

Since 2023, increased attention has been directed toward advancing MOF-based AWH systems, leading to a growing body of research aimed at enhancing performance, adaptability, and scalability under real-world conditions. Li et al. developed a MIL-101(Cr)/nanofibrous/CNTs composite membrane (PM NCM) via a simple spray electrospinning method aimed at efficient individual or household-scale water harvesting [363]. Under controlled conditions of 25 ± 0.5 °C and 98 % RH, the PM NCM sample exhibited an effective moisture uptake of 1.04 $g\ g^{-1}$, comparable to that of MIL-101(Cr), confirming its strong water adsorption performance. The composite features a 3D porous nanofibrous network, which enables fast water vapor transport, while the incorporation of CNTs imparts high solar absorption (92.8 %) and photothermal conversion, reaching surface temperatures above 70 °C under one-sun illumination. This design effectively addresses the limitation of conventional MIL-101(Cr) powder, which suffers from slow adsorption/desorption cycles due to crystal aggregation. The monodispersed MIL-101(Cr) within the porous nanofibrous matrix not only increases active sites but also drastically shortens the adsorption–desorption cycle to 50 min (40 min adsorption + 10 min desorption). This rapid cycling enables multiple daily operation cycles and achieves a high-water production rate of 15.9 $L\ kg^{-1}\ day^{-1}$ (RH 50 %, 25 °C). In addition to its superior performance, the membrane exhibits desirable practical features such as flexibility, portability, and long-term stability, making it a promising candidate for scalable and practical SAWH applications. Luo et al. proposed an effective strategy to develop a cost-efficient, energy-saving, and high-performance sorbent for SAWH by synthesizing a bimetallic MOF (BMOF) via a one-step solvothermal method [304]. The resulting BMOF(3), composed of Al-fumarate and MIL-88A, exhibited a significantly enhanced surface area (1200 m^2g^{-1}) and pore volume (0.51 cm^3g^{-1}), attributed to the synergistic topological modulation by Al and Fe atoms. These structural optimizations resulted in superior water uptake performance across a wide range of humidity conditions. To translate these advantages into a practical system, the authors engineered a solar-responsive monolithic adsorbent by integrating the BMOF(3) framework with polyaniline (PANI)/chitosan coatings on a glass fiber (GF) substrate (PGF), yielding the PGF-BMOF module. This composite not only mitigated the limitations of powder-form MOFs, such as handling difficulties and low structural stability, but also enabled rapid sorption–desorption cycles due to enhanced photothermal response and efficient directional water transport. Notably, even under low humidity (30 % RH), the adsorbent achieved a water uptake of 0.23 $g\ g^{-1}$. A proof-of-concept solar-powered device incorporating the PGF-BMOF demonstrated robust field performance, achieving six full adsorption–desorption cycles per day and collecting up to 113.3 g of potable water. The system also exhibited a daily water yield of 1.19 $g\ g^{-1}$, highlighting its potential for scalable, off-grid water harvesting applications. By leveraging biosafe character and low-cost ligands such as fumaric acid and designing a structurally integrated adsorbent module, this study offers a promising and practical route toward next-generation AWH technologies. An et al. developed a salt-modified MOF composite ($CaCl_2$@MOF-808) to address the limitations of conventional adsorbents and pristine MOFs in low-humidity SAWH [117]. By incorporating hygroscopic $CaCl_2$ into the MOF-808 framework, the composite achieved a high-water uptake of 0.56 $g\ g^{-1}$ at 30 % RH (seven times greater than bare MOF-808) while also demonstrating enhanced structural stability and cycling durability. Outdoor testing with a custom-built solar-powered device showed a water yield of 1.8 $kg\ kg^{-1}\ day^{-1}$. The combination of low cost, high hydrophilicity, and practical recyclability positions $CaCl_2$@MOF-808 as a promising candidate for scalable, solar-driven water harvesting in arid environments. Hu et al. proposed a novel approach to enhance the water harvesting performance of MOF-based materials by developing a porous $CaCl_2$-decorated sorbent (PCC-42) via carbonization of Ca-MOF followed by HCl vapor treatment [119]. The resulting PCC-42 exhibited an exceptional water uptake of 3.04 $g\ g^{-1}$ at 100 % RH and demonstrated fast adsorption–desorption kinetics along with strong photothermal properties. Even under low humidity conditions (30 % RH), it maintained high adsorption capacities (around 0.6 $g\ g^{-1}$), significantly outperforming both Ca-MOF and $CaCl_2{\cdot}2H_2O$. Notably, ~80 % of the adsorbed water could be released under 1 sun in 50 min, and outdoor SAWH tests showed a water yield of 1.13 $L\ kg^{-1}\ day^{-1}$ under arid conditions (30–60 % RH, 20–30 °C). This study presents a practical strategy for designing high-efficiency, solar-responsive sorbents suitable for atmospheric water harvesting in low-humidity environments. Wu et al. investigated a SAWH strategy using composite materials with enhanced photothermal performance [200]. While MOF-801 is widely recognized for its high-water uptake and broad humidity-range applicability, its strong affinity for water also requires relatively high thermal input for desorption, limiting its practical efficiency in low-energy environments. To address this limitation, the authors explored the integration of photothermal carbon materials into MOF-801, synthesizing three composite adsorbents using graphite (G), CNTs, and CB material [200]. Among them, the MOF-801/CNT composite demonstrated superior performance. Structural characterization revealed that MOF-801/CNT exhibited a BET surface area of 355 $m^2\ g^{-1}$ and an average pore size of 4.26 nm-features conducive to both high sorption capacity and effective water transport. Functionally, the incorporation of CNTs significantly improved the photothermal conversion efficiency, resulting in a 30 % increase in water adsorption capacity and a 50 % enhancement in desorption rate compared to the MOF-801/G composite under identical conditions. The MOF-801/CNT composite achieves high water uptake (≈0.15 $kg\ kg^{-1}$ at 20 % RH, 25 °C), making it a promising sorbent for low-humidity SAWH. The study also highlighted that low-temperature, high-humidity environments favor water uptake for MOF-801/CNT, underscoring its suitability for deployment in arid climates with diurnal humidity fluctuations. This work demonstrates the potential of carbon-enhanced MOF composites to overcome energy barriers in SAWH systems, thereby advancing the design of more efficient, solar-powered water harvesting technologies for off-grid and

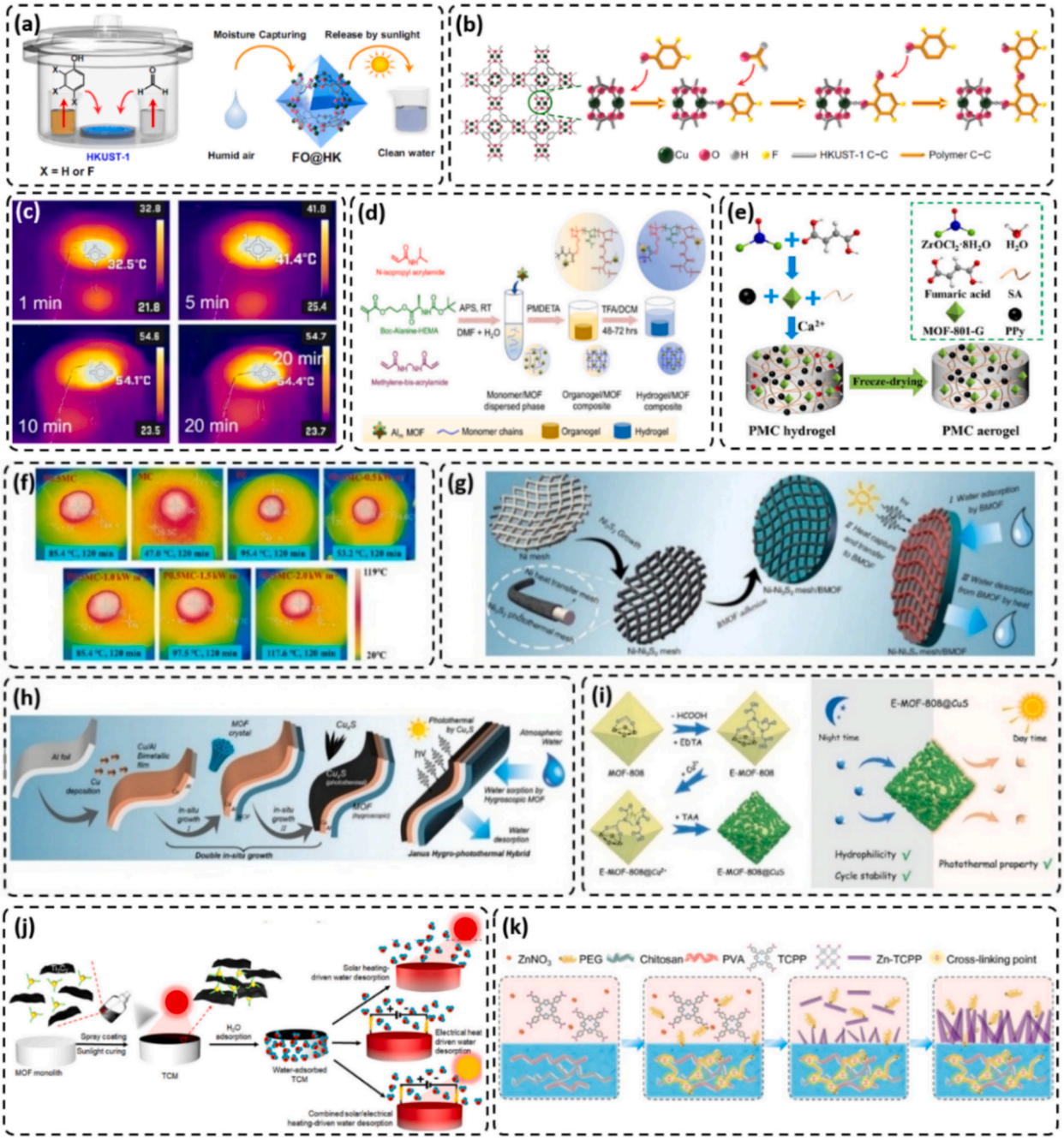

Fig. 16. (a) FO@HK synthesis via VPP inside HKUST-1 pores [319]. (b) VPP occurring at open Cu sites acting as Lewis acid catalysts [319]. (c) IR images of F_3@HK_30@CP under 1 sun [319]. Copyright 2024 Nature (Open Access). (d) Formation of hydrogel/MOF composite by mixing pre-synthesized MOF with hydrogel [322]. Copyright 2024 American Chemical Society. (e) Synthesis of PMC aerogel combining MOF-801-G, polypyrrole, and calcium alginate [323]. (f) IR images of MC, PC, and P0.5MC under 1 sun, and under different light intensities [323]. Copyright 2024 Royal Society of Chemistry. (g) Schematic illustration of Ni-Ni_3S_2 mesh/BMOF synthesis [325]. Copyright 2024 WILEY (Open Access). (h) Formation of Cu_xS–Cu/Al–MOF Janus structure integrating sorptive and photothermal layers [326]. Copyright 2024 WILEY (Open Access). (i) Post-modification of MOF-808 and solar-driven water release from E-MOF-808@CuS [327]. Copyright 2024 WILEY (Open Access). (j) Water desorption in TCM driven by Ti_3C_2/sHBP solar, electrical, and hybrid heating [328]. Copyright 2024 American Chemical Society. (k) Dual role of PEG in MOF-CT/PVA synthesis as hydrogel crosslinker and MOF surfactant [329]. Copyright 2024 Nature (Open Access).

resource-limited regions. To overcome the persistent limitations in mass and heat transfer efficiency of MOF-based SAWH systems, Tan et al. engineered a solar-responsive, sandwich-like adsorbent, designated as Al-Fu@Cu@Cu_xS [364]. This multifunctional composite was constructed via in-situ growth on a thin copper substrate, layering Cu_xS (top), Cu (middle), and Al-fumarate MOF (Al-Fum) (bottom). Each component serves a targeted function: Al-Fum as a hygroscopic matrix for water vapor adsorption, Cu_xS as a highly efficient photothermal layer, and Cu as a heat-conductive interface to facilitate rapid thermal transfer throughout the structure. The composite exhibited a high specific surface area (1033.19 $m^2\ g^{-1}$), enabling a saturated water uptake of 0.223 $g\ g^{-1}$. Under 1 sun (xenon lamp) irradiation, Al-Fu@Cu@Cu_xS reached a surface temperature of 70.4 °C, which was significantly higher than the 42.9 °C observed for pure Al-Fu. It achieved 93.3 % water desorption within 50 min, demonstrating superior performance compared to pure MOF materials. The warming process occurred in two distinct stages: an initial plateau likely caused by heat absorption during water desorption from the MOF layer, followed by a further temperature rise after desorption was nearly complete. The highest temperature, recorded at 87.6 °C, was located at the central copper layer within the structure. The photothermal conversion efficiency of the composite was calculated to be 95.2 %, reflecting a 203.3 % improvement over Al-Fu alone. After the light source was turned off, both Al-Fu@Cu@Cu_xS and the MOF layers rapidly cooled down to room temperature. Moreover, the material demonstrated stable performance even under low RH (40 %), achieving a water uptake of 0.204 $g\ g^{-1}$ and maintaining a sorption equilibrium of 91.5 %. When integrated into an operational SAWH device, the composite enabled a water collection capacity of 2.14 g per cycle, over three times greater than powdered Al-Fu (0.69 g per cycle). The hybrid design successfully overcame conventional thermal limitations and demonstrated excellent cyclic stability, providing a promising pathway for high-efficiency, SAWH in diverse climatic conditions. Luo et al. fabricated a highly integrated monolithic adsorbent module for SAWH, eliminating the need for separate adsorption and photothermal components [306]. Their design combines a layer-by-layer assembly of hydrophilic chitosan/polydopamine (CS/PDA) coatings with composite MIL-160(Al)/MOF-303 (termed Mix-MOF(5))-deposited on a lightweight glass-fiber substrate. Through competitive crystallization, Mix-MOF(5) achieves an optimal structural reorganization, yielding a high specific surface area (917.6 $m^2\ g^{-1}$) and pore volume (0.44 $cm^3\ g^{-1}$), facilitating superior moisture uptake across all humidity conditions: 0.44 $g\ g^{-1}$ at 30 % RH, 0.46 $g\ g^{-1}$ at 60 % RH, and 0.56 $g\ g^{-1}$ at 90 % RH, outperforming the parent MOFs. The CS/PDA photothermal layer efficiently absorbs solar energy and enables rapid water desorption without additional heat sources. The modular prototype achieves a smooth four-cycle daily operation, delivering an outdoor water yield of approximately 0.94 $g\ g^{-1}\ day^{-1}$ under standard sunlight-indicating both high productivity and low energy demand. By unifying high adsorption capacity, fast adsorption–desorption kinetics, solar-powered regeneration, and scalable architecture in a single lightweight structure, this study offers a versatile and practical SAWH solution, particularly well-suited for deployment in arid and off-grid regions.

The year 2024 witnessed an accelerated momentum in MOF-based SAWH research compared to previous years. This acceleration was driven by the growing urgency to combat global freshwater scarcity, alongside advances in materials science, device engineering, and system level integration. During this period, research expanded beyond fundamental water uptake and began to address photothermal performance, moisture stability, desorption kinetics, and scalability, which led to the development of composite architectures that significantly outperformed earlier designs.

Wang et al. introduced a novel atmospheric water harvesting system centered around a multifunctional gel-based adsorbent and a custom-designed device for continuous operation [112]. Their system integrates a double-network porous hydrogel doped with LiCl-modified Al-Fum (LiCl@Al-Fum) to enhance hygroscopic performance under low humidity conditions. To enable passive, solar-driven desorption, carboxylated MWCNTs were incorporated to boost the photothermal properties. Notably, the gel's internal structure was engineered to facilitate vapor transport, and the device design allowed for uninterrupted day-night water harvesting cycles. The system demonstrated a water uptake of 0.9 $g\ g^{-1}$ at 40 % RH and underscored the potential of combining advanced sorbent engineering with device optimization for scalable, off-grid water generation.

Following this, Kang et al. introduced an innovative fluorinated composite MOF sorbent (FO@HK) to overcome key challenges in SAWH, particularly in low-humidity environments [365]. The study focused on HKUST-1, a well-known MOF with high water affinity but limited hydrolytic stability and enhanced its performance by incorporating fluorophenyl oligomers (FO) via a vapor-phase polymerization (VPP) approach (Fig. 16a,b). This modification not only preserved the intrinsic water sorption properties of HKUST-1 but significantly improved its moisture stability and enabled rapid water release under mild solar irradiation. The resulting composite, FO@HK, demonstrated outstanding water uptake of around 0.25 $g\ g^{-1}$ at 30 % RH, respectively, demonstrating superior performance compared to numerous contemporary studies. Moreover, a scaled-up field experiment using F3@HK-30 deposited on carbon paper (CP) further validated the material's efficacy. The SAWH device, operating under real arid conditions (25 % RH, 25 °C), achieved a daily water collection rate of 2.62 $L\ kg^{-1}$ with over 90 % water desorption efficiency within 20 min under 1 sun illumination. To track the temperature evolution of F3@HK_30@CP under 1 sun irradiation, time-lapse infrared imaging was performed using an IR camera. As illustrated in Fig. 16c, the surface temperature rose to approximately 54 °C within 10 min and then stabilized. Additionally, visible water droplets were observed through the view window after 20 min of solar-driven desorption, indicating that effective desorption can be achieved using low-grade solar heat. This study not only highlights the potential of fluorinated MOF composites for high-performance SAWH in low-humidity environments but also provides a scalable and energy-efficient pathway for sunlight-powered water recovery. However, the potential toxicity and persistence of fluorinated compounds may limit their large-scale or commercial application, emphasizing the need for careful evaluation of their long-term safety and sustainability.

Building on salt-bases systems, Yan et al. focused on low-humidity performance by engineering a Ni-doped variant of MOF-801 using mixed organic linkers [366]. By incorporating mixed organic linkers (2,3-diaminobutanedioic acid and fumaric acid) into the MOF-801 framework via a one-pot synthesis method, they successfully enhanced both the adsorption capacity and desorption kinetics of the material. The resulting N-doped MOF-801 demonstrated a rapid uptake of 0.29 $g\ g^{-1}$ at 30 % RH within 30 min and could release 90 % of the adsorbed water within 10 min under standard solar irradiation (1 sun). In practical terms, a custom-built SAWH device

loaded with this sorbent achieved up to 4.64 L kg^{-1} over a 12 h cycle at 30 % RH. These performance metrics underscore the effectiveness of nitrogen modification in tuning pore chemistry and hydrophilicity for enhanced SAWH. This work introduces a mixed-linker engineering strategy to simultaneously achieve fast kinetics, high capacity, and cycling stability, demonstrating a viable path toward scalable and efficient SAWH technologies for deployment in arid and off-grid regions. Yan et al. developed a polymer-MOF-salt composite hydrogel (PML hydrogel) to address key limitations of salt-based SAWH systems, such as salt leakage and aggregation due to the salting-out effect [305]. This composite incorporates a zwitterionic hydrogel (PDMAPS), a high-surface-area MOF (MIL-101(Cr)), and hygroscopic LiCl salt, leveraging the synergistic interaction between these components to enhance both sorption capacity and structural integrity. The PML hydrogel demonstrated excellent water uptake of 0.614 g g^{-1} at 40 % RH and 1.827 g g^{-1} at 90 % RH under ambient conditions (298 K) and reached 80 % of its saturation capacity within 117 min at 30 % RH and 149 min at 90 % RH. However, despite its outstanding adsorption performance and cycling durability over ten consecutive cycles, the desorption kinetics of the PML hydrogel under solar-driven conditions remain relatively slow. Under simulated arid desert conditions (RH = 0 %, T = 353 K), the hydrogel released 80 % of its adsorbed water within ~ 200 min, while the remaining 20 % required more than 13 h for complete desorption. This sluggish release is attributed to the deliquescence/crystallization behavior of LiCl, which occurs alongside chemical adsorption–desorption processes and significantly impedes water release. These findings suggest that while the PML hydrogel offers strong potential for SAWH, further optimization is needed to enhance its desorption efficiency under low-humidity, solar-powered conditions. Moreover, the reliance on LiCl raises concerns regarding the abundance and cost of lithium resources, which could represent an additional limitation for large-scale or commercial deployment. In another hydrogel-based system, Sahoo and Tripathi developed an amino acid-based hydrogel/MOF (AHN_Al_M) for SAWH, integrating an alanine-based zwitterionic hydrogel with Al-based MOFs to create a synergistic structure with enhanced water uptake and photothermal desalination capabilities (Fig. 16d) [367]. The optimal composition, labeled 0.5AHN_Al_M(7.5) (comprising 7.5 wt% Al-MOF), exhibited high sorption efficiency across a range of RHs, achieving 2.21 g g^{-1} at 90 % RH, 0.47 g g^{-1} at 60 % RH, and 0.26 g g^{-1} at 40 % RH. The composite leveraged the hydrophilic and porous nature of both the hydrogel and MOF to establish extended sorption–desorption channels, enabling rapid moisture capture and release. Additionally, under solar irradiation, the composite demonstrated an evaporation rate of 0.79 kg $m^{-2}h^{-1}$, successfully converting 3.4 g of saline water into freshwater in just 3.5 h, highlighting its potential not only for SAWH but also for solar-driven desalination.

Moving to aerogel systems, Liu et al. developed a multifunctional, solar-responsive aerogel composite (PMC) composed of polypyrrole (PPy), defect-rich MOF-801-G, and calcium alginate (CA) to address global water scarcity through SAWH (Fig. 16e) [368]. The composite integrates hygroscopic and photothermal functionalities: MOF-801-G contributes high surface area and water-sorption-active defect sites (notably Zr-OH groups), CA provides structural support and hydrophilicity, while PPy enhances photothermal conversion for efficient solar-driven desorption. Among the tested formulations, the P0.5MC aerogel (with 0.5 g MOF-801-G) exhibited excellent performance, achieving a water sorption capacity of 0.386 g g^{-1} at 20 % RH and 25 °C. Under simulated solar irradiation (1 sun), the composite rapidly reached surface temperatures of 85.4 °C (Fig. 16f), enabling > 95 % desorption efficiency within 2 h and solar water vapor conversion efficiencies above 90 %. Outdoor experiments under real-world conditions (32.85 °C, 61.01 % RH) yielded 1.081 $kgkg^{-1}day^{-1}$, with collected water meeting World Health Organization (WHO) drinking water standards. This study underscores the importance of defect engineering (e.g., Zr-OH content) in boosting sorption kinetics and capacity, and demonstrates the viability of MOF-based, solar-activated composite aerogels for scalable, efficient, and clean SAWH in diverse climates. Complementing this, Zhu et al. developed a vertically aligned nanocomposite sorbent (SA-TA@MOF-5 %) integrating MOF-801 with a polymeric matrix via Fe^{3+}-induced crosslinking and directional freezing, offering a scalable and highly efficient platform for SAWH [369]. The engineered hierarchical pore architecture not only improved the structural integrity and sorption kinetics of MOF-801 but also significantly enhanced photothermal performance through Fe^{3+}-tannic acid coordination, achieving ~ 89 % solar absorption. The material demonstrated rapid sorption–desorption cycles completed within 2 h (1 h for adsorption and 1 h for solar-driven desorption under 1 sun), with water uptake capacities of 0.14–0.57 g g^{-1} across a humidity range of 20–80 % RH. Daily water yields reached up to 1.40 L kg^{-1} at 20 % RH and 5.57 L kg^{-1} at 80 % RH, outperforming many state-of-the-art MOF-based SAWH systems. Moreover, the material-maintained performance over repeated cycles showed potential for additional applications such as dehumidification and air purification. This study demonstrates a practical pathway for overcoming the scalability limitations of MOF powders, presenting a high-performance monolithic adsorbent for efficient solar-driven water harvesting in arid environments.

Addressing a key limitation in SAWH, the sluggish desorption kinetics of MOFs, Chen et al. introduced a photothermal bridge strategy [308]. Specifically, they fabricated a Ni-Ni_3S_2 mesh/MIL-101(Cr) composite sorbent by bonding bulk MOF (BMOF) onto a thermally conductive and photothermally active Ni-Ni_3S_2-coated nickel mesh (Fig. 16g). This configuration effectively enhanced heat transfer and desorption rate under solar irradiation. The composite achieved a water uptake of 0.635 g g^{-1} at 60 % RH and 25 °C, reaching saturation within 150 min. Despite a 28.6 % reduction in water uptake compared to pristine MOF, the composite demonstrated complete desorption within just 40 min under 1 sun (1 kW m^{-2})-a feat unattainable with MOFs alone. Even under weaker solar input (0.6–0.8 kW m^{-2}), it maintained desorption times below 100 min. Heat-transfer simulations revealed uniform temperature distribution across the mesh/MOF interface, validating the efficacy of the photothermal bridge in rapid energy delivery. Notably, the system demonstrated superior sorption–desorption kinetics at 3.18 × 10^{-3} g g^{-1} min^{-1}, surpassing other morphologies (foil, granule, foam) and maintained structural and functional integrity over 50 cycles. These results confirm that integrating photothermal materials with MOFs via mesh architecture not only accelerates solar desorption but also ensures mechanical robustness and long-term stability, making it a practical SAWH solution for humid, water-scarce environments.

Building upon this, Chen et al. in a subsequent study further tackled the fundamental limitation of MOF-based SAWH systems-their inefficient water desorption-by proposing a novel Janus-structured hygro-photothermal adsorbent [307]. This advanced design integrates hydrophilic aluminum fumarate MOF (Al-Fum) on one face and a photothermal Cu_xS layer on the opposite face of a Cu/Al

bimetallic substrate, resulting in the Cu_xS-Cu/Al-MOF Janus composite (Fig. 16h). Each face functions independently: the MOF side adsorb moisture while the Cu_xS side facilitates rapid solar-driven heating. The Janus configuration enables directional heat transfer through the metal substrate acting as a thermal bridge, significantly enhancing desorption efficiency. The composite demonstrated a water uptake of 0.161 g g^{-1} at 40 % RH, achieving saturation within 39–52 min. Impressively, under 1 sun (1 kW m^{-2}), the system reached 71.5 °C in just 20 min and released 97 % of the absorbed water within 40 min, with a photothermal conversion efficiency of 90.6 %. Notably, after 200 adsorption–desorption cycles, the composite retained stable performance in terms of sorption capacity and thermal response. Under simulated arid conditions, the Cu_xS-Cu/Al-MOF exhibits efficient adsorption–desorption kinetics, enabling

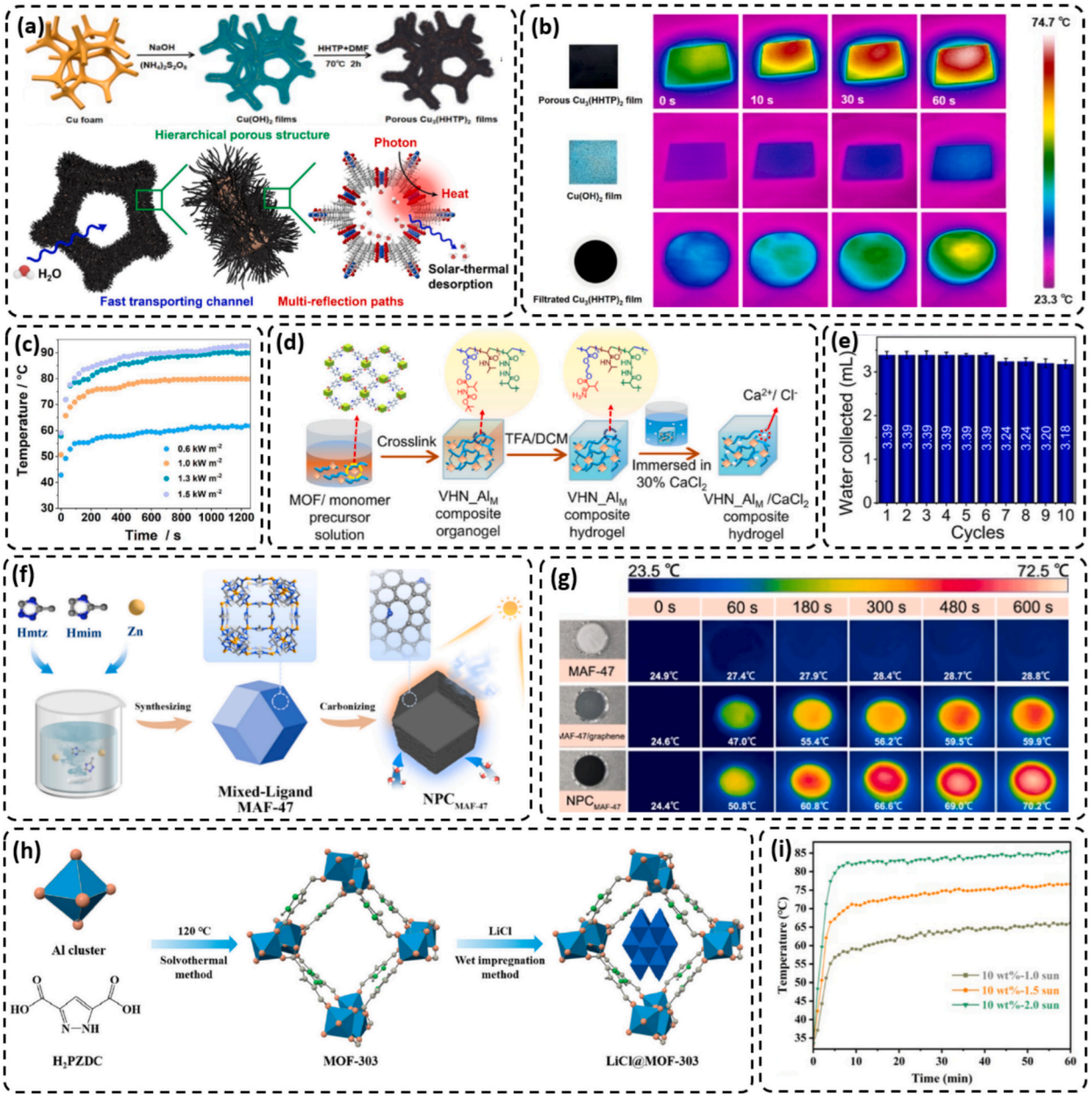

Fig. 17. (a) Hierarchical $Cu_3(HHTP)_2$ film structure enabling fast vapor transport and solar heat absorption [331]. (b) Visual and thermal comparison of porous $Cu_3(HHTP)_2$, $Cu(OH)_2$, and filtrated films under sunlight [331]. (c) Surface temperature evolution of $Cu_3(HHTP)_2$ film at various solar intensities [331]. Copyright 2025 Elsevier (Open Access). (d) Fabrication schematic of hydrogel@MOF/$CaCl_2$ composite [332]. (e) Cyclic performance test of the hydrogel@MOF/$CaCl_2$ system under repeated solar heating [332]. Copyright 2025 WILEY (Open Access). (f) Synthesis steps and water harvesting scheme for NPCMAF-47 [333]. (g) Surface heating profiles and IR images of NPCMAF-47 and controls under solar exposure [333]. Copyright 2025 American Chemical Society (Open Access). (h) Preparation and design of MOF-303@LiCl [334]. (i) Water uptake comparison of MOF-303@LiCl with other sorbents at 50% RH [334]. Copyright 2025 Royal Society of Chemistry.

six water generation cycles per day in the SAWH system, with a daily water yield of 0.42 L kg^{-1}. This dual-functional design, combining directional photothermal conversion with efficient sorption properties, represents a significant advancement in MOF-based SAWH. It emphasizes material asymmetry and internal thermal management as effective strategies for improving water harvesting in energy-limited, arid environments. In a closely related study, Cheng et al. tackled a critical triad of challenges limiting the deployment of MOF-based sorbents for SAWH: insufficient hydrophilicity at low RH, poor cycling stability, and limited functional adaptability [69]. Their work introduces a post-synthetic modification strategy in which MOF-808 is structurally reinforced via coordination with EDTA, yielding a multifunctional sorbent (E-MOF-808) (Fig. 16i). The EDTA ligand, due to its strong hydrophilicity and chelating capability, effectively lowers the moisture adsorption threshold, enabling a fivefold increase in water uptake (0.39 g g^{-1} at 25 % RH) compared to pristine MOF-808, while simultaneously stabilizing the framework over 50 adsorption–desorption cycles with negligible capacity loss. This level of durability directly addresses the instability seen in prior-generation MOFs under cyclic SAWH conditions. Moreover, E-MOF-808 demonstrates a secondary functional dimension. By leveraging the coordination affinity of EDTA, copper ions can be spontaneously incorporated, enabling in-situ deposition of CuS NPs. The E-MOF-808@CuS sorbent achieved a water uptake of 0.33 g g^{-1} within 360 min under 35–45 % RH and 24–26 °C, with solar-driven desorption under 1.0 sun, demonstrating practical adsorption–desorption performance. Taken together, this study offers an integrated material platform that unites high-capacity sorption at low RH, excellent recyclability, and on-demand solar water release.

For all-day, weather-independent operation, Wu et al. developed an adaptive all-day SAWH system by combining monolithic MOFs with a spray-applied Ti_3C_2 MXene/silane-decorated hyperbranched polymer (Ti_3C_2/sHBP) coating (TCMs) [370]. This innovative coating imparts dual-mode heating (solar and electrical) enabling flexible, low-energy water desorption throughout varying sunlight conditions. The TCMs demonstrated the ability to switch between solar-only, hybrid solar/electrical, and electrical-only desorption modes based on sunlight availability (Fig. 16j). The TCM showed a water vapor adsorption capacity of 0.31 g g^{-1} at 0.35 P/P_0 and 25 °C, which was lower than the bare Al-Fum monolith (0.39 g g^{-1}) due to the Ti_3C_2/sHBP coating with limited water affinity. Under simulated environmental conditions (35 % RH, 25 °C), the system achieved 1.80 L kg^{-1} day^{-1} productivity with 28.8 % lower electrical energy consumption compared to fully electrical-driven AWH at comparable yield (1.84 L kg^{-1} day^{-1}). The sprayable nature of the Ti_3C_2/sHBP solution also offers a facile and scalable pathway for coating pre-formed MOF monoliths without compromising their structure or performance. This study introduces a cost-effective and easily deployable dual-heating strategy for MOF-based SAWH systems, expanding their operational feasibility across day-night cycles and fluctuating weather conditions. Additionally, Zhang et al. introduced a composite SAWH system by vertically growing MOF nanosheets (Zn-TCPP) onto a crosslinked chitosan (CT)/PVA hydrogel membrane (MOF-CT/PVA), addressing the limited water retention of single-component MOFs (Fig. 16k) [371]. The directional alignment of the Zn-TCPP-based MOF nanosheets formed a superhydrophilic coating and continuous pore channels, promoting ultrafast vapor transport and efficient water capture. The MOF-CT/PVA composite exhibited water uptake of 1.21 g g^{-1} within 30 min at a relatively low RH of 30 % and demonstrated high cycling durability over 10 full adsorption–desorption cycles. Notably, to enable practical water recovery, the authors utilized the solar-thermal properties of Zn-TCPP combined with the morphology-induced enhanced solar exposure of the vertically aligned structure. Under 1 sun illumination, the surface temperature of the membrane reached 56.9 °C within 10 min, enabling rapid desorption. Thanks to the photothermal effect and interfacial energy differences between the MOF layer and hydrogel, 97 % of the captured water was released within 10 min under sunlight. Over 10 cycles of 30-min adsorption and 10-min desorption, the composite maintained a stable water collection performance of 4.18 g g^{-1} and an average desorption rate of 97.4 %, confirming both efficiency and structural robustness. This work demonstrates a scalable and durable SAWH approach that combines ultrafast kinetics, high capacity, and sunlight-driven regeneration, presenting a compelling solution for freshwater generation in resource-constrained environments. A different strategy by Guo et al. involved LiCl-decorated porous carbon (PC) sorbents derived from LiMOF (termed PCl), synthesized through high-temperature pyrolysis followed by hydrogen chloride (HCl) vapor treatment [372]. This approach addresses key challenges in SAWH, such as limited cycling stability, slow kinetics, and poor salt utilization, by integrating hygroscopic LiCl uniformly into a photothermally active porous framework. The resulting PCl sorbents achieved exceptionally high-water uptake, with a maximum capacity of 7.87 g g^{-1} across a broad humidity range, including 1.34 g g^{-1} at 20 % RH and 4.23 g g^{-1} at 80 % RH, significantly outperforming bulk LiCl in both adsorption and desorption kinetics. Under solar illumination, 0.83 L kg^{-1} of water was collected in 5.5 h, showcasing the material's ability to rapidly capture and release moisture using natural sunlight. Furthermore, the PCl materials demonstrated excellent cyclic stability, retaining high performance across eight consecutive cycles. By leveraging MOF-derived porosity and stable LiCl dispersion, this work presents a scalable and effective strategy for developing next-generation solar-responsive sorbents.

In 2025, the pace of SAWH research accelerated significantly, with the number of studies published by mid-year already matching the total output of 2024. This surge reflects continued advancements along three major trajectories: monolithic photothermal architectures, multifunctional composite sorbents, and defect-engineered or salt-integrated frameworks optimized for low-humidity environments.

Recent efforts in SAWH material design have shifted toward monolithic architectures to overcome the limitations of powdered MOFs in scalability, mechanical stability, and thermal transport. For instance, Wei et al. responded to a key bottleneck in MOF-based SAWH: the limited scalability and functionality of powdery sorbents, which restrict both mass transport and solar-driven desorption [373]. To overcome this, they developed a monolithic, free-standing film of $Cu_3(HHTP)_2$ (HHTP: 2,3,6,7,10,11-hexahydroxytriphenylene) with a hierarchical porous architecture designed to integrate rapid water uptake and efficient photothermal response (Fig. 17a). By engineering the film's multiscale porosity, the authors unlock two crucial advantages: (1) enhanced capillary-driven water vapor transport, and (2) extended optical path lengths that amplify solar absorption. Under just 1 sun (1 kW m^{-2}) irradiation, the surface temperature of the film reaches 75 °C within 60 s and 92 °C under higher flux (1.5 kW m^{-2})-sufficient for rapid water desorption (Fig. 17b,c). $Cu_3(HHTP)_2$ shows efficient water uptake at $P/P_0 = 0.20$ and 25 °C, reaching 0.24 g g^{-1} with a steep rise below this point,

and achieves a notable water harvesting rate of 8.16 $g\ m^{-2}\ h^{-1}$ at just 20 % RH, making it promising for arid environments. Compared to traditional powder or filtered-film MOFs, the monolithic configuration retains structural integrity, eliminates interfacial resistance, and facilitates scalable integration in real-world devices. Thermal imaging and time-resolved heating tests confirm the superior photothermal conversion kinetics, far exceeding that of control materials (e.g., $Cu(OH)_2$ or unstructured $Cu_3(HHTP)_2$). This work provides more than just incremental improvement: it redefines the physical form factor of SAWH sorbents, transforming MOFs from fragile, powder-bound materials into mechanically robust, high-throughput harvesting membranes. It serves as a template for unifying adsorption and desorption within a single-phase material, thereby reducing design complexity and operational overhead in SAWH systems.

By integrating photothermal, hygroscopic, and hydrogel components, multifunctional composites emerge as dual-purpose materials capable of both atmospheric water capture and solar-driven desalination. For instance, Sahoo and Tripathi tackled the multidimensional challenges of SAWH by engineering a multifunctional hydrogel composite (VHN_AlM/$CaCl_2$) that combines N-isopropyl acrylamide-based thermoresponsive hydrogel (PNIPAM), a photothermal MOF (NH_2-MIL-53(Al)), and hygroscopic $CaCl_2$ salt into a single sorbent platform (Fig. 17d) [374]. Their approach reflects a deliberate material design strategy where each component serves a distinct yet synergistic role: PNIPAM introduces thermally triggered phase transitions for controlled adsorption–desorption, $CaCl_2$ drives hygroscopicity, and the MOF enhances porosity and solar-induced heating. The composite achieves remarkable water sorption performance of 4.48 $g\ g^{-1}$ at 90 % RH and 0.62 $g\ g^{-1}$ at 50 % RH, with nearly full desorption (~100 %) within 30 min at just 40 °C. This temperature threshold is significantly lower than those required by conventional desorption methods, thus pointing to energy-efficient regeneration. The integration of photothermal capability via NH_2-MIL-53(Al) ensures rapid thermal response under 1 sun, reaching 38 °C within 10 min, allowing desorption even under modest solar conditions. What distinguishes this study is the dual-functionality of the composite: not only does it serve as a high-performance SAWH sorbent, but it also enables solar-driven desalination, reaching a high evaporation rate of 2.98 $kg\ m^{-2}\ h^{-1}$ at 90 % RH. Though the MOF content is relatively low (7.5 %), the photothermal effect remains sufficient to produce 6.31 mL of freshwater over 3 h, indicating optimized light-to-heat conversion within the porous-hydrogel matrix. Additionally, the material demonstrates cyclic stability, with only a 6 % drop in performance over 10 cycles, and retains functionality in outdoor conditions (85 ± 10 % RH, 32 ± 4 °C) (Fig. 17e). This robustness, combined with its broad environmental adaptability, supports the composite's potential as a dual-purpose water harvesting and purification system for decentralized and off-grid deployment. In sum, this work shifts the paradigm from monofunctional sorbents toward modular, hybridized water materials capable of efficient, low-energy SAWH and desalination.

Addressing water scarcity in arid regions requires adsorbents with enhanced performance at low RH, achieved through salt incorporation and defect-doping strategies. For instance, Lin et al. introduced a novel nitrogen-enriched NC adsorbent ($NPC_{MAF\text{-}47}$) engineered from a mixed-ligand metal-azolate framework (MAF-47) for efficient SAWH under arid conditions (Fig. 17f) [375]. By leveraging defect-rich carbon structures and nitrogen functional groups, the $NPC_{MAF\text{-}47}$ material achieves exceptional water adsorption performance, particularly in low-humidity environments. At 30 % RH, $NPC_{MAF\text{-}47}$ delivers a high-water uptake capacity of 405 $mg\ g^{-1}$ and a record water production rate of 542 $mg\ g^{-1}h^{-1}$, exceeding the performance of all previously reported SAWH adsorbents under similar RH conditions. The superior performance is attributed to the synergistic effects of nitrogen doping and carbon defects, as revealed by DFT simulations, which show enhanced charge redistribution and stronger interaction with water molecules. These structural and chemical advantages translate into rapid adsorption–desorption kinetics. The $NPC_{MAF\text{-}47}$ reaches 70.2 °C under 1 sun (1 $kW\ m^{-2}$) in just 10 min, confirming its strong photothermal conversion capability without needing external light absorbers or thermal conductors (Fig. 17g). Operational optimization revealed that a 15-minute adsorption phase followed by a 10-minute desorption cycle under solar irradiation delivers optimal performance, which remained stable over 10 consecutive cycles. This reflects both the reversible behavior and the excellent long-term stability of $NPC_{MAF\text{-}47}$. Moreover, compared to benchmark materials such as pristine MAF-47 and graphene-MOF composites, $NPC_{MAF\text{-}47}$ exhibits significantly higher thermal response, surface temperature, and sustained water productivity. This study provides compelling evidence for the feasibility of defect–nitrogen synergy in porous carbon structures for next-generation AWH systems. The combination of high surface area, microporosity, photothermal responsiveness, and robust cycling stability positions $NPC_{MAF\text{-}47}$ as one of the most effective materials currently available for SAWH in low-humidity, arid environments. In another study, Tian et al. present a novel composite adsorbent, MOF-303@LiCl-CB, designed to overcome limitations in conventional MOF-based SAWH materials, particularly under low RH conditions [116]. While MOF-303 is a stable and robust material suitable for water uptake at RH ≤ 30 %, its standalone adsorption capacity remains insufficient for scalable deployment. To address this, the researchers embedded LiCl, a highly hygroscopic salt, into the porous framework of MOF-303 to create MOF-303@LiCl (Fig. 17h), thereby significantly enhancing water uptake and kinetics while mitigating the salt's inherent problems of deliquescence, agglomeration, and leakage. The resulting composite exhibited a high-water adsorption capacity of 0.61 $g\ g^{-1}$ at 30 % RH and 25 °C, with adsorption saturation achieved within 80 min. Notably, to enable solar-driven desorption, the team incorporated CB as a photothermal material, producing the MOF-303@LiCl-10 wt% CB composite. Under 1 sun (1 $kW{\cdot}m^{-2}$) and 50 % RH, the surface temperature of the composite increased rapidly, reaching 66.1 °C (Fig. 17i), which was sufficient to induce complete water desorption within 60 min-without any optical focusing or auxiliary energy input. The system demonstrated effective thermal responsiveness across multiple solar intensities (1.0, 1.5, and 2.0 suns), suggesting adaptability to varying environmental conditions. Importantly, the MOF-303@LiCl-CB composite demonstrated excellent stability over repeated adsorption–desorption cycles, consistently harvesting 0.5 g of water per cycle with a desorption rate of ~ 0.21 $g\ g^{-1}\ h^{-1}$. Its robust cycling performance, rapid sorption kinetics, and compatibility with passive solar heating make it well-suited for off-grid water generation in arid environments.

A new class of multifunctional composites is emerging that enables both AWH and solar-driven purification, expanding the utility of SAWH systems beyond moisture capture alone. For instance, Shang et al. developed an innovative multifunctional composite material, WCBs@SA/MNPs/MOFs, which simultaneously enables efficient SAWH [376]. This dual-purpose material is fabricated using

waste cigarette butts (WCBs) as a porous support, combined with SA for structural integrity, MOF-801 for high hygroscopicity, and melanin NPs (MNPs) for photothermal conversion. The fabricated WCBs@SA/MNPs/MOFs effectively capture water even under low-humidity conditions (20 % RH), achieving a water uptake capacity of 0.24 g g^{-1}. The unique synergy of these components imparts WCBs@SA/MNPs/MOFs with exceptional water vapor sorption and solar responsiveness. Under low-humidity conditions (20 % RH), the material delivers daily water harvesting of 1.41 L kg^{-1}, increasing to 5.42 L kg^{-1} at 80 % RH. Simultaneously, under 1 sun (1 kW m^{-2}) solar irradiation, it achieves a high evaporation rate of ~ 2.72 kg $m^{-2}h^{-1}$, effectively purifying undrinkable water. This dual functionality makes the material particularly attractive for deployment in arid or off-grid regions where access to both clean air-sourced water and water purification solutions is limited. Notably, the use of discarded cigarette butts, a major pollutant, as a base material not only mitigates environmental waste but also adds value to what is typically a harmful refuse. The study demonstrates that WCBs@SA/MNPs/MOFs competes with, or outperforms, many existing SAWH systems and photothermal materials in terms of both capacity and sustainability. It offers a compelling solution for decentralized freshwater generation while addressing environmental pollution, thus contributing to global efforts in water security and circular resource utilization.

In summary, MOFs have not only redefined the material landscape of SAWH through their tunable porosity and multifunctionality but have also established themselves as the most promising class of sorbents for enabling high-efficiency, low-energy, and scalable SAWH systems.

7. Progress in SAWH devices

AWH devices can be broadly categorized into passive and active devices, depending on their mode of operation and energy requirements. Passive devices operate without the need for external power sources or mechanical components. They rely on natural air flow, ambient temperature fluctuations, and solar energy to drive the adsorption and desorption processes. These systems are particularly attractive for their energy efficiency, simplicity, and suitability for off-grid or remote applications. Active devices incorporate mechanical ventilation and external heating and cooling systems to enhance water vapor adsorption and condensation. By actively controlling airflow and temperature, these systems can perform multiple cycles per day, making them effective in a wide range of environmental conditions but with higher energy demands.

In SAWH devices, the overall water productivity is fundamentally governed by coupled heat and mass transfer processes occurring within the sorbent layer, adsorbent surface, and condenser unit. In these devices, heat-induced desorption and cooling-induced condensation are the major energy-consuming processes. Key parameters-including the thermal conductivity and thickness of the

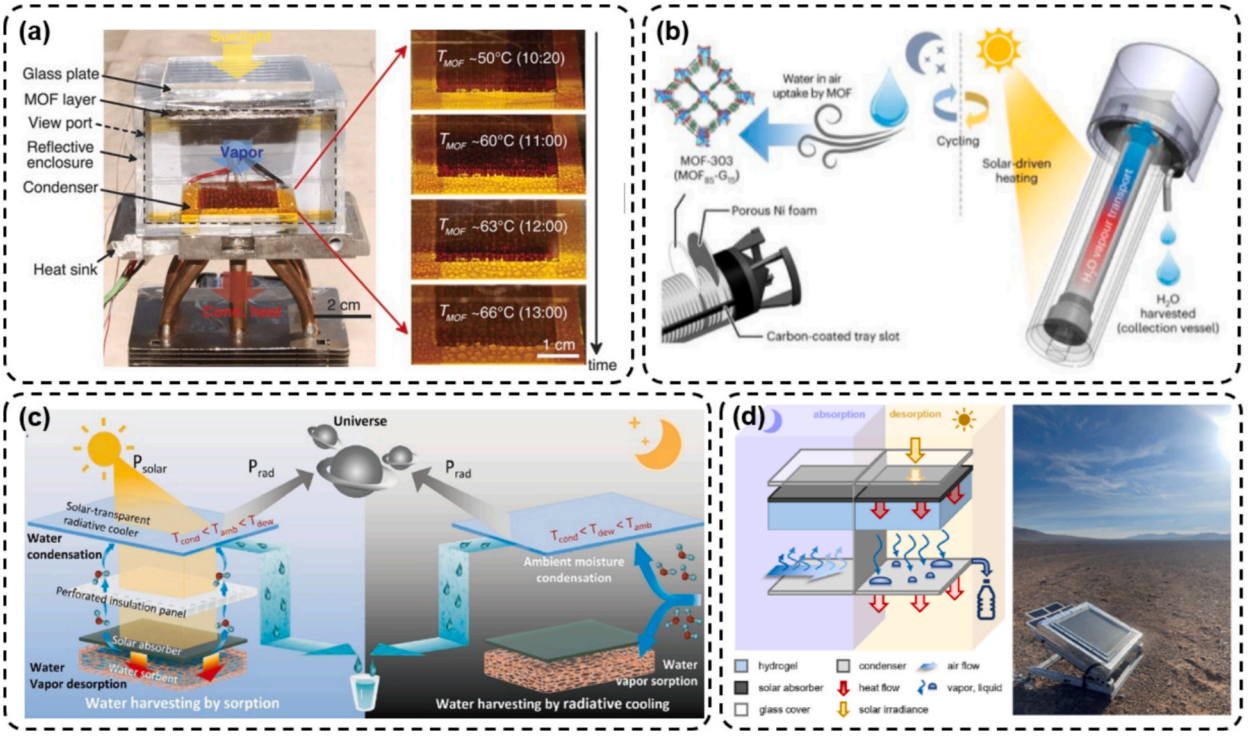

Fig. 18. Evolution of passive SAWH device architectures from concept to advanced system-level designs. (a) Initial prototype using diurnal humidity cycles [25]. Copyright 2017 Science (Open Access). (b) Modular cylindrical design with enhanced solar utilization and thermal insulation [336]. Copyright 2023 Nature. (c) Integrated all-day radiative cooling system for improved water collection and condensation [337]. Copyright 2024 Royal Society of Chemistry. (d) System-optimized hydrogel-salt composite device combining material and thermal modeling for scalable passive SAWH applications [338]. Copyright 2025 Elsevier (Open Access).

sorbent bed, the absorber-condenser temperature gradient, vapor diffusion resistance within the porous media, solar absorptance of the photothermal layer, and ambient convection-directly control adsorption rates during nighttime and desorption/condensation efficiency during daytime operation [105 377]. Recent studies have quantified these effects using detailed experimental temperature mapping and multiphysics simulations. For instance, Kim et al. demonstrated that incomplete heat delivery across the MOF-801 bed limits desorption kinetics, making thermal uniformity essential for maximizing daytime vapor flux [359]. Similarly, Song et al. showed that the incorporation of vacuum insulation, sun-tracking, and thin disc-shaped MOF layers significantly enhances heat transfer into the sorbent bed and reduces vapor transport resistance, thereby improving solar utilization efficiency [378]. Radiative-cooling-based passive devices have also confirmed that reducing condenser temperature by even 5–10 °C substantially increases the driving force for vapor condensation, thereby boosting overall mass transfer and water recovery efficiency [379]. To enhance condensation, Xu et al. implemented an insulation plate between the sorbent and condenser, increasing the temperature difference by 9 °C, and used strip aluminum fin radiators to improve heat dissipation [113]. Shao et al. designed an external condenser connected via a KF 25 flange, which minimized heat loss and leveraged pressure-driven buoyancy for higher vapor flow, further aided by finned structures for effective cooling [380]. Wang et al. demonstrated that actively maintaining the dew point of desorbed vapor above ambient temperature using air-cooled condensers significantly enhances water recovery [381]. Additionally, LaPotin et al. proposed a dual-stage condensation system that recovers latent heat from the top stage to drive desorption in the bottom stage, effectively doubling daily water productivity [382]. These results collectively highlight that SAWH performance is strongly dictated not only by sorbent chemistry but also by the engineered thermal and mass-transport environment surrounding the material. Blending MOFs with conductive additives and optimizing the enclosure design can enhance heat transfer to the sorbent while maintaining sufficient temperature gradients for water desorption and condensation [105 377].

Furthermore, the distinction between passive and active AWH systems is directly reflected in their energy consumption-productivity relationship. Passive SAWH devices rely entirely on solar heating and natural cooling, enabling energy-free operation but limiting daily cycling frequency. Typical water productivities of passive MOF-based systems fall in the range of 0.58–2.8 L kg^{-1} day^{-1} under 20–30 % RH [377 121], constrained by diurnal thermal swings and equilibrium adsorption capacity. In contrast, active devices-equipped with forced convection, electrical heaters, and compressor-based condensers-achieve multiple cycles per day and significantly greater water output. For instance, an active MIL-101(Cr) device utilizing cooling-assisted adsorption achieved a productivity of 7.75–22.81 L kg^{-1} day^{-1} across various climates (10–35 °C, 20–80 % RH). In a practical field trial, the system generated 990.4 mL of water at 26 % RH, corresponding to a daily productivity of 9.9 L kg^{-1}, with an energy consumption of 2.96 kWh L^{-1} [383]. These comparisons emphasize the fundamental trade-off: passive devices offer sustainability and zero operational energy, whereas active systems deliver higher water yield at a markedly higher energy cost.

Our study focuses specifically on passive SAWH systems, where both adsorption and desorption phases are facilitated by natural humidity and temperature variations over the day-night cycle. These systems exemplify the potential for low-energy, sustainable water generation, particularly in arid and resource-limited environments. In the following, we review key representative devices developed within this passive framework.

The initial conceptual demonstration by Kim et al. in 2017 marked an important milestone [27]. Their prototype employed a MOF-801 layer enclosed within a simple shell and integrated with a basic condenser. The system relied entirely on natural diurnal cycles, adsorbing water vapor overnight and releasing it under sunlight during the day (Fig. 18a). Despite its modest and lightweight construction, the device effectively validated the practical feasibility of MOFs in off-grid, solar-driven water harvesting. However, the simplified geometry and limited surface area of the adsorbent bed posed challenges to upscaling and practical deployment. Addressing these limitations, a more advanced version of the device was introduced by Song et al. in 2023 [378]. This second-generation design adopted a modular and cylindrical configuration, enhancing both thermal management and solar energy utilization. Key improvements included the use of vacuum-insulated housing, sun-tracking alignment, and a restructured MOF bed composed of thin, disc-shaped particles stacked with porous metal foam layers (Fig. 18b). These modifications significantly increased the active surface area and improved heat distribution within the sorbent layer, leading to a notable boost in operational efficiency. The device maintained a fully passive profile (powered only by sunlight) while offering greater potential for large-scale and economically viable deployment. Beyond traditional solar-driven systems, Xu et al. in 2024 proposed a novel direction by integrating radiative cooling into the AWH design [384]. Their all-in-one hybrid unit combined daytime and nighttime radiative effects to enhance both water adsorption and condensation. By lowering the condenser temperature through passive radiative cooling, the device achieved better thermal separation and more effective water collection (Fig. 18c). The design emphasized compactness, portability, and low manufacturing cost, presenting a highly integrated solution with promise for real-world use. Furthermore, the incorporation of techno-economic evaluation underscored the importance of not only adsorbent development but also the engineering optimization of device components such as condensers, insulators, and structural elements to achieve high performance under minimal energy input.

Building on these developments, recent studies have shifted focus toward holistic system-level design and optimization of passive atmospheric water harvesting devices. Emphasis has been placed on integrating sorbent materials within carefully engineered housings that maximize solar absorption, enhance vapor confinement, and improve condensation efficiency. By employing advanced heat and mass transfer models, these devices are tailored to balance water productivity and thermal efficiency, enabling effective operation even in extreme environments such as deserts. This system-oriented approach prioritizes scalable, low-cost, and energy-efficient designs that can reliably produce potable water off-grid. Such innovations highlight the crucial role of device engineering, beyond sorbent chemistry, in advancing atmospheric water harvesting technologies toward practical, real-world applications. In line with this system-level perspective, Wilson et al. in 2025 developed and experimentally validated a heat and mass transport model specifically for hydrogel-salt composite-based atmospheric water harvesting devices [385]. Their work integrates both material characteristics and device parameters to optimize performance. Utilizing this model, they designed a passive, solar-driven device that

effectively cycles a polyacrylamide-lithium chloride (PAM-LiCl) hydrogel-salt composite (Fig. 18d). The device demonstrated high water productivity and thermal efficiency across diverse environments, from urban settings to arid deserts, illustrating the potential of combining material innovation with comprehensive system design to overcome challenges in water scarcity.

Overall, the evolution from proof-of-concept to system-level optimized devices shows the growing practicality of passive AWH. Future work should integrate not only material and engineering advances but also life cycle and life cycle sustainability assessments (LCA and LCSA) to ensure long-term sustainability. Different applications-from portable units to community-scale systems-will require tailored designs, balancing cost, durability, scalability, and energy needs to deliver viable and responsible solutions to water scarcity.

8. Summary and outlook

Solar-driven atmospheric water harvesting (SAWH) has emerged as a transformative and sustainable approach to address freshwater scarcity, particularly in off-grid, arid, and resource-constrained environments. This technology leverages the synergy between advanced hygroscopic materials, most notably MOFs, and passive device architectures to enable decentralized, low-energy water generation directly from the atmosphere. Over the past decade, rapid progress has been made in both sorbent chemistry and device engineering, pushing the boundaries of what is feasible for real-world deployment.

From a materials standpoint, MOFs offer unparalleled structural tunability, enabling the design of sorbents with high water uptake at low relative humidity, steep adsorption isotherms, fast kinetics, and excellent cycling durability. Recent developments have focused on enhancing photothermal performance through ligand functionalization, hybridization with light-absorbing agents, and structural modifications such as defect engineering and heteroatom incorporation. These efforts aim to reduce the energy input required for water release, a major bottleneck in the practical viability of SAWH systems.

Equally important is the parallel advancement in device-level integration. Passive SAWH devices, which operate without mechanical components or external energy inputs, have demonstrated significant promise due to their simplicity, scalability, and energy efficiency. Initial demonstrations validated the feasibility of MOF-based water collection under natural diurnal cycles. Subsequent innovations, such as modular device architectures, sun-tracking systems, radiative cooling elements, and optimized sorbent geometries, have dramatically enhanced solar utilization, vapor confinement, and condensation efficiency. These improvements have translated into greater water productivity, thermal performance, and adaptability across diverse environmental conditions.

Critically, recent research has emphasized that optimizing SAWH performance requires a holistic, system-level approach. Beyond material innovation, the integration of high-performance insulators, engineered condensers, and advanced structural designs plays a crucial role in maximizing water yield. Multiphysics modeling and techno-economic assessments have further enabled the rational design of devices tailored for both urban and extreme desert environments. For instance, devices utilizing hydrogel-salt composites, embedded in passive solar frameworks, have shown promising results in maintaining high efficiency and water output across varying climates.

Another emerging focus is the quality of the harvested water. Volatile and semi-volatile organic compounds (VOCs and SVOCs), often originating from indoor environments or polluted air, can compromise the safety of collected water. Advanced MOF-based systems with molecular sieving functions or Fenton-like catalytic degradation mechanisms are being developed to purify the water during the capture or evaporation phase, ensuring that the final output meets potable standards.

Beyond performance optimization of MOF-based SAWH systems, several studies have emphasized that synthesis cost, raw-material availability, large-scale manufacturability, and performance degradation upon scale-up are critical constraints that significantly limit MOF commercialization [386]. Techno-economic analyses have shown that expensive solvents (e.g., N,N'-dimethylformamide (DMF), N,N'-diethylformamide (DEF)) can contribute up to 90 % of total production cost, making the solvent burden the dominant cost factor in many MOFs [387]. In some systems such as HKUST-1, raw materials account for more than 60 % of the overall cost, while in materials like MOF-5, combined solvent and precursor costs exceed 90 % [387]. Raw-material selection also represents a major barrier: commonly used metal nitrates and chlorides pose serious hazards (oxidation, decomposition, explosion risks, corrosion) at large scale, necessitating substitution with safer but less soluble salts such as acetates or sulfates [388]. Likewise, widely used organic linkers (e.g., Terephthalic Acid, Trimesic Acid) are petrochemical-derived and expensive at industrial quantities, limiting scalability and motivating the use of recycled or bio-based linkers [388]. From a manufacturing standpoint, only a few companies have demonstrated multi-kilogram production with acceptable quality, and large-scale synthesis remains limited by long reaction times, heavy solvent consumption, lack of regulatory standards, and extensive post-treatments [386 388]. Collectively, cost structure, material availability, industrial safety, and quality retention during scale-up are essential considerations that must accompany performance-focused research on MOFs for SAWH applications. Additionally, the long-term stability of MOFs under repeated water adsorption/desorption cycles is a crucial consideration. Some MOFs may experience performance degradation over extended operation, which could reduce their effective water uptake and compromise device reliability. Addressing these stability issues through framework engineering, protective coatings, or selection of inherently robust MOFs is therefore essential for practical applications.

Looking forward, the development of scalable, cost-effective, and durable SAWH systems will require continued interdisciplinary collaboration. Key future directions include:

- Material Design: Creating highly porous, hydrophilic, and photothermally active MOFs with high hydrolytic stability, while relying on abundant, low-cost, and environmentally benign components. This can be facilitated through the adoption of greener synthesis routes, the use of earth-abundant metal precursors and bio-derived linkers, and scalable post-synthetic strategies that enhance hydrophilicity and photothermal activity without increasing production complexity. In addition, employing energy-efficient

activation methods and mild chemical modification routes can further improve stability and performance while maintaining compatibility with large-scale manufacturing.
- Mechanistic understanding: gaining deeper insight into water adsorption–desorption mechanisms, heat and mass transfer dynamics, and the role of defects, functional groups, and pore architecture in governing performance, facilitating further improvement.
- Process Integration: Coupling SAWH materials with efficient solar concentrators, heat exchangers, or hybrid desalination and purification units to maximize water yield under real-world conditions
- Device Engineering: Advancing passive configurations through better thermal insulation, droplet removal strategies, and adaptive condensation surfaces.
- Operational Flexibility: Transitioning from intermittent to continuous 24-hour harvesting cycles using smart thermal management or auxiliary energy sources (e.g., battery discharge, radiative cooling).
- Water Safety Assurance: Implementing integrated filtration and VOC-removal mechanisms to ensure consistent water quality.
- Scalability and Sustainability: Designing modular, low-cost devices and validating them through long-term outdoor operation under real-world conditions. Assessing environmental impact, recyclability, and techno-economic feasibility to guide commercialization pathways.

A significant challenge that continues to limit the advancement and large-scale implementation of SAWH systems is the absence of standardized methodologies for evaluating and reporting material and device performance. Current studies employ widely different operating conditions like spanning relative humidity, temperature, solar flux, cycle duration, and testing protocols, while reporting key metrics such as adsorption capacity, water productivity, energy consumption, and desorption efficiency using inconsistent units. This heterogeneity complicates cross-comparison and obscures the identification of genuinely high-performance sorbents and device architectures. Several recent studies have begun outlining preliminary methodological frameworks for standardizing SAWH performance reporting. For example, a widely referenced guideline proposes seven key performance indicators (KPIs) [389] as baseline metrics for comparative evaluation across laboratories, including capacity (maximum water uptake in mL g^{-1}, g g^{-1}, or mol g^{-1}, measured via static sorption), sensitivity (adsorption onset relative pressure, p p^{-1} %, by static sorption), reversibility (hysteresis loop characterization from static sorption), regeneration condition (% water recovery after desorption, static sorption), chemical stability (number of stable adsorption–desorption cycles, static sorption), kinetics (daily water yield in L kg^{-1} day^{-1}, dynamic sorption), and harvested-water quality (six parameters analyzed via standardized WHO-aligned methods: 50, 2130, 5910, 2510, 2340, and 4500). Together, such emerging KPI-based frameworks provide a practical foundation for harmonizing reporting practices and improving cross-study comparability, offering an initial step toward the universal performance standards required for the advancement and real-world adoption of SAWH technologies. While such early frameworks represent an important first step toward unified benchmarking, further refinement is still needed to incorporate device-level metrics, environmental variability, long-term durability, and techno-economic considerations to fully enable fair comparison, accelerate material screening, and guide SAWH technologies toward robust, real-world deployment.

In conclusion, SAWH using MOF-based systems offers a compelling solution for off-grid water generation. While significant strides have been made in both material and system design, bridging the gap between laboratory success and field-ready applications remains a priority. With the integration of high-performance materials, smart engineering, and sustainable design principles, SAWH technology is poised to play a pivotal role in the future of clean water access, bringing us closer to achieving water security for all.

CRediT authorship contribution statement

M. Arjmandi: Writing – original draft, Visualization, Methodology, Investigation, Formal analysis, Conceptualization. **M. Khayet:** Writing – review & editing, Visualization, Supervision, Resources, Project administration, Methodology, Investigation, Funding acquisition, Formal analysis, Conceptualization. **P. Horcajada:** Writing – review & editing, Visualization, Methodology, Investigation, Formal analysis, Conceptualization.

Declaration of competing interest

The authors declare that they have no known competing financial interests or personal relationships that could have appeared to influence the work reported in this paper.

Acknowledgement

This work was supported by the European Union under the Marie Skłodowska-Curie Actions (MSCA), HORIZON-MSCA-2023-PF-01-01, through the PHOTOWAT project (Grant Agreement No. 101154984, DOI: 10.3030/101154984), coordinated by Universidad Complutense de Madrid (UCM), Spain. This publication is part of the project PID2022-138389OBC31, funded by MICIU/AEI/10.13039/501100011033/FEDER, UE (Spain; MICIU: Ministerio de Ciencia, Innovación y Universidades; AEI: Agencia Estatal de Investigación; FEDER, UE: Fondo Europeo de Desarrollo Regional, Cofinanciado por la Unión Europea).

Data availability

Data will be made available on request.

References

[1] Arjmandi M, Chenar MP, Altaee A, Arjmandi A, Peyravi M, Jahanshahi M, et al. Caspian seawater desalination and whey concentration through forward osmosis (FO)-reverse osmosis (RO) and FO-FO-RO hybrid systems: Experimental and theoretical study. J Water Process Eng 2020;37:101492.
[2] Fanzo J. Understanding human water turnover in times of water scarcity. Cell Metab 2023;35:231–2.
[3] Dorian JP, Franssen HT, D. r. s. md.. Global challenges in energy. Energy Policy 2006;34:1984–91.
[4] Okampo EJ, Nwulu N. Optimisation of renewable energy powered reverse osmosis desalination systems: a state-of-the-art review. Renew Sustain Energy Rev 2021;140:110712.
[5] Hunt JD, Al-Nory MT, Slocum AH, Wada Y. Integrated seasonal pumped hydro, cooling, and reverse osmosis: a solution to desert coastal regions. Desalination 2025;593.
[6] Nassrullah H, Anis SF, Hashaikeh R, Hilal N. Energy for desalination: a state-of-the-art review. Desalination 2020;491:114569.
[7] Xu W, Yaghi OM. Metal-organic frameworks for water harvesting from air, anywhere, anytime. ACS Cent Sci 2020;6:1348–54.
[8] Arjmandi M, Aytaç E, Khayet M, Hilal N. Next-generation MOFs for atmospheric water harvesting: the role of machine learning techniques. Coord Chem Rev 2026;548:217211.
[9] Zhou M, Song H, Xu X, Shahsafi A, Qu Y, Zhenyang Xia ZM, et al. Vapor condensation with daytime radiative cooling. *Applied Physical*. Sciences 2020;118: e2019292118.
[10] Chen H, Ran T, Gan Y, Zhou J, Zhang Y, Zhang L, et al. Ultrafast water harvesting and transport in hierarchical microchannels. Nat Mater 2018;17:935–42.
[11] Laha S, Maji TK. Binary/Ternary MOF Nanocomposites for Multi-Environment Indoor Atmospheric Water Harvesting. Materials, Advanced Functional 2022; 32:2203093.
[12] Wahlgren RV. Atmospheric water vapour processor designs for potable water production: a review. Water Res 2001;35:1–22.
[13] Gido B, Friedler E, Broday DM. Assessment of atmospheric moisture harvesting by direct cooling. Atmos Res 2016;182:156–62.
[14] Si Y, Dong Z, Jiang L. Bioinspired designs of Superhydrophobic and Superhydrophilic Materials. ACS Cent Sci 2018;4:1102–12.
[15] From Materials to Chemistry. B. Su||, Y. Tian and L. Jiang. Bioinspired Interfaces with Superwettability. J Am Chem Soc 2016;138:1727–48.
[16] Zhang X, Sun L, Wang Y, Bian F, Wang Y, Zhao Y. Multibioinspired slippery surfaces with wettable bump arrays for droplets pumping. Engineering 2019;116: 20863–8.
[17] Wan K, Gou X, Guo Z. Bio-inspired fog Harvesting Materials: Basic Research and Bionic potential applications. J Bionic Eng 2011;18:501–33.
[18] Guo S, Zhang Y, Tan SC. Device design and optimization of sorption-based atmospheric water harvesters. Device 2023;1:100099.
[19] Liu M, Wang S, Jiang L. Nature-inspired superwettability systems. Nat Rev Mater 2017;2:17036.
[20] Tu Y, Wang R, Zhang Y, Wang J. Progress and Expectation of Atmospheric Water Harvesting. Joule 2018;2:1452–75.
[21] Bai Z, Wang P, Xu J, Wang R, Li T. Progress and perspectives of sorption-based atmospheric water harvesting for sustainable water generation: Materials, devices, and systems. Science Bulletin 2024;69:671–87.
[22] Wang P, Xu J, Bai Z, Wang R, Li T. Designing next-generation all-weather and efficient atmospheric water harvesting powered by solar energy. Energ Environ Sci 2025;18:7005–22.
[23] Ansari E, Elwadood S, Balakrishnan H, Sapkaite I, Munro C, Karanikolos GN, et al. Sorption-based atmospheric water harvesters - perspectives on materials design and innovation. J Environ Chem Eng 2024;12:113960.
[24] Li C, Pan Q, Ying W, Shan H, Wang R, Zhang H, et al. Atmospheric water harvesting with scale-up potentials using natural sunlight and passive cooling. Natural Sciences 2023;3:e20220038.
[25] Li Q, Ying Y, Tao Y, Li H. Assemblable Carbon Fiber/Metal–Organic Framework Monoliths for Energy-Efficient Atmospheric Water Harvesting. Ind Eng Chem Res 2022;61:1344–54.
[26] Tao Y, Li Q, Wua Q, Li H. Embedding metal foam into metal–organic framework monoliths for triggering a highly efficient release of adsorbed atmospheric water by localized eddy current heating. Mater Horiz 2021;8:1439–45.
[27] Kim H, Yang S, Rao SR, Narayanan S, Kapustin EA, Furukawa H, et al. Water harvesting from air with metal-organic frameworks powered by natural sunlight. Science 2017.
[28] Hu Y, Ye Z, Peng X. Metal-organic frameworks for solar-driven atmosphere water harvesting. Chem Eng J 2023;452:139656.
[29] Hanikel N, Prévot MS, Yaghi OM. MOF water harvesters. Nat Nanotechnol 2020;15:348–55.
[30] Xu J, Wang P, Bai Z, Cheng H, Wang R, Qu L, et al. Sustainable moisture energy. Nat Rev Mater 2024;9:722–37.
[31] Ejeian M, Wang R. Adsorption-based atmospheric water harvesting Joule 2021;5:1678–703.
[32] Xiang T, Xie S, O. logo, G. Chen, C. Zhanga and Z. Guo. Recent advances in atmospheric water harvesting technology and its development. Mater Horiz 2025; 12:1084–105.
[33] Kalmutzki MJ, Diercks CS, Yaghi OM. Metal–Organic Frameworks for Water Harvesting from Air. Adv Mater 2018;30:1704304.
[34] Jia L, Hu Y, Liu Z, Hao H, Xu H, Huang W, et al. Porous materials MOFs and COFs: Energy-saving adsorbents for atmospheric water harvesting. Mater Today 2024;78:92–111.
[35] Lu H, Shi W, Guo Y, Guan W, Lei C, Yu G. Materials Engineering for Atmospheric Water Harvesting: Progress and Perspectives. Adv Mater 2022;34:2110079.
[36] Rezk A, Al-Dadah R, Mahmoud S, Elsayed A. Characterisation of metal organic frameworks for adsorption cooling. Int J Heat Mass Transf 2012;55:7366–74.
[37] Wang D, Zhang J, Tian X, Liu D, Sumathy K. Progress in silica gel-water adsorption refrigeration technology. Renew Sustain Energy Rev 2014;30:85–104.
[38] Elwadood SNA, Reddy KSK, Wahedi YA, Alili AA, Farinha AS, Witkamp G-J, et al. Hybrid salt-enriched micro-sorbents for atmospheric water sorption. J Water Process Eng 2023;52:103560.
[39] Ehtisham M, Saeed-Ul-Hassan M, Poater A. A comprehensive review of approaches, systems, and materials used in adsorption-based atmospheric water harvesting. Sci Total Environ 2025;958:177885.
[40] Arjmandi M, Altaee A, Arjmandi A, Chenar MP, Peyravi M, Jahanshahi M. A facile and efficient approach to increase the magnetic property of MOF-5. Solid State Sci 2020;106:106292.
[41] Arjmandi M, Chenar MP, Peyravi M, Jahanshahi M. Influence of As-formed Metal-Oxide in Non-Activated Water-Unstable Organometallic Framework Pores as Hydrolysis Delay Agent: Interplay between Experiments and DFT Modeling. J Inorg Organomet Polym Mater 2019;29:178–91.
[42] Furukawa H, Cordova KE, O'Keeffe M, Yaghi OM. The Chemistry and applications of Metal-Organic Frameworks. Science 2013;341.
[43] Batten SR, Champness NR, Chen X-M, Garcia-Martinez J, Kitagawa S, Öhrström L, et al. Terminology of metal–organic frameworks and coordination polymers (IUPAC Recommendations 2013). Pure Appl Chem 2013;85:1715–24.
[44] Yusuf VF, Malek NI, Kailasa SK. Review on Metal–Organic Framework Classification, Synthetic Approaches, and Influencing Factors: applications in Energy, Drug delivery, and Wastewater TreatmentClick to copy article link. ACS Omega 2022;7:44507–31.
[45] Sadiq S, Khan Sh, Khan I, Khan A, Humayun M, Wu P, et al. Bououdina M. A critical review on metal-organic frameworks (MOFs) based nanomaterials for biomedical applications: Designing, recent trends, challenges, and prospects. Heliyon 2024;10:e25521.
[46] Arjmandi M, Pakizeh M. Effects of washing and drying on crystal structure and pore size distribution (PSD) of Zn4O13C24H12 framework (IRMOF-1). Acta Metallurgica Sinica (English Letters) 2013;26:597–601.
[47] Wang W, Chen D, Li F, Xiao X, Xu Q. Metal-organic-framework-based materials as platforms for energy applications. Chem 2024;10:86–133.
[48] Osterrieth JWM, Fairen-Jimenez D. Metal–Organic Framework Composites for Theragnostics and Drug delivery applications. Biotechnol J 2021;16:2000005.

[49] Binaeian E, Motaghedi N, Maleki S, Arjmandi M. Ibuprofen uptake through dimethyl ethylenediamine modified MOF: optimization of the adsorption process by response surface methodology technique. J Dispers Sci Technol 2020;43:1–14.
[50] Arjmandi M, Peyravi M, Chenara MP, Jahanshahi M. Channelization of water pathway and encapsulation of DS in the SL of the TFC FO membrane as a novel approach for controlling dilutive internal concentration polarization. Environ Sci Water Res Technol 2019;5:1436–52.
[51] Zhang B, Zerui Zhu XW, Liu X, Kapteijn F. Water Adsorption in MOFs: Structures and applications. Adv Funct Mater 2024;34:2304788.
[52] Navalón S, Dhakshinamoorthy A, Álvaro M, Ferrer B, García H. Metal–Organic Frameworks as Photocatalysts for Solar-Driven overall Water Splitting. Chem Rev 2023;123:445–90.
[53] Haldar R, Heinke L, Wöll C. Advanced Photoresponsive Materials using the Metal–Organic Framework Approach. Adv Mater 2020;32:1905227.
[54] Medishetty R, Zaręba JK, Mayer D, Samoć M, Fischer RA. Nonlinear optical properties, upconversion and lasing in metal–organic frameworks. Chem Soc Rev 2017;46:4976–5004.
[55] Nguyen TN, Ebrahim FM, Stylianou KC. Photoluminescent, upconversion luminescent and nonlinear optical metal-organic frameworks: from fundamental photophysics to potential applications. Coord Chem Rev 2018;377:259–306.
[56] Younis SA, Kwon EE, Qasim M, Kim K-H, Kim T, Kukkar D, et al. Metal-organic framework as a photocatalyst: Progress in modulation strategies and environmental/energy applications. Prog Energy Combust Sci 2020;81:100870.
[57] Lu Y-L, Wang Y-P, Wu K, Pan M, Su C-Y. Activating Metal–Organic Cages by Incorporating Functional M(ImPhen)3 Metalloligands: from Structural Design to applications. Acc Chem Res 2024;57:3277–91.
[58] Naghdi S, Shahrestani MM, Zendehbad M, Djahaniani H, Kazemian H, Eder D. Recent advances in application of metal-organic frameworks (MOFs) as adsorbent and catalyst in removal of persistent organic pollutants (POPs). J Hazard Mater 2023;442:130127.
[59] B. Lü, P. L. Yifa Chen, B. Wang, K. Müllen and M. Yin. Stable radical anions generated from a porous perylenediimide metal-organic framework for boosting near-infrared photothermal conversion. *Nature Communications*. 10, 2019.
[60] Juan-Ding Xiao H-L-J. Metal–Organic Frameworks for Photocatalysis and Photothermal Catalysis. Acc Chem Res 2019;52:356–66.
[61] Xie LS, Skorupskii G, Dincă M. Electrically Conductive Metal–Organic Frameworks. Chem Rev 2020;120:8536–80.
[62] Luo Y, Liu X, Tan L, Li Z, Yeung KWK, Zheng Y, et al. Enhanced photocatalytic and photothermal properties of ecofriendly metal-organic framework heterojunction for rapid sterilization. Chem Eng J 2021;405:126730.
[63] Peng Y, Wei X, Wang Y, Li W, Zhang S, Jin J. Metal–Organic Framework Composite Photothermal Membrane for Removal of High-Concentration Volatile Organic Compounds from Water via Molecular Sieving. ACS Nano 2022;16:8329–37.
[64] Ren J, Zhang W, Xuan Z, Li L, Yuan W. Enhanced thermal storage and photo-thermal conversion composite phase change materials based on MOF-derived carbon for efficient solar energy utilization. J Storage Mater 2024;79:110180.
[65] Yu D, Han X, Wang S, Zhong L, Zhang L, Zhou M, et al. Flexible photothermal-triggered MOF-composite nanofibers textures for freshwater harvesting with high efficiency and stability. Sep Purif Technol 2024;331:125629.
[66] Shelonchik O, Lemcoff N, Shimoni R, Biswas A, Yehezkel E, Yesodi D, et al. Light-induced MOF synthesis enabling composite photothermal materials. Nat Commun 2024;15.
[67] Hou A, Du Y, Su Y, Pang Z, S. liu, S. Xian, X. Zhao, L. Ma, B. Liu, H. Wu and Z. Zhou. uS/Co-Ferrocene-MOF Nanocomposites for Photothermally Enhanced Chemodynamic Antibacterial Therapy. ACS Appl Nano Mater 2024;7:10998–1007.
[68] Li T, Sun J, Yin Y, Zhang Q, Wang C, Wang S. Photothermal/nitric oxide synergistic anti-tumour therapy based on MOF-derived carbon composite nanoparticles. Nanoscale 2022;14:16193–207.
[69] Cheng M, Lian X, Bai H, Wang X, Xu J, Cao M, et al. Optimizing Hygroscopic Metal–Organic Frameworks via EDTA-Mediated Structural Reinforcement and Photothermal Modification. Adv Funct Mater 2025;35:2416241.
[70] Yin X, Ai F, Han L. Recent Development of MOF-Based Photothermal Agent for Tumor Ablation. Front Chem 2022;10.
[71] Liu L, Zhang H, Peng L, Wang D, Zhang Y, Yan B, et al. A copper-metal organic framework enhances the photothermal and chemodynamic properties of polydopamine for melanoma therapy. Acta Biomater 2023;158:660–72.
[72] Wang Y, Yu R. Investigation of the catalytic effect of defective Ni-MOF-74 on polymerization of dopamine and multi-pore polydopamine photothermal coating constructed with defective Ni-MOF-74 particles. J Environ Chem Eng 2023;11:110422.
[73] Wang D, Wu H, Zhou J, Xu P, Wang C, Shi R, et al. In Situ One-Pot Synthesis of MOF–Polydopamine Hybrid Nanogels with Enhanced Photothermal effect for Targeted Cancer Therapy. Adv Sci 2018;5:1800287.
[74] Wang P, Zhang J, Zhan M, Tan Z, Wang C, Liu B, et al. Dual-Functional Amino-MOF with Enhanced Ice suppression and Intrinsic Photothermal activity for High-Performance Oocyte Cryopreservation. ACS Appl Bio Mater 2025;8:4383–94.
[75] Espín J, Garzón-Tovar L, Boix G, Imaz I, Maspoch D. The photothermal effect in MOFs: covalent post-synthetic modification of MOFs mediated by UV-Vis light under solvent-free conditions. Chem Commun 2018;54:4184–7.
[76] Su J, Jing P, Jiang K, Du J. *Recent advances in porous MOFs and their hybrids for photothermal cancer therapy*. Recent advances in porous MOFs and their hybrids for photothermal cancer therapy 2022;51:8938–44.
[77] Tong P-H, Yang J-J, Zhou Y-F, Tang Y-F, Tang M-T, Zang Y, et al. Metal-organic frameworks (MOFs) for phototherapy and synergistic phototherapy of cancer. Coord Chem Rev 2025;526:216381.
[78] Connolly BM, Aragones-Anglada M, Gandara-Loe J, Danaf NA, Lamb DC, Mehta JP, et al. Tuning porosity in macroscopic monolithic metal-organic frameworks for exceptional natural gas storage. Nat Commun 2019;10.
[79] Toncón-Leal CF, Villarroel-Rocha J, Silva MTP, Braga TP, Sapag K. Characterization of mesoporous region by the scanning of the hysteresis loop in adsorption–desorption isotherms. Adsorption 2021;27:109–1122.
[80] Rutherford SW. Simple Model for Hydrophilic, Hydrophobic, and Angstrofluidic Features of Water Confined in Micropores: Effects of Pore size and Surface Functionality on Mapping of Equilibrium Isotherm Types. Langmuir 2025;41:20502–15.
[81] Shi L, Kirlikovali KO, Chen Z, Farha OK. Metal-organic frameworks for water vapor adsorption. Chem 2024;10:484–503.
[82] Zhang S, Fu J, Xing G, Zhu W, Ben T. Porous Materials for Atmospheric Water Harvesting. ChemistryOpen 2023;12:e202300046.
[83] Zhou X, Lu H, Zhao F, Yu G. Atmospheric Water Harvesting: a Review of Material and Structural designs. ACS Mater Lett 2020;2:671–84.
[84] Bilal M, Sultan M, Morosuk T, Den W, Sajjad U, Aslam MM, et al. Adsorption-based atmospheric water harvesting: a review of adsorbents and systems. Int Commun Heat Mass Transfer 2022;133:105961.
[85] LaPotin A, Kim H, Rao SR, Wang EN. Adsorption-based Atmospheric Water Harvesting: Impact of Material and Component Properties on System-Level Performance. Acc Chem Res 2019;52:1588–97.
[86] Solovyeva MV, Shkatulov AI, Gordeeva LG, Fedorova EA, Krieger TA, Aristov YI. Water Vapor Adsorption on CAU-10-X: effect of Functional groups on Adsorption Equilibrium and Mechanisms. Langmuir 2021;37:93–702.
[87] Canivet J, Fateeva A, Guo Y, Coasnecd B, Farrusseng D. Water adsorption in MOFs: fundamentals and applications. Chem Soc Rev 2014;43:5594–617.
[88] Rosi NL, Kim J, Eddaoudi M, Chen B, O'Keeffe M, Yaghi OM. Rod Packings and Metal−Organic Frameworks Constructed from Rod-shaped Secondary Building units. J Am Chem Soc 2005;127:1504–18.
[89] Kirchon A, Feng L, Drake HF, Josepha EA, Zhou H-C. From fundamentals to applications: a toolbox for robust and multifunctional MOF materials. Chem Soc Rev 2018;47:8611–38.
[90] Platero-Prats AE, Mavrandonakis A, Gallington LC, Liu Y, Hupp JT, Farha OK, et al. Structural Transitions of the Metal-Oxide Nodes within Metal–Organic Frameworks: on the Local Structures of NU-1000 and UiO-66. J Am Chem Soc 2016;138:4178–85.
[91] Furukawa H, Gándara F, Zhang Y-B, Jiang J, Queen WL, Hudson MR, et al. Water Adsorption in Porous Metal–Organic Frameworks and Related Materials. J Am Chem Soc 2014;136:4369–81.
[92] Rieth AJ, Yang S, Wang EN, Dincă M. Record Atmospheric Fresh Water Capture and Heat transfer with a Material Operating at the Water Uptake Reversibility Limit. ACS Cent Sci 2017;3:668–72.

[93] Reinsch H, M. A. v. d. Veen, B. Gil, B. Marszalek, T. Verbies, D. d. Vos and N. Stock. Structures, Sorption Characteristics, and Nonlinear Optical Properties of a New Series of Highly Stable Aluminum MOFs. Chem Mater 2013;25:17–26.
[94] Hanikel N, Pei X, Chheda S, Lyu H, Jeong W, Sauer J, et al. Evolution of water structures in metal-organic frameworks for improved atmospheric water harvesting. Science 2021;374:454–9.
[95] Borges DD, Maurin G, Galvão DS. Design of Porous Metal-Organic Frameworks for Adsorption Driven thermal Batteries. MRS Adv 2017;2:519–24.
[96] Hanikel N, Prévot MS, Fathieh F, Kapustin EA, Lyu H, Wang H, et al. Rapid Cycling and Exceptional Yield in a Metal-Organic Framework Water Harvester. ACS Cent Sci 2019;5:1699–706.
[97] Ambroz F, Macdonald TJ, Martis V, Parkin IP. Evaluation of the BET Theory for the Characterization of Meso and Microporous MOFs. Small Methods 2018;2:1800173.
[98] Füredi M, Manzano CV, Marton A, Fodor B, Alvarez-Fernandez A, Guldin S. Beyond the Meso/Macroporous Boundary: Extending Capillary Condensation-based Pore size Characterization in Thin Films through Tailored Adsorptives. The Journal of Physical Chemistry Letters 2024;15:1420–7.
[99] Yanagita K, Hwang J, Shamim JA, Hsu W-L, Matsuda R, Delaunay A-E-J, et al. Kinetics of Water Vapor Adsorption and Desorption in MIL-101 Metal–Organic Frameworks. J Phys Chem C 2019;123:387–98.
[100] Salles F, Bourrelly S, Jobic H, Devic T, Guillerm V, Llewellyn P, et al. Molecular Insight into the Adsorption and Diffusion of Water in the Versatile Hydrophilic/Hydrophobic Flexible MIL-53(Cr) MOF. J Phys Chem C 2011;115:10764–76.
[101] Abtab SMT, Alezi D, Bhatt PM, Shkurenko A, Belmabkhout Y, Aggarwal H, et al. Reticular Chemistry in Action: a Hydrolytically Stable MOF Capturing twice its Weight in Adsorbed Water. Chem 2018;4:94–105.
[102] Zheng X, Li Z, Wu Y, Liu Y, Wu Z, Zhang P. Regulating the hydrophilicity of metal–organic framework CAU-1 with mild thermal treatment strategy for improved atmospheric water harvesting. Chem Eng J 2024;483:148920.
[103] Ko N, Choi PG, Hong J, Yeo M, Sung S, Cordova KE, et al. Tailoring the water adsorption properties of MIL-101 metal–organic frameworks by partial functionalization. J Mater Chem A 2015;3:2057–64.
[104] Chen Z, Li P, Zhang X, Li P, Wasson MC, Islamoglu T, et al. Reticular Access to Highly Porous acs-MOFs with rigid Trigonal Prismatic Linkers for Water Sorption. J Am Chem Soc 2019;141:2900–5.
[105] Ibrahim Y, Mahmood F, Sinopoli A, Moursi A, Mahmoud KA, Al-Ansari T. Advancements of metal-organic frameworks for atmospheric water harvesting and climate control. J Water Process Eng 2024;67:106249.
[106] Yang L, Idrees KB, Chen Z, Knapp J, Chen Y, Wang X, et al. Nanoporous Water-Stable Zr-based Metal–Organic Frameworks for Water Adsorption. ACS Appl Nano Mater 2021;4:4346–50.
[107] Gong W, Xie H, Idrees KB, Son FA, Chen Z, Sha F, et al. Water Sorption Evolution Enabled by Reticular Construction of Zirconium Metal–Organic Frameworks based on a Unique [2.2]Paracyclophane Scaffold. J Am Chem Soc 2022;144:1826–34.
[108] An Y, Lv X, Jiang W, Wang L, Shi Y, Hang X, et al. The stability of MOFs in aqueous solutions—research progress and prospects. Green Chem Eng 2024;5:187–204.
[109] Hu Y, Fang Z, Wan X, Ma X, Wang S, Fan S, et al. Carbon nanotubes decorated hollow metal–organic frameworks for efficient solar-driven atmospheric water harvesting. Chem Eng J 2022;430:133086.
[110] Shigematsu A, Yamada T, Kitagawa H. Wide Control of Proton Conductivity in Porous Coordination Polymers. J Am Chem Soc 2011;133:2034–6.
[111] Shan H, Poredoš P, Chen Z, Yang X, Ye Z, Hu Z, et al. Hygroscopic salt-embedded composite materials for sorption-based atmospheric water harvesting. Nat Rev Mater 2024;9:699–721.
[112] X. wang, c. xu, s. li and z. guo. An atmospheric water collection system by a hygroscopic process. Surf Interfaces 2024;46:103891.
[113] Xu J, Li T, Yan T, Wu S, Wu M, Chao J, et al. Ultrahigh solar-driven atmospheric water production enabled by scalable rapid-cycling water harvester with vertically aligned nanocomposite sorbent. Energ Environ Sci 2021;14:5979–94.
[114] Li T, Yan T, Wang P, Xu J, Huo X, Bai Z, et al. Scalable and efficient solar-driven atmospheric water harvesting enabled by bidirectionally aligned and hierarchically structured nanocomposites. Nat Water 2023;1:971–81.
[115] Xu J, Li T, Chao J, Wu S, Yan T, Li W, et al. Efficient Solar-Driven Water Harvesting from Arid Air with Metal–Organic Frameworks Modified by Hygroscopic Salt. Angew Chem Int Ed 2020;59:5202–10.
[116] Tian G, Fua C, Guo Z. A novel hygroscopic salt-modified MOF-303 with efficient solar-driven water harvesting from arid air. Nanoscale 2025;17:12340–9.
[117] An H, Chen Y, Wang Y, Liu X, Ren Y, Kang Z, et al. High-performance solar-driven water harvesting from air with a cheap and scalable hygroscopic salt modified metal–organic framework. Chem Eng J 2023;461:141955.
[118] Hu Y, Fang Z, Ma X, Wan X, Wang S, Fan S, et al. CaCl2 Nanocrystals decorated photothermal Fe-ferrocene MOFs hollow microspheres for atmospheric water harvesting. Appl Mater Today 2021;23:101076.
[119] Hu Y, Wang Y, Fang Z, Yao B, Ye Z, Peng X. Ca-MOF-Derived Porous Sorbents for High-Yield Solar-Driven Atmosphere Water Harvesting. ACS Appl Mater Interfaces 2023;15:44942–52.
[120] Li Y, Li J, Yin S, Shan X, Tao B, Wang S. Preparation of CaCl2/MOF-303 composite and its dehumidification properties. RSC Adv 2025;15:8867–75.
[121] Huang X, Qin Q, Ma Q, Wang B. Atmospheric Water Harvesting with Metal-Organic Frameworks and their Composites: from Materials to Devices. Water 2022;14:3487.
[122] Zhang W, Cheng L, Wang X, Zhang J, Wang X, Wang Z. Advances in Adsorptive Atmospheric Water Harvesting Technology: Materials, Desorption, and Systems. Sustainability 2025;17:10309.
[123] Hu Y, Wang Y, Fang Z, Wan X, Dong M, Yeab Z, et al. MOF supraparticles for atmosphere water harvesting at low humidity. J Mater Chem A 2022;10:15116–26.
[124] Luo F, Liao T, Liang X, Chen W, Wang S, Gao X, et al. Two-linker MOFs-based glass fiber paper monolithic adsorbent for atmospheric water harvesting in arid climates. J Clean Prod 2022;373:133838.
[125] Yilmaz G, Meng FL, Lu W, Abed J, Peh CKN, Gao M, et al. Autonomous atmospheric water seeping MOF matrix. Sci Adv 2020;6.
[126] Yan J, Li W, Yu Y, Huang G, Peng J, Lv D, et al. A Polyzwitterionic@MOF Hydrogel with Exceptionally High Water Vapor Uptake for Efficient Atmospheric Water Harvesting. Molecules 2024;29.
[127] Wu Q, Su W, Li Q, Tao Y, Li H. Enabling Continuous and improved Solar-Driven Atmospheric Water Harvesting with Ti3C2-Incorporated Metal–Organic Framework Monoliths. ACS Appl Mater Interfaces 2021;13:38906–15.
[128] He Y, Fu T, Wang L, Liu J, Liu G, Zhao H. Self-assembly of MOF-801 into robust hierarchically porous monoliths for scale-up atmospheric water harvesting. Chem Eng J 2023;472:144786.
[129] Reinsch H, Marszałek B, Wack J, Senker J, Gilb B, Stock N. A new Al-MOF based on a unique column-shaped inorganic building unit exhibiting strongly hydrophilic sorption behaviour. Chem Commun 2012;48:9486–8.
[130] Cadiau A, Lee JS, Borges DD, Fabry P, Devic T, Wharmby MT, et al. Design of Hydrophilic Metal Organic Framework Water Adsorbents for Heat Reallocation. Adv Mater 2015;27:4775–80.
[131] Khutia A, Rammelberg HU, Schmidt T, Henninger S, Janiak C. Water Sorption Cycle Measurements on Functionalized MIL-101Cr for Heat Transformation Application. Chem Mater 2013;25:790–8.
[132] Cmarik GE, Kim M, Cohen SM, Walton KS. Tuning the Adsorption Properties of UiO-66 via Ligand Functionalization. Langmuir 2012;28:15606–13.
[133] Li B, Lu F-F, Gu X-W, Shao K, Wu E, Qian G. Immobilization of Lewis Basic Nitrogen Sites into a Chemically Stable Metal–Organic Framework for Benchmark Water-Sorption-Driven Heat Allocations. Adv Sci 2022;9:2105556.
[134] Song Y, Xu N, Liu G, Qi H, Zhao W, Zhu B, et al. High-yield solar-driven atmospheric water harvesting of metal–organic-framework-derived nanoporous carbon with fast-diffusion water channels. Nat Nanotechnol 2022;17:857–63.
[135] Bai S, Chao L, Pan A, Ho T, Lin K, Tso C. Study of the relative humidity effects on the water condensation performance of adsorption-based atmospheric water harvesting using passive radiative condensers. Appl Therm Eng 2024;244:122702.

[136] Yang K, Pan T, Lei Q, Dong X, Cheng Q, Han Y. A Roadmap to Sorption-based Atmospheric Water Harvesting: from Molecular Sorption Mechanism to Sorbent Design and System Optimization. Environ Sci Technol 2021;55:6542–60.
[137] Banerjee G, Sengupta K. Pore size optimisation of humidity sensor—a probabilistic approach. Sens Actuators B 2002;86:34–41.
[138] Meng Y, Dang Y, Suib SL. Materials and devices for atmospheric water harvesting. Cell Rep Phys Sci 2022;3:100976.
[139] Kulkarni K, Madanan U, Mittal R, Goldstein R. Experimental validation of heat/mass transfer analogy for two-dimensional laminar and turbulent boundary layers. Int J Heat Mass Transf 2017;113:84–95.
[140] Tu YD, Wang RZ, Ge TS, Zheng X. Comfortable, high-efficiency heat pump with desiccant-coated, water-sorbing heat exchangers. Sci Rep 2017;7.
[141] Terzis A, Ramachandran A, Wang K, Asheghi M, Goodson KE, Santiago JG. High-Frequency Water Vapor Sorption Cycling using Fluidization of Metal-Organic Frameworks. Cell Rep Phys Sci 2020;1:100057.
[142] Sun C, Zhu Y, Shao P, Chen L, Huang X, Zhao S, et al. 2D Covalent Organic Framework for Water Harvesting with Fast Kinetics and Low Regeneration Temperature. Angew Chem Int Ed 2023;62:e202217103.
[143] Feyereisen MW, Feller D, Dixon DA. Hydrogen Bond Energy of the Water Dimer. J Phys Chem 1996;100:2993–7.
[144] Zhang Z, Li X, Yin J, Xu Y, Fei W, Xue M, et al. Emerging hydrovoltaic technology. Nat Nanotechnol 2018;13:1109–19.
[145] Simiao Guo YH, Fang Z, Yao B, Peng X. LiCl in situ decorated metal–organic framework (MOF)-derived porous carbon for efficient solar-driven atmospheric water harvesting. RSC Adv 2024;14:15619–26.
[146] Banala ST, A. TR, Saravanan S, S. V.S., Kalpathy SK, Thomas T. Oxide-coated Al-Cu-based nanoparticles for enhanced solar water heating. Nano-Struct Nano-Objects 2024;40:101361.
[147] Lyu P, Espinoza R, Nguyen SC. Photocatalysis of Metallic Nanoparticles: Interband vs Intraband Induced Mechanisms. J Phys Chem C 2023;127:15685–98.
[148] Gao M, Zhu L, Peh CK, Ho GW. Solar absorber material and system designs for photothermal water vaporization towards clean water and energy production. Energ Environ Sci 2019;12:841–64.
[149] Seh ZW, Liu S, Low M, Zhang S-Y, Liu Z, Mlayah A, et al. Janus Au-TiO2 Photocatalysts with strong Localization of Plasmonic Near-Fields for Efficient Visible-Light Hydrogen Generation. Adv Mater 2012;24:2310–4.
[150] Brongersma ML, Halas NJ, Nordlander P. Plasmon-induced hot carrier science and technology. Nat Nanotechnol 2015;10:25–34.
[151] Wu JZ, Ghopry SA, Liu B, Shultz A. Metallic and Non-Metallic Plasmonic Nanostructures for LSPR Sensors. Micromachines 2023;14.
[152] Sun J, Pang K, Liu T-F, Song J, Cao R. Near-infrared photothermal performance of a metal–organic framework-based composite. Dalton Trans 2021;50:17499–505.
[153] Linic S, Aslam U, Boerigter C, Morabito M. Photochemical transformations on plasmonic metal nanoparticles. Nat Mater 2015;14:567–76.
[154] From Energy to Health. D. J. d. Aberasturi, A. B. Serrano-Montes and L. M. Liz-Marzán. Modern applications of Plasmonic Nanoparticles. Adv Opt Mater 2015;3:602–17.
[155] Baffou G, Quidant R, F. J. G. d. Abajo. Nanoscale Control of Optical heating in complex Plasmonic Systems. ACS Nano 2010;4:709–16.
[156] Ye M, Jia J, Wu Z, Qian C, Chen R, O'Brien PG, et al. Synthesis of Black TiOx Nanoparticles by Mg Reduction of TiO2 Nanocrystals and their Application for Solar Water Evaporation. Adv Energy Mater 2017;7:1601811.
[157] Almond DP, Patel PM. Photothermal Science and Techniques. London: Springer; 1996.
[158] Bricker WP, Shenai PM, Ghosh A, Liu Z, Enriquez MGM, Lambrev PH, et al. Non-radiative relaxation of photoexcited chlorophylls: theoretical and experimental study. Sci Rep 2015;5.
[159] Wu R, Wang S, Zhou Y, Long J, Dong F, Zhang W. Chromium-based Metal–Organic Framework MIL-101 decorated with CdS Quantum Dots for the Photocatalytic Synthesis of Imines. ACS Appl Nano Mater 2019;2:6818–27.
[160] Wang F, Huang Y, Chai Z, Zeng M, Li Q, Wanga Y, et al. Photothermal-enhanced catalysis in core–shell plasmonic hierarchical Cu7S4 microsphere@zeolitic imidazole framework-8. Chem Sci 2016;7:6887–93.
[161] Hui R, O'Sullivan M. Fundamentals of Optical Devices. in *Fiber Optic Measurement Techniques*. Elsevier 2009:1–128.
[162] Li J, Wang L, Zhang C, Wang H, Pan Y, Li S, et al. Manipulation of the Self-Assembly Morphology by Side-Chain Engineering of Quinoxaline-Substituted Organic Photothermal Molecules for Highly Efficient Solar-thermal Conversion and applications. Angew Chem Int Ed 2024;63:e202402726.
[163] Cui X, Ruan Q, Zhuo X, Xia X, Hu J, Fu R, et al. Photothermal Nanomaterials: a Powerful Light-to-Heat Converter. Chem Rev 2023;123:6891–952.
[164] Marsili E, Prlj A, Curchod BFE. A Theoretical Perspective on the Actinic Photochemistry of 2-Hydroperoxypropanal. Chem A Eur J 2022;126:5420–33.
[165] Kass SR. π–Bond Dissociation Energies: C–C, C–N, and C–O. J Org Chem 2024;89:15158–63.
[166] Mathew RJ, Chandran AR, Kishor KSS, Linsa KSM, Saji KJ, Sajeev US. The role of graphene nanoplatelets doping in the defect induced saturable absorption in polyaniline films. Next Materials 2025;8:100662.
[167] Vasconcelos VMR, Postacchini BB, H. S. d. Santosc, F. F. M. Cajazeirasc, V. N. Freire, C. A. Juniorf, C. Pessoae, R. F. d. Costa, I. F. Vasconcelos and E. M. Bezerra. Red-shifted optical absorption induced by donor–acceptor–donor π-extended dibenzalacetone derivatives. RSC Adv 2025;15:2416–29.
[168] Vélez-Cordero JR, Hernández-Cordero J. Heat generation and conduction in PDMS-carbon nanoparticle membranes irradiated with optical fibers. Int J Therm Sci 2015;96:12–22.
[169] Lu G, Huang X, Li Y, Zhao G, Pang G, Wang G. Covalently integrated core-shell MOF@COF hybrids as efficient visible-light-driven photocatalysts for selective oxidation of alcohols. Journal of Energy Chemistry 2020;43:8–15.
[170] L. Wang and J. Yu. Principles of photocatalysis. in *Interface Science and Technology*, 35, 2023, pp. 1-52.
[171] Armghan A, Logeshwaran J, K. A. S. Raja c, M. Alsharari and S. K. Patel. Performance optimization of energy-efficient solar absorbers for thermal energy harvesting in modern industrial environments using a solar deep learning model. Heliyon 2024;10:e26371.
[172] Webba JA, Bardhan R. Emerging advances in nanomedicine with engineered gold nanostructures. Nanoscale 2014;6:2502–30.
[173] Ringe E, Langille MR, Sohn K, Zhang J, Huang J, Mirkin CA, et al. Plasmon Length: a Universal Parameter to Describe size Effects in Gold Nanoparticles. The Journal of Physical Chemistry Letters 2012;3:1479–83.
[174] sensing materials and applications. S. H. Cho, e. Choi, J. M. Suh and H. W. Jang. Advancements in surface plasmon resonance sensors for real-time detection of chemical analytes. J Mater Chem C 2025;13:6484–507.
[175] Zhu H, Chen X, Zheng Z, Ke X, Jaatinen E, Zhao J, et al. Mechanism of supported gold nanoparticles as photocatalysts under ultraviolet and visible light irradiation. Chem Commun 2009:7524–6.
[176] Attia YA, Buceta D, Requejo FG, Giovanettid LJ, López-Quintela MA. Photostability of gold nanoparticles with different shapes: the role of Ag clusters. Nanoscale 2015;7:11273–9.
[177] Kim HS, Lee DY. Near-Infrared-Responsive Cancer Photothermal and Photodynamic Therapy using Gold Nanoparticles. Polymers 2018;10.
[178] Chan GH, Zhao J, Schatz GC, Duyne RPV. Localized Surface Plasmon Resonance Spectroscopy of Triangular Aluminum Nanoparticles. J Phys Chem C 2008;112:13958–63.
[179] Ross MB, Blaber MG, Schatz GC. Using nanoscale and mesoscale anisotropy to engineer the optical response of three-dimensional plasmonic metamaterials. Nat Commun 2014;5.
[180] Yuan H, Khoury CG, Hwang H, Wilson CM, Grant GA, Vo-Dinh T. Gold nanostars: surfactant-free synthesis, 3D modelling, and two-photon photoluminescence imaging. Nanotechnology 2012;32.
[181] Zhang L, Jing H, Boisvert G, He JZ, Wang H. Geometry Control and Optical Tunability of Metal–Cuprous Oxide Core–Shell Nanoparticles. ACS Nano 2012;6:3514–27.
[182] Siahpoush V, Ahmadi-kandjani S, Nikniazi A. Effect of plasmonic coupling on photothermal behavior of random nanoparticles. Opt Commun 2018;420:52–8.
[183] Hubenthal F. Ultrafast dephasing time of localized surface plasmon polariton resonance and the involved damping mechanisms in colloidal gold nanoparticles. Prog Surf Sci 2007;82:378–87.
[184] Ye S, Benz F, Wheeler MC, Oram J, Baumberg JJ, Cespedes O, et al. One-step fabrication of hollow-channel gold nanoflowers with excellent catalytic performance and large single-particle SERS activity. Nanoscale 2016;8:14932–42.

[185] Sun Z-X, Sun K, Gao M-L, Metin Ö, Jiang H-L. Optimizing Pt Electronic States through Formation of a Schottky Junction on Non-reducible Metal–Organic Frameworks for Enhanced Photocatalysis. Angew Chem Int Ed 2022;61:e202206108.
[186] Wang J, Zhang HZ, Li RS, Huang CZ. Localized surface plasmon resonance of gold nanorods and assemblies in the view of biomedical analysis. TrAC Trends Anal Chem 2016;80:429–43.
[187] Zhang L, Chen H, Wang J, Li YF, Wang J, Sang Y, et al. Tetrakis(4-sulfonatophenyl)porphyrin-Directed Assembly of Gold Nanocrystals: Tailoring the Plasmon Coupling through Controllable Gap Distances. Small 2010;6:2001–9.
[188] Dong Y, Song R, Zhang Z, Han X, Wang B, Tao S, et al. Advances in photothermal CO2 hydrogenation catalysis for C1 molecules. Cell Rep Phys Sci 2024;5:102227.
[189] Bajpai M, Srivastava R, Dhar R, Tiwari RS. Review on Optical and Electrical Properties of Conducting Polymers. Indian Journal of Materials Science 2016.
[190] Yassin JM, Taddesse AM, Sánchez-Sánchez M. Novel UiO-66(Ce)/CdS/g-C3N4 Ternary Nanocomposite with Boosted Photoactivity in the Degradation of the dye Rhodamine B. Surf Interfaces 2025.
[191] Lia J, Wu N. Semiconductor-based photocatalysts and photoelectrochemical cells for solar fuel generation: a review. Cat Sci Technol 2015;5:1360–84.
[192] Ding D, Huang W, Song C, Yan M, Guo C, Liu S. Non-stoichiometric MoO3−x quantum dots as a light-harvesting material for interfacial water evaporation. Chem Commun 2017;53:6744–7.
[193] Ovando-Medina VM, Escobar-Villanueva AG, Martínez-Gutiérrez H, González-Ortega O. Interfacial photothermal water evaporator based on nanoporous microwave-expanded graphite and coconut waste fibers@recycled polystyrene as substrate. Int J Energy Res 2020:1–16.
[194] Liu G, Xu J, Wang K. Solar water evaporation by black photothermal sheets. Nano Energy 2017;41:269–84.
[195] Zhu L, Gao M, Peha CKN, Ho GW. Solar-driven photothermal nanostructured materials designs and prerequisites for evaporation and catalysis applications. Mater Horiz 2018;5:323–43.
[196] Zielinski MS, Choi J-W, Grange TL, Modestino M, Hashemi SMH, Pu Y, et al. Hollow Mesoporous Plasmonic Nanoshells for Enhanced Solar Vapor Generation. Nano Lett 2016;16:2159–67.
[197] Ansari AS, Azzahra G, Nugroho FG, Mujtaba MM, Ahmed ATA. Oxides and Metal Oxide/Carbon Hybrid Materials for Efficient Photocatalytic Organic Pollutant Removal. Catalysts 2025;15.
[198] Zhou L, Tan Y, Ji D, Zhu B, Zhang P, Xu J, et al. Self-assembly of highly efficient, broadband plasmonic absorbers for solar steam generation. Sci Adv 2016;2.
[199] Wang L, Li S-R, Chen Y-Z, Jiang H-L. Encapsulating Copper Nanocrystals into Metal–Organic Frameworks for Cascade Reactions by Photothermal Catalysis. Small 2021;17:2004481.
[200] Wu J, Sui Z, Du X, Zhang Y, Ma T. A Study on the Improvement of the Photothermal Characteristics of the Adsorbent for Sorption-based Atmospheric Water Harvesting Driven by Solar. Coatings 2023;13:154.
[201] Cao M, Wang Q-Y, Li R-M, Dai F, Wang S, Luo P, et al. A bis-aromatic MOF system constructed with a copper iodine cluster and porphyrinic ligand for enhancing near-infrared photothermal conversion. Inorg Chem Front 2024;11:7018–25.
[202] Liao J-Z, Zhu Z-C, Liu S-T, Ke H. Photothermal Conversion Perylene-based Metal–Organic Framework with Panchromatic Absorption Bandwidth across the Visible to Near-Infrared. Inorg Chem 2024;63:3327–34.
[203] Gao G, Luo S, Zhao Y, Zhang W, Li M, Cao Y, et al. A metal-organic framework with chemodynamic performance self-synergistic efficient near-infrared photothermal activities for in vivo antibacterial application. Chem Eng J 2024;500:157416.
[204] Lü B, Chen Y, Li P, Wang B, Müllen K, Yin M. Stable radical anions generated from a porous perylenediimide metal-organic framework for boosting near-infrared photothermal conversion. Nat Commun 2019;10.
[205] Qin J, Dou Y, Wu F, Yao Y, Andersen HR, Hélix-Nielsen C, et al. In-situ formation of Ag2O in metal-organic framework for light-driven upcycling of microplastics coupled with hydrogen production. Appl Catal B 2022;319:121940.
[206] Yang D, Yang G, Gai S, He F, An G, Dai Y, et al. Au25 cluster functionalized metal–organic nanostructures for magnetically targeted photodynamic/photothermal therapy triggered by single wavelength 808 nm near-infrared light. Nanoscale 2015;7:19568–78.
[207] Liu Z-Y, Zhang H, Ren X-Y, Luo H-B, Zhang J, Ren X-M. Functionalization of Cluster-Nodes in a Metal–Organic Framework for Light-Manipulating Proton Conduction. ACS Mater Lett 2024;6:461–5.
[208] Li R, Chen T, Lu J, Hu H, Zheng H, Zhu P, et al. Metal–organic frameworks doped with metal ions for efficient sterilization: Enhanced photocatalytic activity and photothermal effect. Water Res 2023;229:119366.
[209] Hou W, Chen C, Xie D, Xu Y. Substituted Ti(IV) in Ce-UiO-66-NH2 Metal–Organic Frameworks increases H2 and O2 Evolution under Visible Light. ACS Appl Mater Interfaces 2023;15:2911–21.
[210] Bhattacharyya A, Gutiérrez M, Cohen B, Szalad H, Albero J, Garcia H, et al. Unraveling the Optimal Cerium Content for Boosting the Photoresponse activity of Mixed-Metal Zr/Ce-based Metal–Organic Frameworks through a Photodynamic and Photocurrent Correlation: Implications on Water Splitting Efficiency. ACS Appl Mater Interfaces 2023;15:36434–46.
[211] Bhattacharyya A, Gutiérrez M, Cohen B, Valverde-González A, Iglesias M, Douhal A. How does the metal doping in mixed metal MOFs influence their photodynamics? a direct evidence for improved photocatalysts. Mater Today Energy 2022;29:101125.
[212] Xu C, Pan Y, Wan G, Liu H, Wang L, Zhou H, et al. Turning on Visible-Light Photocatalytic C−H Oxidation over Metal–Organic Frameworks by introducing Metal-to-Cluster Charge transfer. J Am Chem Soc 2019;141:19110–7.
[213] Khoo RSH, Fiankor C, Yang S, Hu W, Yang C, Lu J, et al. Postsynthetic Modification of the Nonanuclear Node in a Zirconium Metal–Organic Framework for Photocatalytic Oxidation of Hydrocarbons. J Am Chem Soc 2023;145:24052–60.
[214] Gutiérrez L, Mondal SS, Bucci A, Kandoth N, Escudero-Adán EC, Shafir A, et al. Crystal-to-Crystal Synthesis of Photocatalytic Metal–Organic Frameworks for Visible-Light Reductive Coupling and Mechanistic Investigations. ChemSusChem 2020;13:3418–28.
[215] Chen T, Zhao D. Post-synthetic modification of metal-organic framework-based membranes for enhanced molecular separations. Coord Chem Rev 2023;491:215259.
[216] Li H, Wang T, Chu H, Rokhum SL, Zhang Y, Yu H, et al. In–situ modification of UiO–66(Zr) organic ligand to synthesize highly recyclable solid acid for biodiesel production. Chem Eng Res Des 2024;205:713–21.
[217] Han D, Han Y, Li J, Liu X, Yeung KWK, Zheng Y, et al. Enhanced photocatalytic activity and photothermal effects of cu-doped metal-organic frameworks for rapid treatment of bacteria-infected wounds. Appl Catal B 2020;261:118248.
[218] Fu Y, Sun D, Chen Y, Huang R, Ding Z, Fu X, et al. An Amine-Functionalized Titanium Metal–Organic Framework Photocatalyst with Visible-Light-Induced activity for CO2 Reduction. Angew Chem Int Ed 2012;51:3364–7.
[219] Horiuchi Y, Toyao T, Saito M, Mochizuki K, Iwata M, Higashimura H, et al. Visible-Light-Promoted Photocatalytic Hydrogen Production by using an Amino-Functionalized Ti(IV) Metal–Organic Framework. J Phys Chem C 2012;116:20848–53.
[220] Sun D, Ye L, Li Z. Visible-light-assisted aerobic photocatalytic oxidation of amines to imines over NH2-MIL-125(Ti). Appl Catal B 2015;164:428–32.
[221] Huang H, Wang X-S, Philo D, Ichihara F, Song H, Li Y, et al. Toward visible-light-assisted photocatalytic nitrogen fixation: a titanium metal organic framework with functionalized ligands. Appl Catal B 2020;267:118686.
[222] Sun M, Yan S, Sun Y, Yang X, Guo Z, Du J, et al. Enhancement of visible-light-driven CO2 reduction performance using an amine-functionalized zirconium metal–organic framework. Dalton Trans 2018;47:909–15.
[223] Long J, Wang S, Ding Z, Wang S, Zhou Y, Huang L, et al. Amine-functionalized zirconium metal–organic framework as efficient visible-light photocatalyst for aerobic organic transformations. Chem Commun 2012;48:11656–8.
[224] Gomes Silva C, Luz I, F. X. Llabrés i Xamena, A. Corma and H. García. Water Stable Zr–Benzenedicarboxylate Metal–Organic Frameworks as Photocatalysts for Hydrogen Generation. *Chemistry – a.* European Journal 2010;16:11133–8.
[225] Shen L, Liang S, Wu W, Lianga R, Wu L. Multifunctional NH2-mediated zirconium metal–organic framework as an efficient visible-light-driven photocatalyst for selective oxidation of alcohols and reduction of aqueous Cr(vi). Dalton Trans 2013;42:13649–57.

[226] Wang D, Huang R, Liu W, Sun D, Li Z. Fe-based MOFs for Photocatalytic CO2 Reduction: Role of Coordination Unsaturated Sites and dual Excitation Pathways. ACS Catal 2014;4:4254–60.
[227] Wu Z, Huang X, Zheng H, Wang P, Hai G, Dong W, et al. Aromatic heterocycle-grafted NH2-MIL-125(Ti) via conjugated linker with enhanced photocatalytic activity for selective oxidation of alcohols under visible light. Appl Catal B 2018;224:479–87.
[228] Jin J-K, Wu K, Liu X-Y, Huang G-Q, Huang Y-L, Luo D, et al. Building a Pyrazole–Benzothiadiazole–Pyrazole Photosensitizer into Metal–Organic Frameworks for Photocatalytic Aerobic Oxidation. J Am Chem Soc 2021;143:21340–9.
[229] Xu W-J, Huang B-X, Li G, Yang F, Lin W, Gu J-X, et al. Donor–Acceptor Mixed-Naphthalene Diimide-Porphyrin MOF for Boosting Photocatalytic Oxidative Coupling of Amines. ACS Catal 2023;13:5723–32.
[230] Fiankor C, Nyakuchena J, Khoo RSH, Zhang X, Hu Y, Yang S, et al. Symmetry-Guided Synthesis of N,N′-Bicarbazole and Porphyrin-based Mixed-Ligand Metal–Organic Frameworks: Light Harvesting and Energy transfer. J Am Chem Soc 2021;143:20411–8.
[231] Yan T, Li Y-Y, Gu Q-Y, Li J, Su J, Wang H-Y, et al. A Tetrathiafulvalene/Naphthalene Diimide-Containing Metal–Organic Framework with fsc Topology for Highly Efficient Near-Infrared Photothermal Conversion. Inorg Chem 2022;61:3078–85.
[232] Wang X, Zhao C, Yang M, Baek J-H, Meng Z, Sun B, et al. Bioinspired Photothermal Metal-Organic Framework Cocrystal with Ultra-Fast Water Transporting Channels for Solar-Driven Interfacial Water Evaporation. Small 2025;21:2407665.
[233] Lü C-X, Zhan G-P, Chen K, Liu Z-K, Wu C-D. Anchoring Zn-phthalocyanines in the pore matrices of UiO-67 to improve highly the photocatalytic oxidation efficiency. Appl Catal B 2020;279:119350.
[234] Yang X, Liang T, Sun J, Zaworotko MJ, Chen Y, Cheng P, et al. Template-Directed Synthesis of Photocatalyst-Encapsulating Metal–Organic Frameworks with Boosted Photocatalytic activity. ACS Catal 2019;9:7486–93.
[235] Liu H, Li Q-Q, Zhou L, Deng B, Pan P-H, Zhao S-Y, et al. Confinement of Organic Dyes in UiO-66-Type Metal–Organic Frameworks for the Enhanced Synthesis of [1,2,5]Thiadiazole[3,4-g]benzoimidazoles. J Am Chem Soc 2023;145:17588–96.
[236] Sun D, Xu M, Jiang Y, Long J, Li Z. Small-Sized Bimetallic CuPd Nanoclusters Encapsulated inside Cavity of NH2-UiO-66(Zr) with Superior Performance for Light-Induced Suzuki Coupling Reaction. Small 2018;2:1800164.
[237] Sun D, Li Z. Double-Solvent Method to Pd Nanoclusters Encapsulated inside the Cavity of NH2–Uio-66(Zr) for Efficient Visible-Light-Promoted Suzuki Coupling Reaction. J Phys Chem C 2016;120:19744–50.
[238] Fang Z, Deng Z, Wan X, Li Z, Ma X, Hussain S, et al. Keggin-type polyoxometalates molecularly loaded in Zr-ferrocene metal organic framework nanosheets for solar-driven CO2 cycloaddition. Appl Catal B 2021;296:120329.
[239] Nazir A, Huo P, Wang H, Weiqiang Z, Wan Y. A review on plasmonic-based heterojunction photocatalysts for degradation of organic pollutants in wastewater. J Mater Sci 2023;58:6474–515.
[240] Hayat A, Rauf S, Alwan BA, Jery AE, Almuqati N, Melhi S, et al. Recent advance in MOFs and MOF-based composites: synthesis, properties, and applications. Mater Today Energy 2024;41:101542.
[241] Qi X-C, Lang F, Li C, Liu M-W, Wang Y-F, Pang J. Synergistic Effects of MOFs and Noble Metals in Photocatalytic Reactions: Mechanisms and applications. ChemPlusChem 2024;89:e202400158.
[242] Biswas A, Lemcoff N, Shelonchik O, Baranov M, Gordon G, Nun UB, et al. Molecular light-to-heat conversion promotes orthogonal synthesis and assembly of metal-organic frameworks. Nat Commun 2025;16.
[243] Zhu S, Huang C, Li X, Chen X, Ye H, Xue Z, et al. Enhanced photothermal conversion in 3D stacked metal–organic framework nanosheets. Aggregate 2024;5:e529.
[244] Liu X, He L, Zheng J, Guo J, Bi F, Ma X, et al. Solar-Light-Driven Renewable Butanol Separation by Core–Shell Ag@ZIF-8 Nanowires. Adv Mater 2015;27:3273–7.
[245] Li Y, Jin J, Wang D, Lv J, Hou K, Liu Y, et al. Coordination-responsive drug release inside gold nanorod@metal-organic framework core–shell nanostructures for near-infrared-induced synergistic chemo-photothermal therapy. Nano Res 2018;11:3294–305.
[246] Zhao C, Pan X, Wang Z, Wang C-C. $1 + 1 > 2$: a critical review of MOF/bismuth-based semiconductor composites for boosted photocatalysis. Chem Eng J 2021;417:128022.
[247] Ningab X, Lu G. Photocorrosion inhibition of CdS-based catalysts for photocatalytic overall water splitting. Nanoscale 2020;12:1213–23.
[248] Chu X, Sathish C, Yang J-H, Guan X, Zhang X, Qiao L, et al. Strategies for improving the Photocatalytic Hydrogen Evolution Reaction of Carbon Nitride-based Catalysts. Small 2023;19:2302875.
[249] Meng A, Teng Z, Zhang Q, Su C. Intrinsic Defects in Polymeric Carbon Nitride for Photocatalysis applications. Chemistry-An Asian Journal 2020;15:3405–15.
[250] Anus A, Park S. The synthesis and key features of 3D carbon nitrides (C3N4) used for CO2 photoreduction. Chem Eng J 2024;486:150213.
[251] Lee D-E, Danish M, Alam U, Jo W-K. Review on inorganic and polymeric materials-coordinated metal-organic-framework photocatalysts for green hydrogen evolution. Journal of Energy Chemistry 2024;92:322–56.
[252] Liu J, X. X. Qi Li a, F. Li, C. Zhao, Q. Sun, P. Qiao, J. Zhou, J. Wu, B. Li, H. Bao and B. Jiang. Metal-organic frameworks loaded on phosphorus-doped tubular carbon nitride for enhanced photocatalytic hydrogen production and amine oxidation. J Colloid Interface Sci 2021;590:1–11.
[253] Daliran S, Khajeh M, Oveisi AR, Albero J, García H. CsCu2I3 Nanoparticles Incorporated within a Mesoporous Metal–Organic Porphyrin Framework as a Catalyst for One-Pot Click Cycloaddition and Oxidation/Knoevenagel Tandem Reaction. ACS Appl Mater Interfaces 2022;14:36515–26.
[254] Yan C, Tian Q, Yang S. Recent advances in the rational design of copper chalcogenide to enhance the photothermal conversion efficiency for the photothermal ablation of cancer cells. RSC Adv 2017;7:37887–97.
[255] Gong Y-N, Guan X, Jiang H-L. Covalent organic frameworks for photocatalysis: Synthesis, structural features, fundamentals and performance. Coord Chem Rev 2023;475:214889.
[256] López-Magano A, Daliran S, Oveisi AR, Mas-Ballesté R, Dhakshinamoorthy A, Alemán J, et al. Recent advances in the use of Covalent Organic Frameworks as Heterogenous Photocatalysts in Organic Synthesis. Adv Mater 2023;35:2209475.
[257] Yang L, Wang J, Zhao K, Fang Z, Qiao H, Zhai L, et al. Photoactive Covalent Organic Frameworks for Catalyzing Organic Reactions. ChemPlusChem 2022;87:e202200281.
[258] Altintas C, Erucar I, Keskin S. MOF/COF hybrids as next generation materials for energy and biomedical applications. CrstEngComm 2022;24:7360–71.
[259] Yuan G, Tan L, Wang P, Wang Y, Wang C, Yan H, et al. MOF-COF Composite Photocatalysts: Design, Synthesis, and Mechanism. Cryst Growth Des 2022;22:893–908.
[260] Gao M-L, Qi M-H, Liu L, Han Z-B. An exceptionally stable core–shell MOF/COF bifunctional catalyst for a highly efficient cascade deacetalization–Knoevenagel condensation reaction. Chem Commun 2019;55:6377–80.
[261] Zhang M-Y, Li J-K, Wang R, Zhao S-N, Zang S-Q, Mak TCW. Construction of Core–Shell MOF@COF Hybrids with Controllable Morphology Adjustment of COF Shell as a Novel Platform for Photocatalytic Cascade Reactions. Adv Sci 2021;8:2101884.
[262] Peng Y, Zhao M, Chen B, Zhang Z, Huang Y, Dai F, et al. Hybridization of MOFs and COFs: a New Strategy for Construction of MOF@COF Core–Shell Hybrid Materials. Adv Mater 2018;30:1705454.
[263] Sun D, Jang S, Yim S-J, Ye L, Kim D-P. Metal Doped Core–Shell Metal-Organic Frameworks@Covalent Organic Frameworks (MOFs@COFs) Hybrids as a Novel Photocatalytic Platform. Adv Funct Mater 2018;28:1707110.
[264] Li T, Wu M, Xu J, Du R, Yan T, Wang P, et al. Simultaneous atmospheric water production and 24-hour power generation enabled by moisture-induced energy harvesting. Nat Commun 2022;13.
[265] Severino MI, Freitas C, Pimenta V, Nouar F, Pinto ML, Serre C. Cost Estimation of the production of MIL-100(Fe) at Industrial Scale from two Upscaled Sustainable Synthesis Routes. Ind Eng Chem Res 2025;64:2708–18.
[266] Zou M, Dong M, Zhao T. Advances in Metal-Organic Frameworks MIL-101(Cr). Int J Mol Sci 2022;23:9396.
[267] Qian Y, Fu H, Li L, Su W, Li J, Zhang Y. Efficient Removal of Azlocillin Sodium from Water by Polystyrene Anion Exchange Resin Supported MIL-53. Processes 2021;9:2195.

[268] Liu L, Chen Z, Wang J, Zhang D, Zhu Y, Ling S, et al. Imaging defects and their evolution in a metal–organic framework at sub-unit-cell resolution. Nat Chem 2019;11:622–8.
[269] Fathieh F, Kalmutzki MJ, Kapustin EA, Waller PJ, Yang J, Yaghi OM. Practical water production from desert air. Sci Adv 2018;4.
[270] Shao L, Meng F, Chen J, Fu Y. Epitaxial transformations of metal–organic frameworks into orientated superparticles. J Mater Chem A 2023;11:5027–36.
[271] Cho H-Y, Kim J, Kim S-N, Ahn W-S. High yield 1-L scale synthesis of ZIF-8 via a sonochemical route. Microporous Mesoporous Mater 2013;169:180–4.
[272] Liu J, Wang Y, Benin AI, Jakubczak P, Willis RR, LeVan MD. CO2/H2O Adsorption Equilibrium and rates on Metal−Organic Frameworks: HKUST-1 and Ni/DOBDC. Langmuir 2010;26:14301–7.
[273] Schoenecker PM, Carson CG, Jasuja H, Flemming CJJ, Walton KS. Effect of Water Adsorption on Retention of Structure and Surface Area of Metal–Organic Frameworks. Ind Eng Chem Res 2021;51:6513–9.
[274] Canivet J, Bonnefoy J, Daniel C, Legrand A, Coasnebc B, Farrusseng D. Structure–property relationships of water adsorption in metal–organic frameworks. New J Chem 2014;38:3102–11.
[275] Li S, Wu P, Chen L, Tang Y, Zhang Y, Qin L, et al. Enhanced atmospheric water harvesting (AWH) by Co-based MOF with abundant hydrophilic groups and open metal sites. J Water Process Eng 2024;58:104899.
[276] Jeremias F, Khutia A, Henninger SK, Janiak C. MIL-100(Al, Fe) as water adsorbents for heat transformation purposes—a promising application. J Mater Chem 2012;22:10148–51.
[277] Hanikel N, Kurandina D, Chheda S, Zheng Z, Rong Z, Neumann SE, et al. MOF Linker Extension Strategy for Enhanced Atmospheric Water Harvesting. ACS Cent Sci 2023;9:551–7.
[278] Low JJ, Benin AI, Jakubczak P, Abrahamian JF, Faheem SA, Willis RR. Virtual High Throughput Screening Confirmed Experimentally: Porous Coordination Polymer Hydration. J Am Chem Soc 2009;131:15834–42.
[279] DeCoste JB, Peterson GW, Jasuja H, Glover TG, Huang Y-G, Walton KS. Stability and degradation mechanisms of metal–organic frameworks containing the Zr6O4(OH)4 secondary building unit. J Mater Chem A 2013;1:5642–50.
[280] Burtch NC, Jasuja H, Walton KS. Water Stability and Adsorption in Metal–Organic Frameworks. Chem Rev 2014;114:10575–612.
[281] Clough TJ, Jiang L, Wong K-L, Long NJ. Ligand design strategies to increase stability of gadolinium-based magnetic resonance imaging contrast agents. Nat Commun 2019;10.
[282] Ferreira JC, Rabeh WM. Biochemical and biophysical characterization of the main protease, 3-chymotrypsin-like protease (3CLpro) from the novel coronavirus SARS-CoV 2. Sci Rep 2020;10.
[283] Wittmann T, Siegel R, Reimer N, Milius W, Stock N, Senker J. Enhancing the Water Stability of Al-MIL-101-NH2 via Postsynthetic Modification. Chemistry-A European Journal 2015;21:314–23.
[284] Rong S, Su P, Chen S, Jia M, Li W. Sub-5 nm porous polymer decoration toward superhydrophobic MOFs with enhanced stability and processability. Chin Chem Lett 2022;33:2134–8.
[285] Nguyen JG, Cohen SM. Moisture-Resistant and Superhydrophobic Metal−Organic Frameworks Obtained via Postsynthetic Modification. J Am Chem Soc 2010;132:4560–1.
[286] Ding N, Li H, Feng X, Wang Q, Wang S, Ma L, et al. Partitioning MOF-5 into Confined and Hydrophobic Compartments for Carbon Capture under Humid Conditions. J Am Chem Soc 2016;138:10100–3.
[287] Zhang W, Hu Y, Ge J, Jiang H-L, Yu S-H. A Facile and General Coating Approach to Moisture/Water-Resistant Metal–Organic Frameworks with Intact Porosity. J Am Chem Soc 2014;136:16978–81.
[288] Ding M, Jiang H-L. Improving Water Stability of Metal–Organic Frameworks by a General Surface Hydrophobic Polymerization. CCS Chem 2021;3:2740–8.
[289] DeCoste JB, Peterson GW, Schindler BJ, Killops KL, Broweb MA, Mahle JJ. The effect of water adsorption on the structure of the carboxylate containing metal–organic frameworks Cu-BTC, Mg-MOF-74, and UiO-66. J Mater Chem A 2013;1:11922–32.
[290] Li T, Chen D-L, Sullivan JE, Kozlowski MT, Johnsoncd JK, Rosi NL. Systematic modulation and enhancement of CO2 : N2 selectivity and water stability in an isoreticular series of bio-MOF-11 analogues. Chem Sci 2013;4:1746–55.
[291] Hungerford J, Bhattacharyya S, Tumuluri U, Nair S, Wu Z, Walton KS. DMOF-1 as a Representative MOF for SO2 Adsorption in both Humid and Dry Conditions. J Phys Chem C 2018;122:23493–500.
[292] Duan Z, Li Y, Xiao X, Huang X, Li X, Li Y, et al. Interpenetrated Metal–Organic Frameworks with ftw Topology and Versatile Functions. ACS Appl Mater Interfaces 2020;12:18715–22.
[293] Lei J, Zhang P, Xue Y-Y, Xu J, Li H-P, Lv H-J, et al. Design of ultra-stable Yttrium-organic framework adsorbents for efficient methane purification and storage. Sep Purif Technol 2022;283:120211.
[294] Liu L, Telfer SG. Systematic Ligand Modulation Enhances the Moisture Stability and Gas Sorption Characteristics of Quaternary Metal–Organic Frameworks. J Am Chem Soc 2015;137:3901–9.
[295] Lv X-L, Yuan S, Xie L-H, Darke HF, Chen Y, He T, et al. Ligand Rigidification for Enhancing the Stability of Metal–Organic Frameworks. J Am Chem Soc 2019;141:10283–93.
[296] Pearson RG. Hard and soft acids and bases, HSAB, part 1: fundamental principles. J Chem Educ 1968;45:581.
[297] Pearson RG. Hard and soft acids and bases, HSAB, part II: underlying theories. J Chem Educ 1968;45:643.
[298] Colombo V, Galli S, Choi HJ, Han GD, Maspero A, Palmisano G, et al. High thermal and chemical stability in pyrazolate-bridged metal–organic frameworks with exposed metal sites. Chem Sci 2011;2:1311–9.
[299] Xue J, Yang F, Jin J, Li Y, Wu D, Yang G-P, et al. Design and Synthesis of four newly Water-Stable Pb-based Heterometallic Organic Frameworks: how do the Second Metals (Zn, Cd, Co, and Mn) Optimize their Fluorescent and Catalytic Properties. Cryst Growth Des 2022;22:2628–36.
[300] Hilal SH, Karickhoff SW, Carreira LA. A Rigorous Test for SPARC's Chemical Reactivity Models: Estimation of more than 4300 Ionization pKas. Quant Struct-Act Relat 1995;14:348–55.
[301] Pan T, Yang K, Han Y. Recent Progress of Atmospheric Water Harvesting using Metal-Organic Frameworks. Chem Res Chin Univ 2020;36:33–40.
[302] Liu J, Benin AI, Furtado AMB, Jakubczak P, Willis RR, LeVan MD. Stability Effects on CO2 Adsorption for the DOBDC Series of Metal–Organic Frameworks. Langmuir 2011;27:11451–6.
[303] Kang IJ, Khan NA, Haque E, Jhung SH. Chemical and thermal Stability of Isotypic Metal–Organic Frameworks: effect of Metal Ions. Chemistry-A European Journal 2011;17:6437–42.
[304] Luo F, Liang X, Chen W, Wang S, Gao X, Zhang Z, et al. Bimetallic MOF-Derived Solar-Triggered Monolithic Adsorbent for Enhanced Atmospheric Water Harvesting. Small 2023;19:2304477.
[305] Yan J, Li W, Yu Y, Huang G, Peng J, Lv D, et al. A Polyzwitterionic@MOF Hydrogel with Exceptionally High Water Vapor Uptake for Efficient Atmospheric Water Harvesting. Molecules 2024;29:1851.
[306] Luo F, Liang X, Chen W, Wang S, Gao X, Zhang Z, et al. High-efficient and scalable solar-driven MOF-based water collection unit: from module design to concrete implementation. Chem Eng J 2023;465:142891.
[307] Chen W, Liu Y, Xu B, Ganesan M, Tan B, Tan Y, et al. A Functionally Asymmetric Janus Hygro-Photothermal Hybrid for Atmospheric Water Harvesting in Arid Regions. Small 2024;20:2306521.
[308] Chen W, Liu Y, Xu B, Cheng B, Ganesan M, Tan Y, et al. Enhancing Atmospheric Water Harvesting of MIL-101 (Cr) MOF Sorbent with Rapid Desorption Enabled by Ni—Ni3S2 Photothermal Bridge. Adv Funct Mater 2024;34:2410999.
[309] Liang Y, Wang S, Jia H, Yao Y, Song J, Yang W, et al. pH/redox/α-amylase triple responsive metal-organic framework composites for pest management and plant growth promotion. Microporous Mesoporous Mater 2022;344:112230.
[310] Mahmoud LAM, R. A. d. Reis, X. Chen, V. P. Ting and S. Nayak. Metal–Organic Frameworks as potential Agents for Extraction and delivery of Pesticides and Agrochemicals. ACS Omega 2022;7:45910–34.

[311] Matsumoto M, Kitaoka T. Ultraselective Gas Separation by Nanoporous Metal–Organic Frameworks embedded in Gas-Barrier Nanocellulose Films. Adv Mater 2016;28:1765–9.
[312] Ikigaki K, Okada K, Tokudome Y, Toyao T, Falcaro P, Doonan CJ, et al. MOF-on-MOF: Oriented growth of Multiple Layered Thin Films of Metal–Organic Frameworks. Angew Chem Int Ed 2019;58:6886–90.
[313] Rezaei F, Lawson S, Hosseini H, Thakkar H, Hajari A, Monjezi S, et al. MOF-74 and UTSA-16 film growth on monolithic structures and their CO2 adsorption performance. Chem Eng J 2017;313:1346–53.
[314] Jeremias F, Fröhlich D, Janiak C, Henninger SK. Advancement of sorption-based heat transformation by a metal coating of highly-stable, hydrophilic aluminium fumarate MOF. RSC Adv 2014;4:24073–82.
[315] Chaudhari AK, Tan J-C. A mechano-responsive supramolecular metal–organic framework (supraMOF) gel material rich in ZIF-8 nanoplates. Chem Commun 2017;53:8502–5.
[316] Tian T, Zeng Z, Vulpe D, Casco ME, Divitini G, Midgley PA, et al. A sol–gel monolithic metal–organic framework with enhanced methane uptake. Nat Mater 2018;17:174–9.
[317] Bueken B, Velthoven NV, Willhammar T, Stassin T, Stassen I, Keen DA, et al. Gel-based morphological design of zirconium metal–organic frameworks. Chem Sci 2017;8:3939–48.
[318] Lohe MR, Rosea M, Kaskel S. Metal–organic framework (MOF) aerogels with high micro- and macroporosity. Chem Commun 2009:6056–8.
[319] Ahmed A, Hasell T, Clowes R, Myers P, Coopera AI, Zhang H. Aligned macroporous monoliths with intrinsic microporosity via a frozen-solvent-templating approach. Chem Commun 2015;51:1717–20.
[320] Gu J, Fan H, Li C, Jürgen Caro HM. Robust Superhydrophobic/Superoleophilic Wrinkled Microspherical MOF@rGO Composites for Efficient Oil–Water Separation. Angew Chem Int Ed 2019;58:5297–301.
[321] Hindocha S, Poulston S. Study of the scale-up, formulation, ageing and ammonia adsorption capacity of MIL-100(Fe), Cu-BTC and CPO-27(Ni) for use in respiratory protection filters. Faraday Discuss 2017;201:113–25.
[322] Zacharia R, Cossement D, Lafia L, Chahine R. Volumetric hydrogen sorption capacity of monoliths prepared by mechanical densification of MOF-177. J Mater Chem 2010;20:2145–51.
[323] Ribeiro RP, Antunes CL, Garate AU, Portela AF, Plaza MG, Mota JP, et al. Binderless shaped metal-organic framework particles: Impact on carbon dioxide adsorption. Microporous Mesoporous Mater 2019;275:111–21.
[324] Bingre R, Louis B, Nguyen P. An Overview on Zeolite Shaping Technology and Solutions to Overcome Diffusion Limitations. Catalysts 2018;8:163.
[325] Valekar AH, Cho K-H, Lee U-H, Lee JS, Yoon JW, Hwang YK, et al. Shaping of porous metal–organic framework granules using mesoporous ρ-alumina as a binder. RSC Adv 2017;7:55767–77.
[326] Kim P-J, You Y-W, Park H, Chang J-S, Bae Y-S, Lee C-H, et al. Separation of SF6 from SF6/N2 mixture using metal–organic framework MIL-100(Fe) granule. Chem Eng J 2015;262:683–90.
[327] Moreira MA, Santos JC, Ferreira AFP, Loureiro JM, Ragon F, Horcajada P, et al. Reverse Shape Selectivity in the Liquid-phase Adsorption of Xylene Isomers in Zirconium Terephthalate MOF UiO-66. Langmuir 2012;28:5715–23.
[328] Wickenheisser M, Janiak C. Hierarchical embedding of micro-mesoporous MIL-101(Cr) in macroporous poly(2-hydroxyethyl methacrylate) high internal phase emulsions with monolithic shape for vapor adsorption applications. Microporous Mesoporous Mater 2015;204:242–50.
[329] Ren J, Musyoka NM, Langmi HW, Swartbooi A, North BC, Mathe M. A more efficient way to shape metal-organic framework (MOF) powder materials for hydrogen storage applications. Int J Hydrogen Energy 2015;40:4617–22.
[330] Wickenheisser M, Herbst A, Tannert R, Milow B, Janiak C. Hierarchical MOF-xerogel monolith composites from embedding MIL-100(Fe,Cr) and MIL-101(Cr) in resorcinol-formaldehyde xerogels for water adsorption applications. Microporous Mesoporous Mater 2015;215:143–53.
[331] Finsy V, Ma L, Alaerts L, Vos DD, Baron G, Denayer J. Separation of CO2/CH4 mixtures with the MIL-53(Al) metal-organic framework. Microporous Mesoporous Mater 2009;120:221–7.
[332] Kriesten M, Schmitz JV, Siegel J, Smith CE, Kaspereit M, Hartmann M. Shaping of Flexible Metal-Organic Frameworks: Combining Macroscopic Stability and Framework Flexibility. Eur J Inorg Chem 2019:4700–9.
[333] Zhu H, Zhang Q, Zhu S. Assembly of a Metal–Organic Framework into 3 D Hierarchical Porous Monoliths using a Pickering High Internal phase Emulsion Template. ChemEurJ 2016;22:8751–5.
[334] Fu Q, Wen L, Zhang L, Chen X, Pun D, Ahmed A, et al. Preparation of Ice-Templated MOF–Polymer Composite Monoliths and their Application for Wastewater Treatment with High Capacity and Easy Recycling. ACS Appl Mater Interfaces 2017;9:33979–88.
[335] Hastürk E, Höfert S-P, Topalli B, Schlüsener C, Janiak C. Shaping of MOFs via freeze-casting method with hydrophilic polymers and their effect on textural properties. Microporous Mesoporous Mater 2020;295:109907.
[336] Wang J, Qin J, Zhu H, Li B-G, Zhu S. Hierarchically Porous Monolith with High MOF Accessibility and Strengthened Mechanical Properties using Water-in-Oil High Internal phase Emulsion Template. Adv Mater Interfaces 2021;8:2100620.
[337] Hastürk E, Schlüsener C, Quodbach J, Schmitz A, Janiak C. Shaping of metal-organic frameworks into mechanically stable monoliths with poly(vinyl alcohol) by phase separation technique. Microporous Mesoporous Mater 2019;280:277–87.
[338] Chen Y, Huang X, Zhang S, Li S, Cao S, Pei X, et al. Shaping of Metal–Organic Frameworks: from Fluid to shaped Bodies and Robust Foams. J Am Chem Soc 2016;138:10810–3.
[339] Lawson S, Li X, Thakkar H, Rownaghi AA, Rezaei F. Recent advances in 3D Printing of Structured Materials for Adsorption and Catalysis applications. Chem Rev 2021;121:6246–91.
[340] Thakkar H, Eastman S, Al-Naddaf Q, Rownaghi AA, Rezaei F. 3D-printed Metal–Organic Framework Monoliths for Gas Adsorption Processes. ACS Appl Mater Interfaces 2017;9:35908–16.
[341] M. Bible, M. Sefa, J. A. Fedchak, J. Scherschligt, B. Natarajan, Z. Ahmed and M. R. Hartings. 3D-Printed Acrylonitrile Butadiene Styrene-Metal Organic Framework Composite Materials and Their Gas Storage Properties. *3D Printing and Additive Manufacturing*. 5, 2018.
[342] Liu X, Lim GJ, Wang Y, Zhang L, Mullangi D, Wu Y, et al. Binder-free 3D printing of covalent organic framework (COF) monoliths for CO2 adsorption. Chem Eng J 2021;403:126333.
[343] Franco M, Chairez TP, Poznyak A. BTEX decomposition by ozone in gaseous phase. J Environ Manage 2012;95:S55–60.
[344] Castro M, Kumar B, Feller J, Haddi Z, Amari A, Bouchikhi B. Novel e-nose for the discrimination of volatile organic biomarkers with an array of carbon nanotubes (CNT) conductive polymer nanocomposites (CPC) sensors. Sens Actuators B 2011;159:213–9.
[345] Wakeham SG, Canuel EA, Doering PH. Geochemistry of volatile organic compounds in seawater: Mesocosm experiments with 14C-model compounds. Geochim Cosmochim Acta 1986;50:1163–72.
[346] Feng A, Akther N, Duan X, Peng S, Onggowarsito C, Mao S, et al. Recent Development of Atmospheric Water Harvesting Materials: a Review. ACS Mater Au 2022;2:576–95.
[347] Parafati L, Vitale A, Restuccia C, Cirvilleri G. Performance evaluation of volatile organic compounds by antagonistic yeasts immobilized on hydrogel spheres against gray, green and blue postharvest decays. Food Microbiol 2017;63:191–8.
[348] Li H, Guo J, Ren J, Li Y, Yu X. Carbon nanodot-induced Eu3+-based fluorescent polymeric hydrogel for excellent phase-separation absorption of VOC. J Mater Chem A 2022;10:7941–7.
[349] Zeng C, Mojiri A, Ananpattarachai J, Farsad A, Westerhoff P. Sorption-based atmospheric water harvesting for continuous water production in the built environment: Assessment of water yield and quality. Water Res 2024;265:122227.
[350] Zhang N, Zhang J, Gao C, Yuan S, Wang Z. Emerging advanced membranes for removal of volatile organic compounds during membrane distillation. Desalination 2025;597:118372.
[351] Altalyan HN, Jones B, Bradd J, Nghiem LD, Alyazichi YM. Removal of volatile organic compounds (VOCs) from groundwater by reverse osmosis and nanofiltration. J Water Process Eng 2016;9:9–21.

[352] Ma X, Deng Z, Li Z, Chen D, Wan X, Wanga X, et al. A photothermal and Fenton active MOF-based membrane for high-efficiency solar water evaporation and clean water production. J Mater Chem A 2020;8:22728–35.
[353] Zhang H, Zhou Z, Du J, Pei X, Zhou L. Starch-derived photoresponsive high-efficientcy hygroscopic hydrogel for all-weather atmospheric water harvesting. J Clean Prod 2023;416:137897.
[354] Entezari A, Ejeian M, Wang R. Super Atmospheric Water Harvesting Hydrogel with Alginate Chains Modified with Binary Salts. ACS Mater Lett 2020;2:471–7.
[355] Lyu T, Han Y, Chen Z, Fan X, Tian Y. Hydrogels and hydrogel derivatives for atmospheric water harvesting. Mater Today Sustainability 2024;25:100693.
[356] Inbar O, Gozlan I, Ratner S, Aviv Y, Sirota R, Avisar D. Producing Safe Drinking Water using an Atmospheric Water Generator (AWG) in an Urban Environment. Water 2020;12:2940.
[357] Kaplan A, Ronen-Eliraz G, Ratner S, Aviv Y, Wolanov Y, Avisar D. Impact of industrial air pollution on the quality of atmospheric water production. Environ Pollut 2023;325:121447.
[358] Li Y, Yu J, Li Y, Shen J, Du M, Zhang X, et al. Nanoporous MOF-303 Performance for Atmospheric Water Harvesting in the Presence of Airborne Contaminants: GCMC and DFT Simulations. ACS Appl Nano Mater 2024;7:23850–9.
[359] Kim H, Rao SR, Kapustin EA, Zhao L, Yang S, Yaghi OM, et al. Adsorption-based atmospheric water harvesting device for arid climates. Nat Commun 2018;9.
[360] Xu J, Li T, Chao J, Si Wu TY, Li W, Cao B, et al. Efficient Solar-Driven Water Harvesting from Arid Air with Metal–Organic Frameworks Modified by Hygroscopic Salt. Angew Chem 2020;132:5240–8.
[361] Tao Y, Wu Q, Huang C, Su W, Ying Y, Zhu D, et al. Sandwich-Structured Carbon Paper/Metal–Organic Framework Monoliths for Flexible Solar-Powered Atmospheric Water Harvesting on demand. ACS Appl Mater Interfaces 2022;14:10966–75.
[362] Hu Y, Fang Z, Wan X, Ma X, Wang Y, Dong M, et al. Ferrocene Dicarboxylic Acid Ligand-Exchanged Hollow MIL-101(Cr) Nanospheres for Solar-Driven Atmospheric Water Harvesting. ACS Sustain Chem Eng 2022;10:6446–55.
[363] Li A, Xiong J, Liu Y, Wang L, Qin X, Yu J. A Rapid-Ab/Desorption and Portable Photothermal MIL-101(Cr) Nanofibrous Composite Membrane Fabricated by Spray-Electrospinning for Atmosphere Water Harvesting. ENERGY & ENVIRONMENTAL MATERIALS 2023;6:e12254.
[364] Tan Y, Chen W, Fang Y, Wang S. Sandwich-like adsorbent based on Al-fumarate MOF coating on Cu@CuxS sheet for rapid solar-driven atmospheric water harvesting. Chem Eng J 2023;475:146353.
[365] Kang MS, Heo I, Park SH, Bae J, Kim S, Kim G, et al. Time-efficient atmospheric water harvesting using Fluorophenyl oligomer incorporated MOFs. Nat Commun 2024;15.
[366] Yan X, Xue F, Zhang C, Peng H, Huang J, Liu F, et al. Solar-powered mixed-linker metal–organic frameworks for water harvesting from arid air. EcoMat 2024;6:e12473.
[367] Sahoo SK, Tripathi BP. Amino Acid-based Thermoresponsive Hydrogel/MOF Composite for Enhanced Atmospheric Water Harvesting and Solar Desalination. ACS ES&T Eng 2024;4:1644–56.
[368] Liu C-H, Xu L, Wang Z-Y, Han S-J, Li Y-B, Fu M-L, et al. Engineering defective MOF-801 nanostructures on the surface of a calcium alginate aerogel for efficient and stable atmospheric water harvesting. J Mater Chem A 2024;12:31533–46.
[369] Zhu M, He G, Wang Z, Chen J, Fu X, Yang H, et al. MOF-801 enabled rapid-cycling atmospheric water harvester with vertically aligned photothermal channel. J Environ Chem Eng 2024;12:113815.
[370] Wu Q, Feng Z, Zhou X, Li H. Spray-Applied MXene Coatings on Metal–Organic Framework Monoliths for Adaptive All-Day Atmospheric Water Harvesting at Mitigated Energy cost. Ind Eng Chem Res 2024;63:4866–75.
[371] Zhang L, Li R, Zheng S, Zhu H, Cao M, Li M, et al. Hydrogel-embedded vertically aligned metal-organic framework nanosheet membrane for efficient water harvesting. Nat Commun 2024;15.
[372] Guo S, Hu Y, Fang Z, Yaoab B, Peng X. LiCl in situ decorated metal–organic framework (MOF)-derived porous carbon for efficient solar-driven atmospheric water harvesting. RSC Adv 2024;14:15619–26.
[373] Wei Y, Huang X, Huang J, Li Z, Wang Q-Y, Ma Q. Free-standing MOF film with hierarchical porous structure for efficient solar-powered atmospheric water harvesting. Chem Eng J 2025;503:158426.
[374] Sahoo SK, Tripathi BP. Synergistic Super-Hygroscopic Composite Gel for Enhanced Atmospheric Water Harvesting and Desalination applications. Small 2025:2501809.
[375] Lin W-H, Chen Y-L, Yang S-Y, Zhong X-F, Feng J-H, Jia M-M, et al. Toward Enhanced Atmospheric Water Harvesting in Arid Conditions via Mixed-Ligand MOF-Derived Porous Carbon. ACS Appl Mater Interfaces 2025;17:34052–62.
[376] Shang B, Zhu M, Wang Z, Chen J, Fu X, Yang H, et al. Waste cigarette butts based super-hygroscopic photothermal materials for atmospheric water harvesting and solar-driven undrinkable water purification. Sep Purif Technol 2025;363:132238.
[377] Tian G, Fu C, Guo Z. Metal-organic framework-based composite adsorbents for atmospheric water harvesting: Materials and devices. Mater Today 2025;83:307–30.
[378] Song W, Zheng Z, Alawadhi AH, Yaghi OM. MOF water harvester produces water from Death Valley desert air in ambient sunlight. Nat Water 2023;1:626–34.
[379] Liu X, Beysens D, Bourouina T. Water Harvesting from Air: Current Passive Approaches and Outlook. ACS Mater Lett 2022;4:1003–24.
[380] Shao Z, Wang Z-S, Lv H, Tang Y-C, Wang H, Du S, et al. Modular all-day continuous thermal-driven atmospheric water harvester with rotating adsorption strategy. Appl Phys Rev 2023;10:041409.
[381] Wang W, Yang T, Pan Q, Dai Y, Wang R, Ge T. All-day freshwater production enabled by an active continuous sorption-based atmospheric water harvesting system. Energ Conver Manage 2022;264:115745.
[382] LaPotin A, Zhong Y, Zhang L, Zhao L, Leroy A, Kim H, et al. Dual-Stage Atmospheric Water Harvesting Device for Scalable Solar-Driven Water Production. Joule 2021;5:166–82.
[383] Feng Y, Ge L, Zhao Y, Li Q, Wang R, Ge T. Active MOF water harvester with extraordinary productivity enabled by cooling-enhanced sorption. Energ Environ Sci 2024;17:1083–94.
[384] Xu J, Huo X, Yan T, Wang P, Bai Z, Chao J, et al. All-in-one hybrid atmospheric water harvesting for all-day water production by natural sunlight and radiative cooling. Energ Environ Sci 2024;17:4988–5001.
[385] Wilson CT, Díaz-Marín CD, Colque JP, Mooney JP, Fil BE. Solar-driven atmospheric water harvesting in the Atacama Desert through physics-based optimization of a hygroscopic hydrogel device. Device 2025:100798.
[386] Metawea AM, Walker G. Continuous manufacturing and scale up of metal organic materials (MOM): current situation, challenges and future direction. J Ind Eng Chem 2025;148:150–73.
[387] DeSantis D, Mason JA, James BD, Houchins C, Long JR, Veenstra M. Techno-economic Analysis of Metal–Organic Frameworks for Hydrogen and Natural Gas Storage. Energy Fuel 2017;31:2024–32.
[388] Chakraborty D, Yurdusen A, Mouchaham G, Nouar F, Serre C. Large-Scale production of Metal–Organic Frameworks. Adv Funct Mater 2024;34:2309089.
[389] S. Ponton, D. Brassard, A. F. S. Rendón, S. Alavitabari, R. Boudreault, E. Bédard, P.-L. Girard-Lauriault and J. R. Tavares. A Guideline to Evaluate Sorbent Performance for Atmospheric Water Harvesting. *Advanced Energy and Sustainability Research,* p. e202500258, 2025.